OUKA
The University of Osaka
Institutional Knowledge Archive

Title	Ellipsometry Based on Spin-Orbit Interaction of Light
Author(s)	Faiz, Naila Zahra
Citation	大阪大学, 2026, 博士論文
Version Type	VoR
URL	https://doi.org/10.18910/105443
rights	
Note	

The University of Osaka Institutional Knowledge Archive : OUKA

https://ir.library.osaka-u.ac.jp/

The University of Osaka

Doctoral Dissertation

Ellipsometry Based on Spin–Orbit Interaction of Light

NAILA ZAHRA FAIZ

January 2026

Graduate School of Engineering
The University of Osaka

Ellipsometry Based on Spin–Orbit Interaction of Light

NAILA ZAHRA FAIZ

Abstract

The downsizing demand for devices stimulates the development of new materials and the fabrication of surfaces with intricate properties. These progresses lead to the demand for a precise measurement of subtle changes in interface properties. Ellipsometry is one of the established instruments for such needs due to its precision and multi-parameter measurement capability. However, its reliance on rotating elements and temperature-sensitive retarders can introduce operational complexity and long-term stability issues.

This work proposes a new ellipsometry technique employing the Spin–Orbit Interaction (SOI) of light, introduced as the Spin Hall Effect of Light (SHEL) ellipsometry. While not exactly ellipsometry in the conventional sense, the approach shares several similarities. In conventional ellipsometry, the target interface is characterized by ellipsometric angles retrieved from intensity-based polarization measurement. In SHEL ellipsometry, the target parameter is retrieved by measuring the polarization-dependent subwavelength beam shift emerging from the spin–orbit interaction. While conventional ellipsometry uses a pair of polarizers as polarization state generation and analyzer, a pair of polarizers in SHEL ellipsometry defines the almost orthogonal initial and final polarization states to realize the weak measurement scheme, allowing amplification of the SHEL shift.

First, a proof of concept to validate the proposed SHEL ellipsometry is carried out by examining several experimental parameters. Quantitative validation was performed by refractive index retrieval, demonstrating the quantitative capability of SHEL ellipsometry. The varying thickness of film layer profiles manifested in the variation of the beam shifts proves that SHEL observation qualitatively draws the structural profile on the nanoscale. Lastly, surface roughness variations as small as 0.6 nm, confirmed from AFM measurement, can be resolved through effective medium approximation modeling. The measurement scheme is inherently extendable from pointwise probing to line scans and ultimately to 2D areal mapping, enabling fast localized analysis as well as wide area observation.

The second stage is the extension of the SHEL ellipsometry working range to access high-sensitivity measurement at near Brewster incidence. Under horizontally polarized incidence, the SHEL shift shows an intrinsically amplified amplitude near Brewster's incidence, demonstrating promising enhancement for measurement. To access this high-sensitivity regime, the requirement of an appropriate weak measurement parameter is formulated through gain calculation. The results show not only better sensitivity reflected in the thin film thickness and 2D roughness measurement, but also establish practical guidelines for implementation near Brewster operation for SHEL ellipsometry. Additionally, the anomalous SHEL shift at the Brewster angle is shown to be beneficial in approximating unknown material refractive indices and in calibrating the incident angle.

The results presented in this thesis establish SHEL ellipsometry as a practical and scalable measurement framework that translates fundamental concepts of spin–orbit optics into a robust optical metrology tool to achieve sub-nanometer sensitivity under realistic experimental conditions. As such, this represents a concrete step toward bridging fundamental quantum-optical physics and industrially relevant nanoscale measurement technologies.

Contents

Abstract **i**

Contents **iii**

List of Figures **v**

List of Tables **ix**

1 Introduction **1**
1.1 Background and Motivation 1
1.2 Ellipsometry as an Optical Characterization Technique in Material Science 7
1.3 Spin–Orbit Interaction and Precision Metrology 12
1.4 Research Objectives 17
1.5 Organization of the Dissertation 18

2 Theoretical Principles **21**
2.1 Introduction 21
2.2 Spin–Orbit Interaction and Beam Shifts 22
2.3 The Spin Hall Effect of Light upon Reflection 25
2.4 Weak Measurement Approach to the Spin Hall Effect of Light 28
2.4.1 Conventional Weak Measurement 28
2.4.2 Modification to the Weak Measurement 31
2.4.3 Experimental Implication of Weak Measurement in SHEL Observation 32
2.5 Beam Propagation Factor 35
2.6 Optical Interface Model 37
2.7 Definition and Detection of the Beam Shift 42
2.8 SHEL Ellipsometry Framework 44

3 Proof-of-Concept of the Spin Hall Effect of Light Ellipsometry **49**
3.1 Introduction 49
3.2 Experimental Setup 50
3.3 Measurement Application 54
3.3.1 Refractive Index 55

3.3.2 Film Thickness 61
3.3.3 Surface Roughness 65
3.4 Conclusions 75

4 High Sensitivity Measurement at Near Brewster Incidence 77
4.1 Introduction 77
4.2 Anomaly of SHEL Shift at Brewster Angle 78
4.2.1 Polarization and Angular Dependence of SHEL 78
4.2.2 Angular Parameter in Weak Measurement Observation of SHEL 81
4.3 Observation of SHEL Shift at Near Brewster Incidence 83
4.4 Measurement of Physical Properties Using SHEL Ellipsometry at Near Brewster Incidence 88
4.5 Comparison to Conventional Ellipsometry 94
4.6 Conclusions 99

5 Conclusions 101

Bibliography 109

List of Publications and Awards 123

Acknowledgements 125

List of Figures

1.1 General principle of ellipsometer which determines ellipsometry parameters based on the phase shift Δ and the amplitude ratio ψ of polarized waves 8
1.2 Several configurations of ellipsometer, (a) General configuration, (b) Rotating compensator ellipsometer (RCE), (c) Rotating analyzer ellipsometer (RAE), (d) PME, (e) Spectroscopic ellipsometer (SE), and (f) Mueller matrix ellipsometer (MME) 11
1.3 Spin and orbital angular momentum are analogous to the planet rotation and revolution, where spin corresponds to the photon rotation on its axis and orbit corresponds to the photon revolution 14
1.4 Illustration of angular momentum of light (a) spin angular momentum corresponds to the circular polarization of the electric field, (b) intrinsic orbital angular momentum manifests as helical phase front, and (c) extrinsic orbital angular momentum is expressed physically as beam transverse shift. 16
1.5 Structure of the dissertation 20

2.1 Graphical illustration of the four sub-wavelength beam shift, (a) spatial IF shift or SHEL shift, (b) angular IF shift, (c) spatial GH shift, and (d) angular GH shift 23
2.2 Principle of the Spin Hall Effect of Light (SHEL) upon reflection off an interface, decomposed circular polarizations component displaced at a distance of δ_r from the supposed reflection trajectories at the same plane of the incidence. 26
2.3 Pair of polarizers defining the initial and final polarization state in a weak measurement scheme to amplify and observe the SHEL shift. 33
2.4 Implication of ε value to the observed intensity of SHEL shift, (a) $\varepsilon = 0$, (b) $+\varepsilon$, (c)$-\varepsilon$, (d) distorted state when ε is too small and $\langle f|i\rangle \approx 0$ 35
2.5 Propagation factor of Gaussian beam (a) in free space, and (b) in a telescopic lens system. 37
2.6 Optical interface models, (a) air-glass, (b) thin film layer, and (c) roughness layer . . . 38
2.7 Oblique reflection by a single layer (thin film or EMA roughness layer) with parallel-plane boundaries. 41
2.8 Definition of SHEL beam shift based on the recorded images, based on experimental procedures, and ε value. Cross-polarizer ($\varepsilon = 0$) images are used to define the reference point and shifted beam centroid ($\varepsilon \neq 0$) y_ε distance to the reference y_0 is defined as the detected amplified SHEL shift. 43

2.9 Working flow of the image processing in detecting the beam shift, the yellow block corresponds to $\varepsilon = 0$ and the green block corresponds to $\varepsilon \neq 0$. 45
2.10 Flowchart of measurement procedure using SHEL ellipsometry 48

3.1 Experimental setup of SHEL Ellipsometry 51
3.2 Schematic of Incident Angle Control by Double Rotating Mount 51
3.3 Picture of the Complete Experiment Setup 54
3.4 Numerical calculation of SHEL shift upon varying refractive index (a) for $|H\rangle$ and (b) for $|V\rangle$ 56
3.5 Sample with known refractive index value, (a) top view, (b) side view 56
3.6 SHEL shift measurement on varying incident angle from 40∘ to 70∘ with $|H\rangle$ incident (a) $\varepsilon = 0.5^o$; (b) $\varepsilon = 1.0^o$; (c) $\varepsilon = 1.5^o$; and with $|V\rangle$ incident (d) $\varepsilon = 0.1^o$; (e) $\varepsilon = 0.3^o$; (f) $\varepsilon = 0.5^o$ 58
3.7 Comparison of samples with different refractive index: MgF_2 ($n = 1.37; \theta_B \approx 54°$) and CaF_2 ($n = 1.43; \theta_B \approx 55°$), (a) using $|H\rangle$ with $\varepsilon = 1.5°$ and (b) using $|V\rangle$ with $\varepsilon = 0.5°$ 60
3.8 Measurement result of refractive indices (a) using $|H\rangle$ and (b) using $|V\rangle$ 60
3.9 Numerical calculation of SHEL shift to incident angle of varying Au film thickness from 0.5 nm to 10 nm on a BK7 substrate (a) using $|H\rangle$ and (b) using $|V\rangle$ 62
3.10 Sample preparation of gold film thickness on BK7 and SiO_2 (a) design of film layer and deposition time (b) sample of gold film layer on SiO_2 substrate 62
3.11 Measured SHEL shift using $|H\rangle$ of (a) gold film layer on SiO_2 and (b) gold film layer on BK7 64
3.12 Numerical calculation of the influence of surface roughness on SHEL shift (a) $|H\rangle$ incident, (b) $|V\rangle$ incident 66
3.13 Schematic of raster scanning and overlapping beam scanning process 66
3.14 Scanning result of three different optical flats for MgF_2, CaF_2, SiO_2 in (a-c) 2D reconstruction and (d-f) 3D reconstruction 67
3.15 Full-field WLI scanning from product manual of SiO_2 optical flat (a) 2D reconstruction, (b) 3D reconstruction 69
3.16 WLI scanning of SiO_2 (a) central area, (b) outer diameter area, and (c) roll-over area . 69
3.17 SHEL scanning on (a) SiO_2 optical flat, (b) center area, and (c) edge area 70
3.18 SHEL scanning of SiO_2 (a) scanning area (b-e) result of the four area scanning 71
3.19 Comparison scanning of AFM and SHEL ellipsometry of SiO_2 optical flat (a) AFM of polished surface, (b) AFM of unpolished surface, (c) SHEL ellipsometry of polished surface, (d) SHEL ellipsometry of unpolished surface 73

4.1 (a) Calculation of Fresnel reflection coefficient and illustration of the polarization component at Brewster angle incident (b) for unpolarized incident beam, (c) for p-polarized incident beam 80
4.2 Original SHEL shift to incident angle due to varying physical properties, (a) refractive index, (b) varying film thickness, (c) varying thickness equivalent surface roughness, (d) absolute SHEL shift to d_{EMA} 82
4.3 Influence of the varying azimuth angle on Amplified SHEL shift 84

4.4 Amplification factors $G_{Amod} = \delta^H_{Amod}/\delta^H_r$ in Weak Measurement Observation of SHEL, (a) influence of angular parameters, (b) influence of incident angle, (c) influence of azimuth angle, (d) optimal angular parameters 84
4.5 SHEL shift simulation compared to the experimental observation (a) simulation at $\theta_i = 50°$, (b) simulation at $\theta_i = 60°$, (c) observation at $\theta_i = 50°$, (d) observation at $\theta_i = 560°$ 85
4.6 Observation of SHEL shift at the Brewster angle 86
4.7 SHEL shift simulation compared to the experimental observation at near Brewster incidence considering the optimal post-selected angle criteria (a) simulation with small ε, (b) simulation with large ε, (c) observation with small ε, (b) observation with large ε . 86
4.8 Observation of SHEL shift to incident angle at different regions (a) far from Brewster angle and (b) near Brewster incidence, considering the optimal post-selected angle criterion 89
4.9 Comparison of SHEL shift due to nanofilm thickness observed at different regions . . . 93
4.10 Surface roughness measurement using SHEL ellipsometry observed at different regions (a) front face, (b) rear face, (c) front face with near Brewster incidence, (d) rear face with near Brewster incidence 93
4.11 Rotating analyzer ellipsometry (a) schematic of optical configuration, (b) samples of recorded intensity measurement (c-d) intensity as analyzer angle and the corresponding sinusoidal fitting 97
4.12 Measurement results of $|\rho|$ from $50° - 60°$ from RAE and SHEL comparet to Fresnel formula theoritical calculation 97

List of Tables

1.1 Comparison of several measurement techniques in material characterization 6

3.1 Specification of He-Ne Laser. 52
3.2 Specification of Polarizer Sheet and Rotating Mount. 53
3.3 Specification of Lenses 53
3.4 Specification of CCD Camera 54
3.5 Specification of substrates used as the base of gold film growth 64

4.1 Pseudo refractive index n and corresponding percentage error for different incident angles θ_i. 91
4.2 Refractive index n and corresponding percentage error at different incident angle θ_i for near Brewster incidence operation. 91
4.3 Comparison of conventional ellipsometry and SHEL ellipsometry 96

Chapter 1

Introduction

1.1 Background and Motivation

In ancient times, civilization had used nanoparticles such as gold and silver in stained glass and ceramics, as well as nanostructures in Damascus steel, unknowingly [1]. However, the term nanometer, defined as 1/1000.000.000 meters, was not familiar until it was first introduced in the early 20th century by Richard Zsigmondy, a chemist and Nobel laureate, who measured gold colloidal nanoparticles [1, 2]. Following that, "There's Plenty of Room at the Bottom," a lecture by Feynman, points out the idea for extremely small machines that at the time was limited only by lack of equipment and technique rather than limited by the laws of nature [2, 3]. Some key technological breakthroughs in nanoscience and technology include the discovery of fullerenes (C60), the development of carbon nanotubes, and the invention of Scanning Tunneling Microscopy (STM) and Atomic Force Microscopy (AFM), which enable the observation of atoms and support advanced material discoveries [2, 4–6].

Advances in nanoscience and nanotechnology have revolutionized a wide range of sectors, including medicine, biology, optics/photonics, food and agriculture, energy, environmental sciences, and the semiconductor industry. In medicine, it enables targeted drug delivery, advanced imaging techniques, and tissue engineering, leading to significant improvements in diagnostic accuracy and therapeutic

efficacy [7–9]. In optics and photonics, the development of nanomaterials and nanomanufacturing techniques has facilitated the creation of advanced displays, lasers, and photodetectors [10, 11]. In the biological sciences, nanoparticles play a crucial role in biosensing and cellular imaging, allowing the investigation of biological processes at the molecular scale [12, 13]. Nanomaterials also contribute to environmental sustainability through applications in water and air purification and environmental monitoring [14]. Among these fields, the semiconductor industry stands out as a primary driver of nanosciences and nanotechnology, as its technological demands are both influenced by and supportive of advancements across other application areas.

In the semiconductor industry, advances in nanoscience and nanotechnology enable the sector to overcome the physical limits of traditional materials and fabrication methods. Downscaling of devices leads to smaller, faster, and more efficient chips and transistors [15–17]. Discoveries of nanomaterials improving the performance of electronic and optoelectronical devices, such as graphene which offer unique electrical, mechanical, and optical properties [18], the carbon nanotubes that enable energy-efficient high-speed transistors [19], or the nanowires and quantum dots that allow precise control of electronic and optical properties for new device architecture [16]. Nanotechnology also involves new manufacturing methods that enable the fabrication of nanostructures or thin-film deposition [15, 20]. The study of nanomaterials has grown and has since discovered new functionalities and better material properties that benefit the development of sensors, photodetectors, and bioelectronic interfaces [15, 16].

As the discovery of STM and AFM accelerates nanoscience and nanotechnology, the urgency of metrological advancement in helping material characterization has been proven to be essential. During the design, processing, evaluation, and deployment, the correct and sufficient properties need to be measured. Most of the time, the performance and properties of materials and devices are highly dependent on their dimensions and morphology, making precise characterization essential. Material characterization helps understand the unique properties of intricate materials, ensuring reproducibility and reliability, providing feedback for the manufacturing process, and assessing safety in the processing [21–23].

Material characterization techniques are often broadly categorized as chemical or physical. However, many of these methods are inherently surface-sensitive, and the distinction frequently overlaps in practical applications. Chemical characterization focuses on identifying chemical composition, bonds, structures, and stoichiometry. Techniques such as X-ray photoelectron spectroscopy (XPS), energy-dispersive X-ray spectroscopy (EDX), secondary ion mass spectrometry (SIMS), and Fourier-transform infrared spectroscopy (FTIR) provide detailed information for oxidation state and local structure, elemental analysis, chemical bonding, and functional groups, which are very useful for probing surface chemistry in nanoparticles and complex materials [24–26]. Physical characterization employs a range of methods such as scanning electron microscopy (SEM), transmission electron microscopy (TEM), atomic force microscopy (AFM) to assess surface morphology, nanostructures, and particle size; X-ray diffraction (XRD) to determine crystal structure and phase composition; and spectroscopic techniques such as UV-Vis and photoluminescence to probe optical properties including absorption and emission [27, 28]. Ellipsometry is a notable hybrid technique, capable of assessing both optical constants and surface-related structural parameters like thickness and roughness through polarization analysis [29].

Among the wide range of material parameters accessible through different methods and instruments, refractive index, thin-film thickness, and surface roughness are especially crucial because they govern the fundamental light–matter interactions that define device performances such as optical coatings, photonic sensors, photonic devices, and nanostructures [30–32]. Their interplay affects light propagation, device sensitivity, and overall efficiency, making it common to study these three properties simultaneously [31, 33, 34]. Accordingly, the development of simultaneous determination of two to three of these properties has been widely studied [35–38]. In this research, we focus on surface metrology and optical characterization methods, with particular emphasis on refractive index, thin-film thickness, and surface roughness.

Among established direct surface metrology techniques, AFM provides high-resolution topographic imaging by detecting interactions between a sharp cantilever tip and the sample surface, achieving sub-nanometer accuracy [39]. However, this technique is relatively slow and typically restricted to scanning

areas no larger than 100×100 micrometers. Additionally, the geometry and condition of the AFM probe tip significantly contribute to measurement uncertainty [40]. SEM is also widely applied for surface morphology and roughness analysis with nanoscale lateral resolution [41, 42]. Even so, SEM's reliance on electron beams and its need for conductive samples or coatings can limit its applicability and potentially be damaging to sensitive samples.

Optical surface metrology techniques, in contrast, provide non-contact and non-destructive measurement capabilities that are highly desirable for industrial and in-line applications. White Light Interferometry (WLI) is a high-resolution, non-contact technique for measuring surface topography, roughness, and film thickness. It leverages the interference of broadband light to generate 3D surface profiles with nanometer height resolution [43], making it attractive for applications such as MEMS, thin film analysis, surface studies, and industrial inspection of silicon wafers [44]. Nevertheless, WLI exhibits limitations related to surface slope and geometry, environmental and mechanical sensitivity, limited lateral resolution, and the requirement of a reference plane [45]. It also struggles with abrupt height changes or steep slopes and is less effective for highly curved, transparent media, and rough surfaces, where reconstruction errors and data loss can occur [46, 47]. Due to its sensitivity, environmental vibrations and mechanical instabilities in the setup introduce phase error that often requires complex compensation strategies [48, 49]. The effective measurement range of WLI is determined by the coherence length of the light source ($\lambda/2$) and optical configuration, such as the lens numerical aperture of the lens in a microscopy setup [50].

Techniques such as AFM, SEM, and WLI are classified as direct surface measurement approaches, as they rely on physical probing or direct optical examination of surface topography. In contrast, scatterometry and ellipsometry are indirect, model-based optical metrology techniques that infer surface and structural parameters from the interaction of light with the sample. These techniques are well-established for high-throughput evaluation of nanostructured surfaces [51]. Scatterometry observes and analyzes how light scatters from surface structures, especially periodic ones, to extract dimensional and structural information as a function of wavelength or angle by interpreting the diffraction pattern. This

technique is widely employed in semiconductor manufacturing due to its cost-effectiveness, rapid non-contact measurement, and suitability for in-line monitoring. A theoretical electromagnetic model of the sample structure complements the measurement. Key limitations include its strong model dependence, which increases complexity and can introduce errors if surface features such as roughness or non-uniformities are not properly included in the model [52, 53].

Several specialized surface-sensitive techniques have been used for thin film measurement. Reflectometry, for instance, determines optical properties and thickness by analyzing reflected intensity as a function of wavelength or angle [54, 55]. It is well-suited for in-situ monitoring and can also sense parameters such as temperature or strain [56]. However, because it relies solely on intensity, reflectometry faces the difficulty in identifying the optical loss source or retrieving full dielectric properties [57]. Spectroscopic reflectometry measures wavelength-dependent reflectance from the film surface and analyzes the interference pattern in estimating thickness, which is typically effective in the nanometer to millimeter range [58, 59]. Advanced configurations, such as time-domain and optical frequency-domain reflectometry (OFDR), can be employed to achieve the required resolution, depending on the application [60–62]. Other widely used techniques include X-ray reflectivity (XRR) and quartz crystal microbalance (QCM). XRR analyzes reflected X-rays at low angles to obtain electron density profiles, thickness, and roughness. It offers high precision and is particularly useful for multilayer structures, but requires long measurement times and operates best on smooth, well-defined surfaces [58, 63, 64]. QCM detects changes in the resonance frequency of a quartz crystal due to mass changes on its surface. While primarily a mass-sensitive technique, it can indirectly monitor thickness changes in thin films deposited on the quartz surface, but it is less suitable for hard/inorganic films [65].

Established refractive index measurement technique for bulk materials includes the prism coupling methods, Brewster angle refractometry, and ellipsometry [66, 67]. Several physical interactions with materials, like thermal effects, nonlinear optical effects, and photo-induced structural modifications, can be indirectly monitored via refractive-index variation [68–71]. Consequently, refractive index measurement plays a crucial role in surface and thin-film optical metrology.

While reflectometry measures only the intensity of reflected light, ellipsometry analyzes polarization changes upon reflection, providing access to both amplitude and phase information. This enables ellipsometry to extract refractive index, thin-film thickness, surface roughness, and even anisotropy, making it one of the most versatile techniques for advanced surface and thin-film metrology [72]. Similar to scatterometry and reflectometry, ellipsometry measures area-averaged optical responses and relies on accurate optical models to interpret experimental data. Surface roughness and inhomogeneity were initially considered complications in ellipsometric analysis that required compensation [73, 74]. However, in subsequent studies, this sensitivity could be exploited to directly retrieve surface roughness as an additional measured parameter [75, 76].

Various methods and principles for measuring surface-related parameters have been discussed. Table 1.1 provides a comparative summary of the existing surface metrology instruments.

Table 1.1: Comparison of several measurement techniques in material characterization

Category	**Technique**	**Measured Parameters**	**Advantages**	**Limitations**
Non-optical	AFM	Surface topography	Sub-nm vertical resolution	Slow, small scan area, tip wear
Non-optical	SEM	Surface morphology	High magnification and nm lateral resolution	Vacuum operated, conductive sample/coating required
Optical	WLI	Surface topography, film thickness	Fast, non-contact, nm vertical resolution	Reference surface, surface slope, abrupt height changes, hundreds nm to mm film thickness, only transparent film
Optical	Scatterometer	Thickness, critical dimensions, profile	Fast, high precision for periodic structure	Model dependent, not suitable for random surface, hundreds nm to mm film thickness
Optical	Reflectometer	Thickness, refractive index	Fast, low complexity	Limited information, less sensitive to thin films < 10 nm
Optical	Ellipsometry	Refractive index, thickness, surface roughness	high sensitivity to film thickness with nm precision, multi-parameter, broad material compatibility	Rotating element, temperature sensitive retarder, requires rigorous fitting

While a wide range of tools exists for material characterization, ellipsometry stands out for its ability to simultaneously determine multiple parameters with high precision. Despite its versatility and precision, ellipsometry presents practical challenges, including reliance on rotating components or modulators that introduce mechanical complexity, alignment sensitivity, and long-term stability issues due to environmental factors such as temperature drift.

These limitations motivate the exploration of alternative surface-metrology strategies that preserve the multi-parameter sensitivity of ellipsometry while improving robustness against thermal and mechanical perturbations. One promising direction is the exploitation of the spin–orbit interaction of light, which provides new opportunities for stable and highly sensitive optical surface metrology. The following section introduces ellipsometry in detail, establishing the foundation for the proposed alternative.

1.2 Ellipsometry as an Optical Characterization Technique in Material Science

Given the increasing demand for accurate, non-destructive evaluation of material properties outlined in the previous section, ellipsometry has emerged as one of the most powerful optical techniques for this purpose. Ellipsometry's ability to simultaneously determine multiple parameters with high precision makes it interesting in industrial environments such as semiconductor manufacturing and optical coatings. Over the decades, ellipsometry has evolved and preserved its reputation as a versatile metrology tool, with various configurations and applications for a wide variety of materials and structures. This section provides a detailed discussion of ellipsometry, including its operating principles, configurations, capabilities, and limitations.

As previously mentioned, ellipsometry stands out as a highly versatile non-destructive optical testing method capable of simultaneously evaluating thin film thickness, refractive index, and subwavelength roughness under appropriate modeling. In general, ellipsometry operates by analyzing the change in polarization state of light upon reflection from a sample. It retrieves a complex ellipsometry parameter

that consists of amplitude and phase related to the sample information with sub-nanometer sensitivity [77–80]. The measurable quantity in ellipsometry is the complex reflectance ratio, also known as the ellipsometry parameter, denoted by ρ, and consists of ellipsometry angles ψ and Δ [77],

$$\rho = \frac{r_p}{r_s} = \tan(\psi)\exp(i\Delta) \tag{1.1}$$

where the ψ and Δ are defined through the complex Fresnel coefficient ratio, r_p and r_s, with $\tan\psi = \frac{|r_p|}{|r_s|}$ and $\Delta = \arg(r_p) - \arg(r_s)$. These parameters are measured and fitted to the optical model of the interface to retrieve physical properties with subnanometer sensitivity. Figure 1.1 shows an illustration of the ellipsometry measurement principle [81].

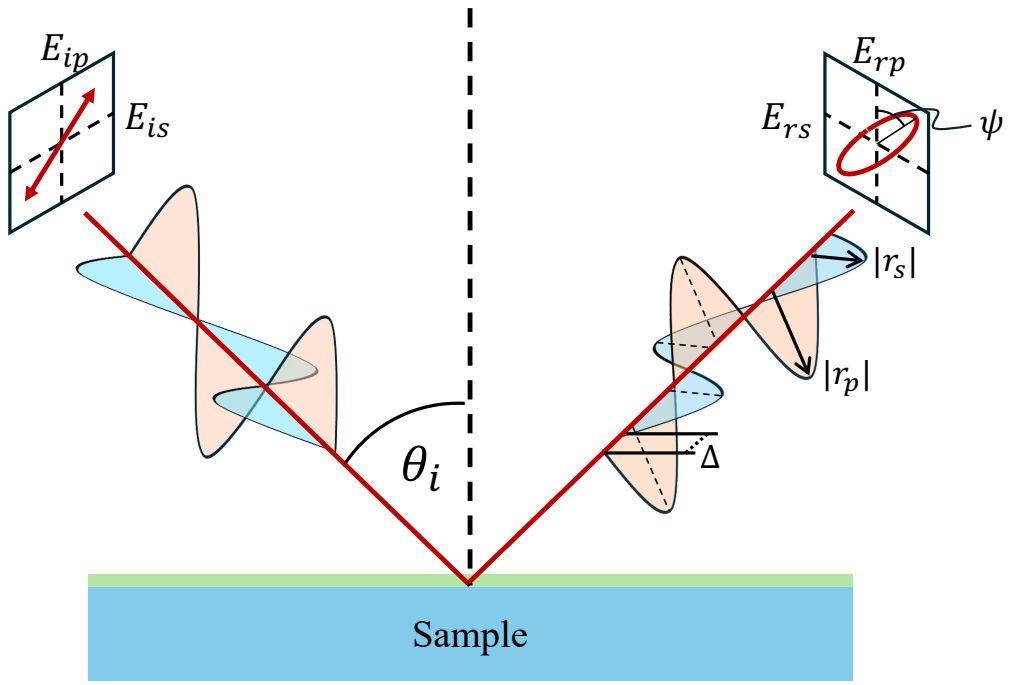


Fig. 1.1: General principle of ellipsometer which determines ellipsometry parameters based on the phase shift Δ and the amplitude ratio ψ of polarized waves

Ellipsometry was initially recognized for its precision and accuracy in determining thin film thickness and refractive index, but later studies revealed its notable sensitivity to surface roughness as well [73,75]. In ellipsometric analysis, roughness evaluation serves two main functions: it enables correction of the extracted optical parameters to exclude roughness-induced artifacts and provides a means to distinguish varying degrees of surface roughness [29]. In practice, this sensitivity has been modeled effectively using effective medium approximation, where the roughness layer is treated as a uniform layer with effective optical constants derived from a mixture of voids and the underlying material [75]. It has also been employed alongside techniques such as AFM to provide complementary surface characterization data [51, 82].

The general configuration of an ellipsometer is commonly referred to as the Polarizer-Sample-Compensator-Analyzer (PSCA) ellipsometer. The polarizer sets the input polarization state, the compensator introduces a known phase shift, the sample modifies the polarization state upon reflection, and the analyzer resolves the output polarization state. The compensator can be placed either before or after the sample. The measurement is performed in a static configuration. PSCA/PCSA ellipsometer provides a foundation for many ellipsometry designs.

Over the decades, ellipsometry has undergone continuous advancement. Various instrumental configurations have been developed to improve measurement accuracy and broaden the application range, such as the rotating analyzer ellipsometer (RAE), the rotating compensator ellipsometer (RCE), the phase modulation ellipsometer (PME), and the spectroscopic ellipsometer (SE) [83].

The rotating analyzer ellipsometer (RAE), introduced in 1962 by W. Budde, consists of a static polarizer and compensator, and a continuously rotating analyzer during measurement [84]. This rotation modulates the detected signal, enabling the extraction of the ellipsometer angles. Although RAE can be cost-effective, it can also be slower and sensitive to mechanical alignment errors. The rotating compensator ellipsometer (RCE) places a rotating compensator, usually a quarter-wave plate (QWP), that modulates the polarization state to improve accuracy in the Δ retrieval at some specific angles [85]. The Phase Modulation Ellipsometer (PME) is a refined version of the ellipsometer that uses a

photoelastic modulator to oscillate the beam's polarization, enabling rapid and sensitive measurements of ellipsometric angles. PME does not need a continuously rotating part, which improves mechanical stability, although careful calibration of the modulator is still necessary [86].

Extensions such as spectroscopic ellipsometry (SE) expand measurements across a wide spectral range, allowing the retrieval of wavelength-dependent optical properties, which is beneficial for wavelength-sensitive optical behavior. SE is implemented with a spectrometer as the detector in ellipsometer configurations [80, 87]. Another more sophisticated development, such as Mueller-matrix ellipsometers (MME), extends the conventional ellipsometry by measuring the full 4×4 Mueller matrix, capturing all polarization effects, including depolarization and anisotropy. MME is suitable for characterizing complex, depolarizing, anisotropic samples and has shown the ability for the retrieval of nanostructures' surface [88]. With expanded measurable parameters, the instrumentation is more complex, involving multiple PSG and PSA, each of which can consist of a combination of rotating retarders and phase modulators as a multi-state controller [89]. Figure 1.2 illustrates several mentioned ellipsometer configurations, providing a compact description of their diversity. Additionally, these different configuration of ellipsometry is also expanded into imaging ellipsometry, enabling spatially resolved mapping of thin films and surface characterization [90–92].

As most of these configurations require a continuously rotating mechanical element, they are sensitive to rotating alignment errors. Additionally, when a retarder is included in the configuration, the temperature dependency might alter the measurement result [93, 94]. Although a zero-order retarder less sensitive to temperature dependence is currently standard, it is preferable to avoid installing one in the ellipsometer setup entirely. Additionally, for an ultra-thin film thickness down to 5 nm, extracting parameters has shown faced difficulty, consequently needing advanced modeling or complementary measurement with other methods [36, 95].

In this work, we address these limitations by integrating a subwavelength optical phenomenon arising from the spin–orbit interaction of light called the Spin Hall Effect of Light (SHEL) into the ellipsometry framework. Unlike conventional ellipsometry configurations, which rely on mechanically

rotating components and temperature-sensitive retarders, the proposed SHEL-based approach enables polarization-dependent signal detection without moving parts. Consequently, significantly reduces the susceptibility to any mechanically-sourced error and thermal drift during long measurement time. Moreover, the intrinsic sensitivity of SHEL to parameter variations at the interface offers the capability for characterizing thin films and nanoscale surface roughness down to subnanometer resolution. The following section introduces the underlying physics of SHEL and discusses its suitability for a robust ellipsometric technique for precision measurement.

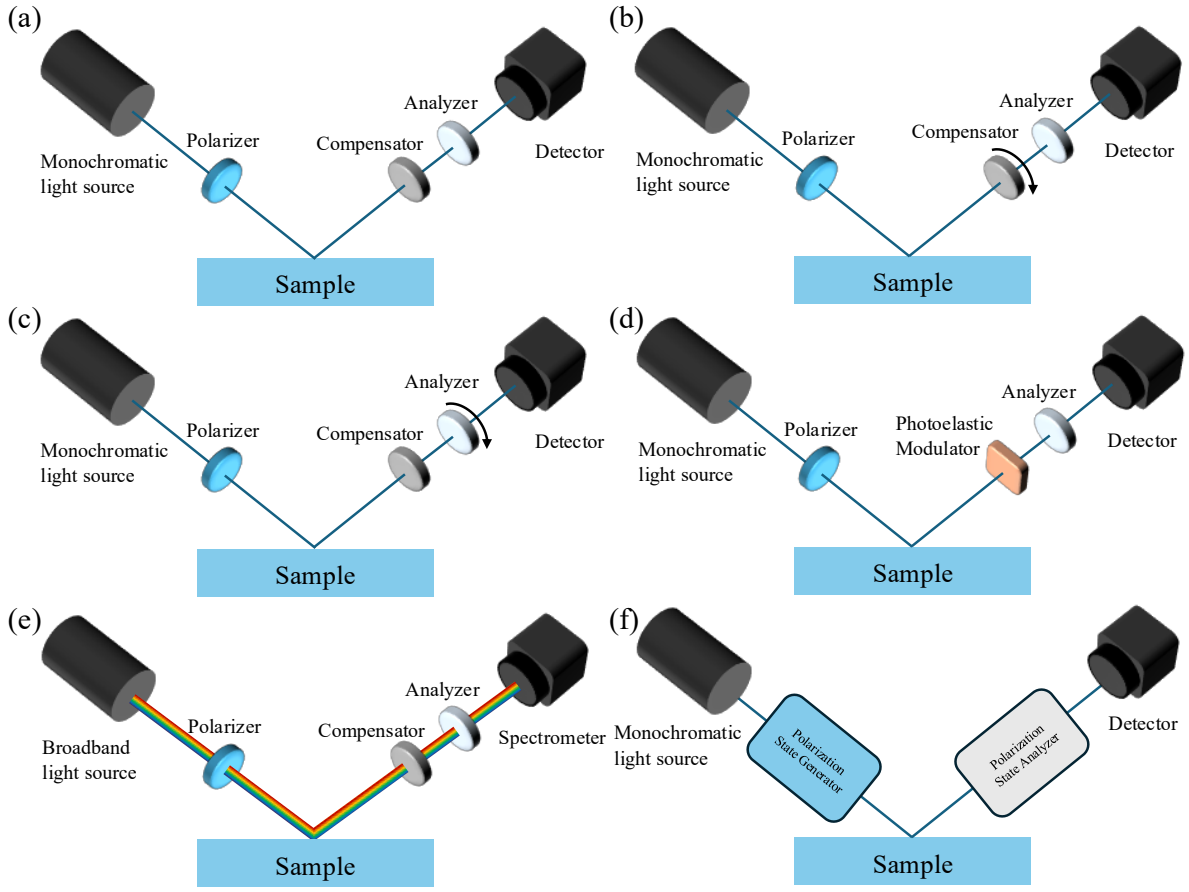


Fig. 1.2: Several configurations of ellipsometer, (a) General configuration, (b) Rotating compensator ellipsometer (RCE), (c) Rotating analyzer ellipsometer (RAE), (d) PME, (e) Spectroscopic ellipsometer (SE), and (f) Mueller matrix ellipsometer (MME)

1.3 Spin–Orbit Interaction and Precision Metrology

Previous explanations of ellipsometry principles highlight the role of polarization in probing the material properties. Beyond the changes in polarization state in light-matter interaction demonstrated by the ellipsometry framework, confined beams also undergo polarization-dependent spatial displacement at interfaces. This broader class of phenomena, known as the spin–orbit interaction (SOI) of light, includes the Spin Hall Effect of Light (SHEL), which is introduced in this section.

SHEL is a phenomenon where a confined light beam experiences a polarization-dependent transverse shift at optical interfaces. It is often discussed along with other types of subwavelength beam shifts, the Goos-Hänchen (GH) and Imbert-Fedorov (IF) shifts [96–98]. In contrast to SHEL, the GH shift occurs in the longitudinal direction (in-plane) [99]. On the contrary, the IF shift is linked to SHEL and defines the out-of-place subwavelength beam shift. Historically, the IF shift was observed exclusively in reflection, then subsequent studies revealed that it also occurs in transmission, which leads to the generalization of IF shift as SHEL with circular polarization as its eigenmodes. SHEL, as one of the SOI manifestations, is significant at the micro- and nanoscales and has been extensively studied. It is known to offer substantial benefits in light manipulation and photonic device applications [100]. Then, by enabling polarization-dependent spatial separation of light, SHEL can be harnessed for compact beam steering and spin-controlled routing in integrated photonic circuits. In quantum and spin-photonics, it facilitates spin–orbit coupling for information encoding, quantum state manipulation, and secure communications [101,102]. SHEL also enhances imaging and microscopy through contrast improvement and chirality-sensitive detection [103, 104].

Beyond those functional photonic applications, SHEL has proven especially valuable for precision optical measurement. Since it universally occurs at interfaces, both in reflection and transmission, SHEL enables a flexible metrological platform. Although both schemes can be utilized, they differ in sensitivity, tunability, and practical implementation, where reflection-SHEL is more widely preferred and adopted for various measurements. Reflection-SHEL has been demonstrated in offering high-precision

measurement of different physical properties, even in real-time and compact measurements [105–107]. It is highly tunable via the incident angle, polarization, and interface design. Transmission-SHEL, while also sensitive, is often less pronounced than reflection-SHEL [108]. However, it is proven powerful for specific samples, such as metasurfaces or layered structures [109, 110]. Applications reported in the previous studies of SHEL application include characterization of graphene layers [111, 112], refractive indices [113, 114], optical conductivity [115, 116], film thickness [117, 118], and polarization properties at various interfaces [119, 120]. Besides that, it has also been reported to enable a sensing platform through the detection of refractive index dynamics of specific material due to external parameters, such as using parity-time symmetric interface for gas sensing [121], humidity sensitive metamaterials for detection of biomolecules [122], chemical reaction rate of sucrose hydrolis [123], and discrimination of cancerous cells [124]. Furthermore, SHEL-based measurement has been reported to enable dual or multi-function measurement, for example, detection of refractive index and graphene layer [111], refractive index sensing in conjunction with resonance angle and fermi energy detection [114], and combination of temperature-film thickness [125]. These diverse applications have been enabled by polarization-dependent beam splitting, which provides a versatile means of inferring material properties at the interface.

To introduce SHEL in context, it is first necessary to consider how light carries angular momentum and how the coupling between its components leads to spin–orbit interaction. Light possesses angular momentum in two distinct forms: spin angular momentum (SAM), linked to the circular polarization of light, and orbital angular momentum (OAM), which arises from the spatial structure of the light's wavefront, as in helical or vortex beams [126]. Both can be viewed as the circular movement of photons, though in different senses. A simple analogy helps differentiate the two angular momenta. SAM resembles the rotation of a planet about its own axis, while OAM corresponds to the planet's orbital movement around the sun, as illustrated in Fig. 1.3 [127].

Furthermore, OAM can be categorized into intrinsic and extrinsic components. Intrinsic OAM (IOAM) is associated with the inherent helical phase front of a vortex beam, marked by its phase

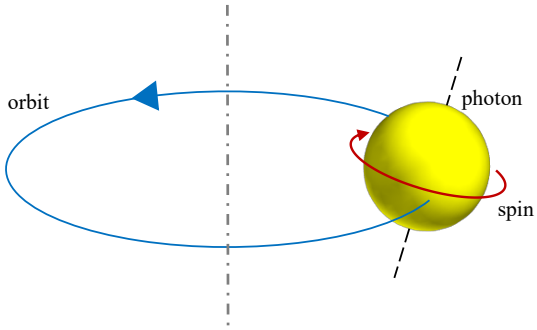


Fig. 1.3: Spin and orbital angular momentum are analogous to the planet rotation and revolution, where spin corresponds to the photon rotation on its axis and orbit corresponds to the photon revolution

singularity at the center. Extrinsic OAM (EOAM), on the other hand, happens when the entire beam is displaced or shifted from its expected trajectory [128]. Figure 1.4 summarizes the three forms of angular momentum. Although SAM and OAM are usually independent, in certain conditions they couple into the spin–orbit interaction of light, which underlies phenomena such as SHEL.

SOI gives rise to a range of intriguing physical phenomena. One of the widely studied phenomena is the spin-dependent splitting of light that occurs in inhomogeneous media or at interfaces, which is referred to as the Spin Hall Effect of Light (SHEL) [129, 130]. SOI can also reshape light by enabling spin-controlled shaping and conversion of light modes, such as the generation of a vortex beam from a Gaussian beam through a birefringence material [128, 131]. In engineered systems, such as metasurfaces, the interaction is further enhanced, offering opportunities in information processing and communication [109]. At nonparaxial fields, SOI occurs in tightly focused regions, which will cause the polarization to affect the spatial distribution and propagation of light [132, 133].

In this research, the focus is on the Spin Hall Effect of Light (SHEL). A circularly polarized beam, also known as a SAM-carrying beam, undergoes a tiny shift from its supposed secondary trajectory when interacting with an interface. The direction and magnitude of this shift depend on both the incident beam polarization and the modifying property at the interface. This polarization-dependent shift forms the physical core principle for exploiting the SHEL shift as a sensitive measurement tool.

There are significant conceptual and experimental similarities between SHEL-based measurement and ellipsometry, as both rely on the interaction between a sample or interface and the polarization of light. In ellipsometry, the sample induces a change in polarization that is directly measured by analyzing the polarization state of the reflected light. A similar light–matter interaction occurs in SHEL, but the effect manifests as a transverse beam shift. Although this difference relates to the measured quantity, both techniques fundamentally depend on polarization control and require at least a pair of polarizers in their setups.

In ellipsometry, one of the polarizers functions as an "analyzer," dedicated to detecting changes in the polarization state after reflection. In contrast, within the SHEL framework, the polarizer pair plays a different role: they realize the pre- and post-selection conditions in a weak measurement scheme. The polarizers are oriented nearly orthogonally to each other, ensuring that weak coupling occurs. This configuration amplifies the measurable beam shift, enhancing sensitivity to subtle sample-induced changes.

These parallels form the base of the idea that SHEL can be incorporated into an ellipsometry-inspired measurement framework, offering distinct advantages. By converting the weak-measurement-enhanced beam shift into physical parameters, the method could address some limitations of traditional ellipsometry, such as reliance on rotating optical components. Importantly, although SHEL has been widely studied from various perspectives, its explicit use as an ellipsometry technique has not been addressed in prior works.

In this study, we therefore propose a novel "SHEL ellipsometry" approach that employs spin–orbit interaction at optical interfaces and combines it with the established framework of conventional ellipsometry. Exploiting the SHEL-based approach coupled with weak measurement provides a measurement with high sensitivity to slight variations in optical parameters at the interface. Furthermore, characterization of refractive index, thin-film thickness, and surface roughness is facilitated within a unified measurement scheme. This approach maintains a simple optical configuration while improving the robustness against systematic errors typical of conventional ellipsometry.

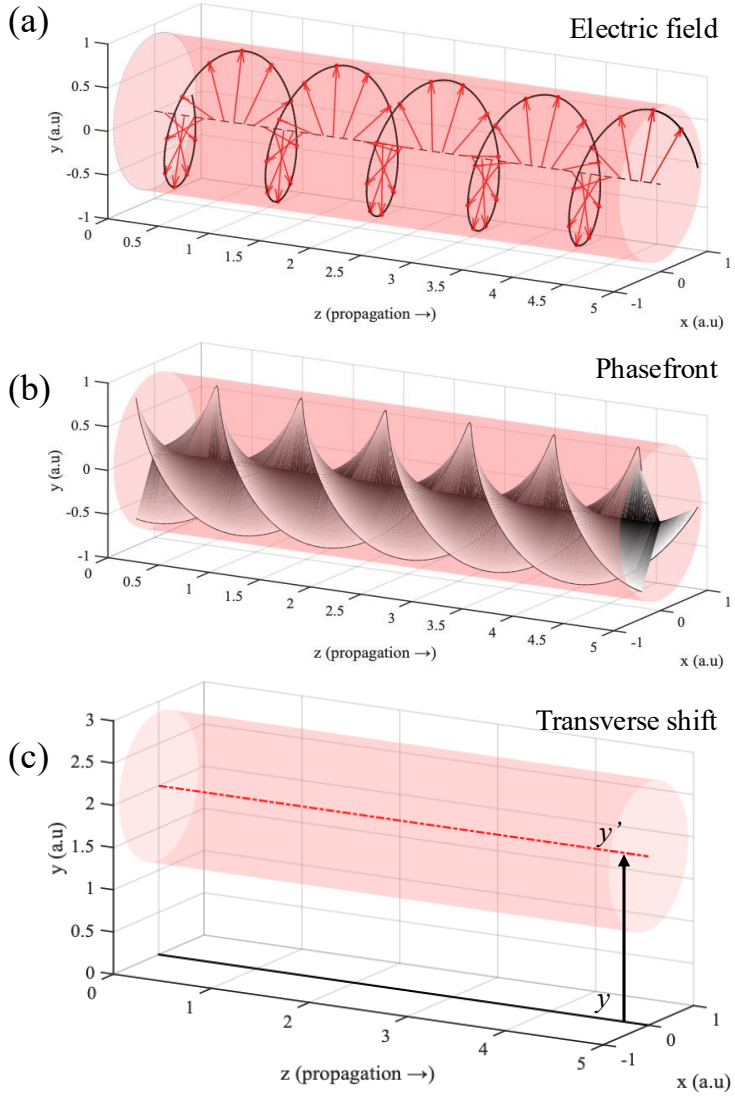


Fig. 1.4: Illustration of angular momentum of light (a) spin angular momentum corresponds to the circular polarization of the electric field, (b) intrinsic orbital angular momentum manifests as helical phase front, and (c) extrinsic orbital angular momentum is expressed physically as beam transverse shift.

1.4 Research Objectives

Building on the theoretical foundations of spin–orbit interaction discussed in the previous section, this research explores the use of spin-dependent optical beam shifts as an alternative measurement observable to conventional polarization-state-based ellipsometry. The study focuses on reflective optical configurations and emphasizes experimental feasibility, robustness, and extensibility toward two-dimensional areal measurement. In this context, a novel ellipsometry technique based on the Spin Hall Effect of Light (SHEL) is developed and investigated for high-precision optical material characterization.

The objectives of this research are as follows:

1. To analyze the theoretical framework of spin–orbit interaction in reflection geometries, with particular emphasis on the Spin Hall Effect of Light and its behavior near Brewster incidence, where polarization conversion and beam shift effects are more pronounced.

2. To design and implement a SHEL ellipsometry configuration that employs SHEL-induced beam shifts as the primary measurement observable through the weak measurement scheme, thereby eliminating the need for mechanically rotating or thermally unstable polarization elements.

3. To validate the proposed SHEL ellipsometry technique through quantitative measurement of the refractive index of known samples.

4. To validate the proposed SHEL ellipsometry and single-layer optical interface model through systematic investigation of beam shift sensitivity to variations in thin-film thickness grown with varying deposition times, and to investigate the feasibility of surface roughness characterization by relating SHEL shift responses to effective medium thickness.

5. To extend the measurement capability from pointwise sensing to two-dimensional areal mapping by raster scanning mode.

6. To explore strategies for accessing the high sensitivity measurement, particularly by exploiting the

angular dependence of SHEL near Brewster incidence, and identifying experimental parameters needed to improve the measurement.

The scope of this work is limited to reflective measurement geometries at visible wavelengths, where materials are modeled as homogeneous and isotropic media. Experimental demonstrations are conducted on bulk samples with known refractive indices, gold thin layers grown on substrates with varying deposition times, and polished surfaces with nanoscale roughness. For materials with intrinsic anisotropy, the retrieved refractive indices under this modelling assumption are interpreted as effective refractive indices. Transmission geometries, explicit anisotropic modelling, and complex multilayer stacks beyond single thin films are outside the scope of this study.

Through these objectives, this research seeks to establish a foundation for a simplified, highly sensitive ellipsometric tool based on the spin–orbit interaction of light, contributing to advancement in precision optical metrology.

1.5 Organization of the Dissertation

To address the research objectives outlined previously, this dissertation is structured to progress from the theoretical foundations to experimental validation and application of ellipsometry based on the spin–orbit interaction of light.

Chapter 1. Introduction This chapter outlines the background and motivation for this study, highlights the limitations and purpose of existing material characterization instruments, particularly conventional ellipsometry techniques, and introduces the potential of leveraging a novel physical phenomenon, the spin–orbit interaction of light, as a foundation for a novel ellipsometric approach. The research objectives and overall dissertation structure are also presented to contextualize the broader relevance of this work.

Chapter 2. Theoretical Principles This chapter provides all the theoretical foundations necessary to understand the spin–orbit interaction of light in the context of optical metrology. Key concepts include the various beam shift phenomena arising from spin–orbit coupling, the interplay between spin and orbital

angular momentum, and the relationship between beam shifts and polarization-dependent reflection properties. The weak measurement scheme is also introduced as a means of amplifying and observing beam shifts, along with the image-processing techniques used to extract beam-shift information from recorded beam profiles.

Chapter 3. Proof-of-Concept of the Spin Hall Effect of Light Ellipsometry This chapter presents the design and implementation of a SHEL-based ellipsometry technique. The experimental setup, the influence of experimental parameters on beam shift behavior, and sensitivity evaluation through refractive index retrieval are presented. Measurements involving gold thin films with varying thicknesses and polished substrates with different surface roughness levels are also discussed. Together, these results establish the feasibility and foundational performance of the proposed SHEL ellipsometry method.

Chapter 4. High Sensitivity Measurement at Near Brewster Incidence Following the proof-of-concept in the previous chapter, this chapter focuses on enhancing the measurement sensitivity by operating near the Brewster angle under horizontally polarized incident light, where the spin–orbit interaction effects are maximized. The experimental conditions required to achieve stable and reliable measurements in this regime are examined, and their performance is compared with that of conventional non-Brewster-angle operation.

Chapter 5. Conclusions The final chapter summarizes the key findings of the research, discusses the implications of the results, and outlines potential directions for future work. The chapter also reflects on the practical applicability of the proposed SHEL ellipsometry technique in optical metrology and material characterization.

A schematic overview of the thesis structure is provided in Fig. 1.5 for clarity,

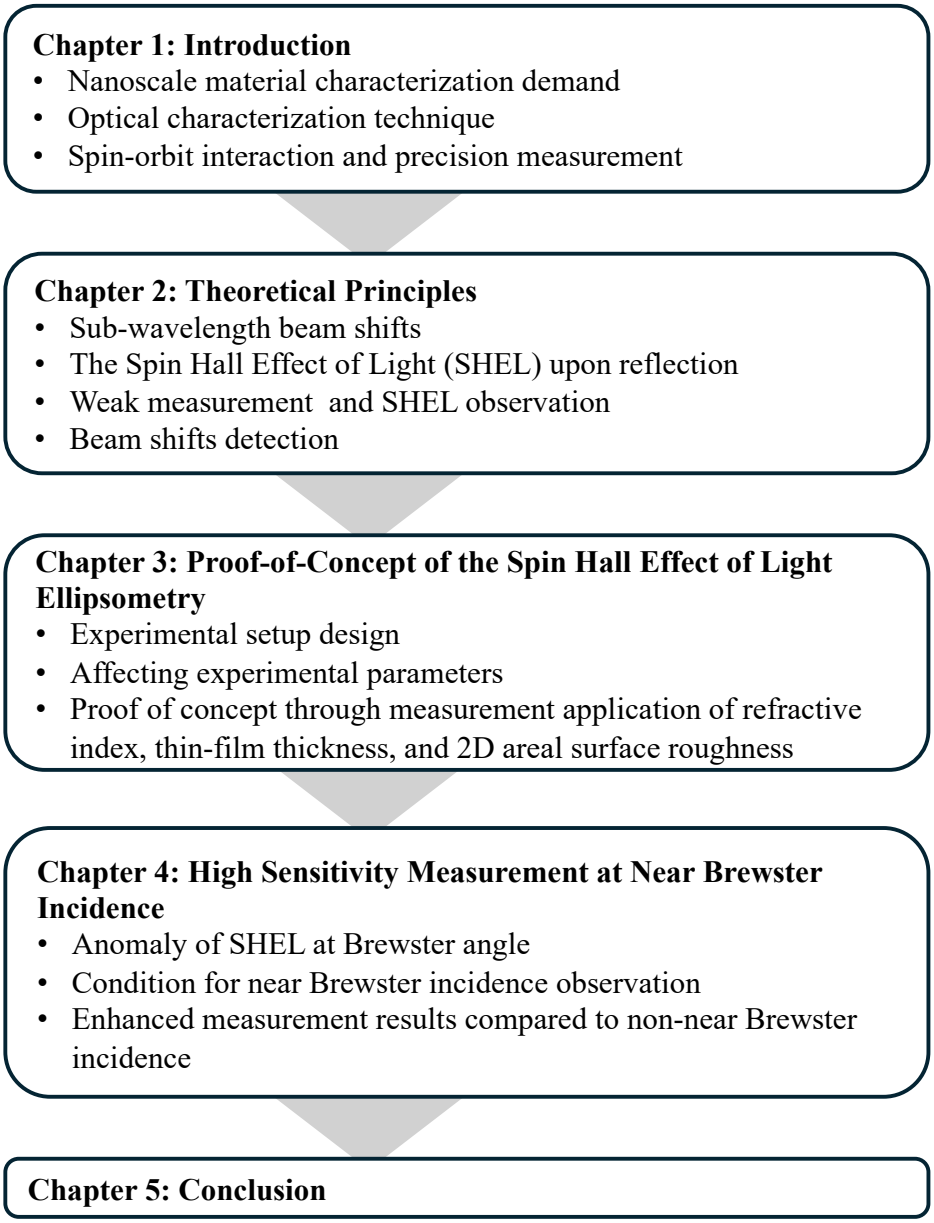


Fig. 1.5: Structure of the dissertation

Chapter 2

Theoretical Principles

2.1 Introduction

This chapter outlines the fundamental principles that support the proposed ellipsometric techniques using the spin–orbit interaction of light. The discussion begins with subwavelength beam shifts, including the Goos-Hänchen and Imbert-Fedorov effects, which describe longitudinal and transverse light displacements at dielectric boundaries. Next, the spin Hall effect of light (SHEL) is introduced as a manifestation of spin–orbit interaction. In this phenomenon, spin angular momentum associated with circular polarization couples to the beam trajectory, resulting in polarization-dependent transversal shifts. These shifts contain valuable information about the optical interface and can serve as a sensitive probe of material properties. The concept of weak measurement is introduced to access these subwavelength effects. Weak measurement theory enables amplification of small beam displacements through carefully designed pre- and post-selection of polarization states, allowing for precise determination of spin-dependent beam shifts without significant disturbance to the beam's overall structure. Subsequently, modeling of optical interfaces is presented, with an emphasis on reflection through planar boundaries. The treatment includes the Fresnel equations, polarization-dependent phase shifts, and multi-reflection effects, all of which are relevant to extracting the physical properties in the ellipsometric analysis. The chapter concludes with

the principles of beam shift detection, highlighting the conditions under which spin-dependent displacements become experimentally accessible. The relationship between these shifts and the optical properties is established, providing a theoretical basis for the SHEL ellipsometry technique described in later chapters.

2.2 Spin–Orbit Interaction and Beam Shifts

Light interaction with an interface is one of the most fundamental phenomena in optics that is present in all optical systems. It defines how light propagates between different media with different optical properties. The essential interaction of a plane wave and an interface is widely known to be governed by Snell's law and the Fresnel formula. Snell's law explains that the angle of refraction is equal to the angle of incidence, and the Fresnel formula relates the polarization amplitude between the incident and the secondary waves, whether reflection or transmission.

For a plane wave, those two well-known formulas are sufficient to describe the light interactions at the interface from a geometrical-optics perspective. However, the interactions become more complicated for a finite-width real optical beam, and those two governing laws become insufficient. In the subwavelength scale, a finite-width beam does not simply follow the geometrical optics evolution, as the beam deflects from the supposed trajectories of the secondary beam. While it happens in transmission and light reflection, this study will solely focus on the reflection phenomenon. Ever since the discoveries of these beam shift phenomena, they have attracted much attention in nano-optics studies, from material manipulation to precision measurement.

It has been summarized that the subwavelength beam shift can be divided into two, relative to the plane of incidence: the in-plane and out-of-plane shifts. Then, based on the shift types, there are the spatial and angular shifts. Commonly used terms summarize these beams into the Goos-Hänchen shift for the in-plane shift and the Imbert-Fedorov shift for the out-of-plane shift. Furthermore, there are spatial and angular GH and IF shifts, respectively [98]. For better understanding, Fig. 2.1 shows the schematic of the four beam shifts.

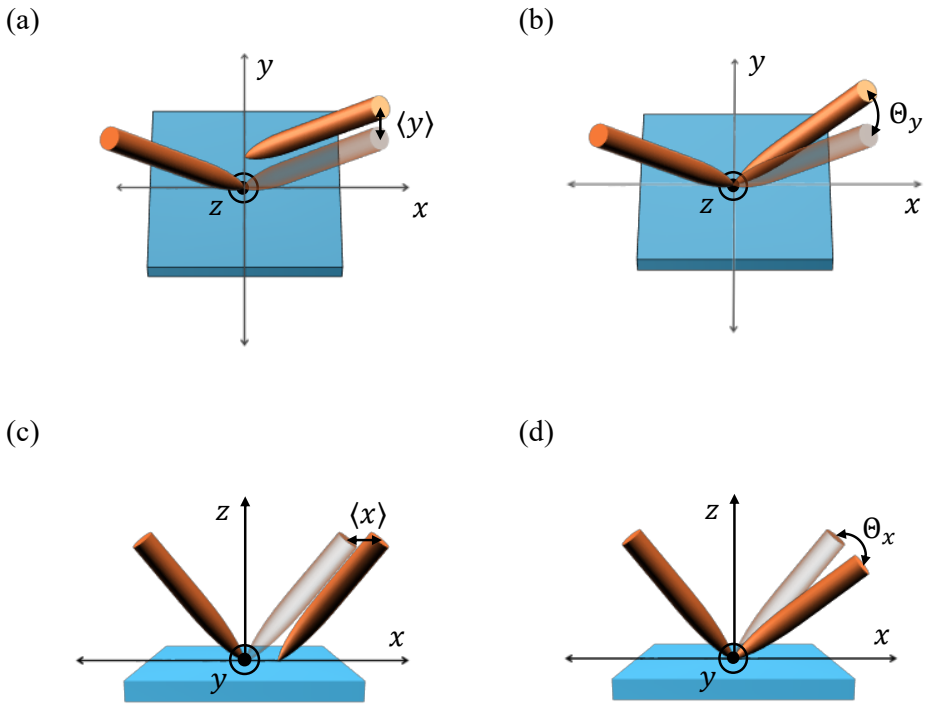


Fig. 2.1: Graphical illustration of the four sub-wavelength beam shift, (a) spatial IF shift or SHEL shift, (b) angular IF shift, (c) spatial GH shift, and (d) angular GH shift

Both GH and IF shifts depend on the polarization of the incident beams; the GH shift's eigenmodes are linear polarization, and the IF shifts have the eigenmodes of circularly polarized waves [98]. The transverse IF shifts are commonly related to the balance and conservation of light's angular momentum. In addition, Onoda et. al describe it as an instance of the Spin Hall Effect of Light (SHEL), an analogue of the Hall effect in the electronics system, where the change of the dielectric constant acts as the "force" to the light [129]. Since it occurs due to the intrinsic polarization of the incident light, which is a manifestation of the spin angular momentum, while the beam deflection is the external orbital angular momentum, the SHEL is also considered as a case of spin–orbit interaction of light (SOI) [128].

Since the SHEL is highly related to the light's angular momentum, describing the terminology and the definition surrounding it is essential. An optical beam carries several types of angular momentum. Previously, it has been mentioned that circular polarization (CP) is related to the spin component of light. The rotation of the EM fields in CP produces Spin Angular Momentum $\boldsymbol{S_z}$(SAM) where $\sigma = \pm 1$ defines the helicity of the polarization, +1 for right CP and -1 for left CP. Then there is Orbital Angular Momentum (OAM), which can be divided into intrinsic (IOAM) and extrinsic (EOAM). The IOAM is related to the helical phase front possessed by, for example, a vortex beam. The topological charge of the beam $\ell = 0, \pm 1, \pm 2, ...$ determined the IOAM $\boldsymbol{L^{Int}}$. Finally, the EOAM $\boldsymbol{L^{Ext}}$is given by the cross-product of the transverse position of the beam centre $\boldsymbol{r}$ and linear momentum $\boldsymbol{p}$ [128]. The EOAM appears as the beam shifts from the supposed trajectory.

$$\boldsymbol{S_z} = \sigma\hbar \tag{2.1}$$

$$\boldsymbol{L^{int}} = \ell\hbar \tag{2.2}$$

$$\boldsymbol{L^{ext}} = \boldsymbol{r} \times \boldsymbol{p} \tag{2.3}$$

The interaction between the SAM and EOAM produces the spin Hall effect of light, which is

polarization-dependent beam transversal shifting. The following subsection explains the SHEL in detail.

2.3 The Spin Hall Effect of Light upon Reflection

A linearly polarized light incident on an optical interface will be reflected as a different handedness of circularly polarized light and deflected from its supposed trajectory [130]. Historically, this transverse shift was first predicted theoretically by Fedorov, stating that, besides the longitudinal shift, there is also a transverse shift when a circularly polarized beam undergoes total internal reflection [134]. It wasn't explainable by classical optical geometries, and later Imbert provided the first experimental proof of it, establishing the effect as a real and measurable phenomenon, which led to what is now known as Imbert-Fedorov shift, a manifestation of SOI [135]. Subsequently, Onoda's modern interpretation of IF as SHEL, connecting the phenomenon to the Berry phase, and later Bliokh et al., completed the theoretical definition [129, 136]. SHEL can be described by the interplay between SAM and EOAM, which is governed by total angular momentum conservation laws, where the total angular momentum (TAM) remains constant. TAM of a polarized wave packet $\boldsymbol{J}$ consists of intrinsic spin $\boldsymbol{S_z}$ and the orbital angular momentum $\boldsymbol{L^{Ext}}$. Thus, any change in one part will affect another. Figure 2.2 shows the SHEL upon reflection from an optical interface.

$$\boldsymbol{J_z} = \boldsymbol{r} \times \boldsymbol{k} + \langle \boldsymbol{\Psi} | \hat{\sigma}_3 | \boldsymbol{\Psi} \rangle \boldsymbol{k}/k \tag{2.4}$$

$$\boldsymbol{J_i} = \boldsymbol{J_r} = constant \tag{2.5}$$

Therefore,

$$S_r - S_i = L_r - Li \tag{2.6}$$

The EOAM of incident light is zero because the $\boldsymbol{r}$ and $\boldsymbol{k}$ of the incident light are within the $y = 0$

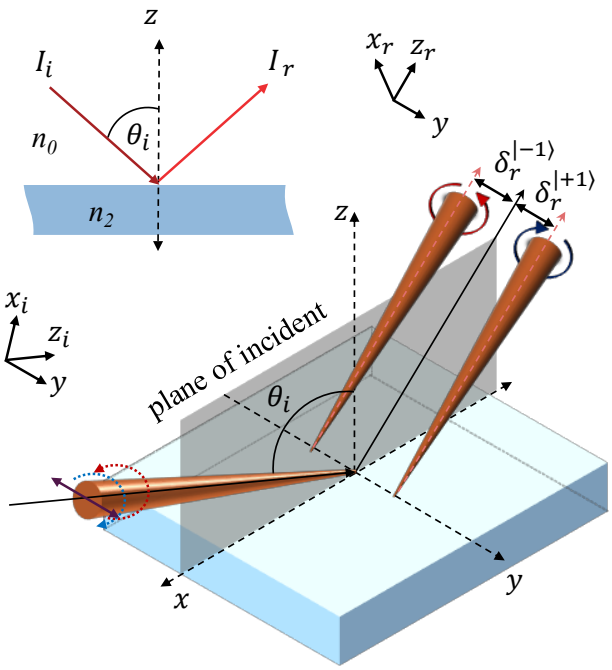


Fig. 2.2: Principle of the Spin Hall Effect of Light (SHEL) upon reflection off an interface, decomposed circular polarizations component displaced at a distance of δ_r from the supposed reflection trajectories at the same plane of the incidence.

plane [129]. From Snell's law, it is known that $n_0 sin\theta_i = n_2 sin\theta_t$ and $\theta_r = \pi - \theta_i$.

$$\langle \Psi_r | \hat{\sigma_3} | \Psi_r \rangle \cos\theta_r - \langle \Psi_i | \hat{\sigma_3} | \Psi_i \rangle \cos\theta_i = k_0 \sin\theta_i \delta_r \tag{2.7}$$

Therefore, the transverse shift of light can be defined as

$$\delta_r(\theta_i) = \frac{\langle \Psi_r | \hat{\sigma_3} | \Psi_r \rangle - \langle \Psi_i | \hat{\sigma_3} | \Psi_i \rangle}{k_0 \tan\theta_i} \tag{2.8}$$

This equation establishes the explicit formula for the transverse shift at the interface (SHEL), which shows its polarization dependence. The Pauli matrix $\hat{\sigma_3}$ distinguishes the right and left circular polarization. The sign and magnitude of the shift directly depend on the handedness of the polarization. In the case of linearly polarized incidence, which is an equal superposition of RCP and LCP, it is decomposed into opposite transverse directions upon reflection. Without polarization analysis, it will not result in a net shift. Furthermore, the general derivation of a transverse beam upon horizontal and vertical linear polarizations is defined as follows [137]:

$$\delta_r^H = \mp \frac{1 + r_s/r_p}{k_0 \tan\theta_i} \tag{2.9}$$

$$\delta_r^V = \mp \frac{1 + r_p/r_s}{k_0 \tan\theta_i} \tag{2.10}$$

This equation shows that the transverse shift depends on light polarization through the Fresnel complex coefficient, which is affected by the interface properties, enabling both control of light behavior and characterization of materials. Since the beam shift is related to the incident and reflected polarization, and how reflection of linear polarized incidence requires polarization analysis, it resembles the ellipsometry principle. Despite being subwavelength ($\delta_r \approx 1/k_0$), the shift offers a novel method for probing various physical properties. These conditions naturally motivate the use of a weak measurement techniques that enable amplification of the tiny SHEL shift to a detectable scale, a subject discussed in

the following section.

2.4 Weak Measurement Approach to the Spin Hall Effect of Light

2.4.1 Conventional Weak Measurement

As previously mentioned, the SHEL shift is in fractions of a wavelength, which makes observation a challenge. Without proper technique, it can not be observed. Several methods to observe and measure the SHEL shift exist. It can be done via interferometry, but the most explored one is polarization analysis-based, such as by polarimetric or intensity ratio of cross-polarizer [138, 139]. One of the widely used techniques to access the beam shift is by applying the weak measurement. Weak measurement for SHEL shift observation was first demonstrated on transmission, but ever since it has become the milestone for direct observation of SHEL [140]. The weak measurement itself was first introduced by Aharonov et al as a quantum measurement technique that introduces complex amplification known as the weak value A_w to a system with weak coupling between the observable $\hat{A}$ and the probe [141].

$$A_w = \frac{\langle \Psi_f | \hat{A} | \Psi_i \rangle}{\langle \Psi_f | \Psi_i \rangle} \tag{2.11}$$

In the weak measurement formalism, the observable of interest ($\hat{A}$) belongs to the system, and the probe is described by a continuous degree of freedom, which is the photon polarization and the transverse position of the optical beam for the SHEL case, respectively. The coupling between the system and probe is governed by the interaction Hamiltonian ($\hat{H}$) and the resulting time evolution is expressed by a von Neumann-type unitary operator ($\hat{U}$).

$$\hat{H} = g\hat{A} \otimes \hat{p} \tag{2.12}$$

$$\hat{U} = \exp(-ig\hat{A} \otimes \hat{p}) \tag{2.13}$$

where $\hat{p}$ is the momentum operator of the probe and g is the coupling strength.

In the SHEL case, $\hat{A}$ can be identified $\hat{\sigma_3}$, the Pauli operator that explains the left and right circular polarizations, $\hat{p}$ equal to k_y, the transverse momentum of the beam, and the coupling strength is given by the small spin-dependent displacement δ_r. Thus, the interaction in (2.13) can also be expressed in waveform formalism as

$$\hat{U} = \exp -ik_y\hat{\sigma_3}\delta_r \tag{2.14}$$

Since δ_r is small, the unitary operator can be expanded into a first-order expansion as

$$\hat{U} \approx 1 - ik_y\hat{\sigma_3}\delta_r \tag{2.15}$$

In general, the procedure of applying weak measurement consists of three steps: (i) preselection of the initial state $|\Psi_i\rangle$, (ii) weak interaction between system and probe, and (iii) postselection of the final state in a nearly orthogonal state $|\Psi_f\rangle$. Thus, after preselection and postselection, the Gaussian pointer wavefunction $|\Phi\rangle$ acquires the form

$$\langle\Psi_f|\hat{U}|\Psi_i\rangle \approx \langle\Psi_f|\Psi_i\rangle(1 - ik_yA_w\delta_r)|\Phi\rangle \tag{2.16}$$

which can be understood as the shifting of the Gaussian beam by an amount of $A_w\delta_r$ in the practical sense.

Applied to the SHEL, these steps have direct physical meaning: the preselected state corresponds to the incident polarization, the weak interaction is the small spin-dependent displacement δ_r acquired upon reflection, and the postselected state is determined by the analyzer projecting the reflected polarization. The measured outcome is then the displacement of the beam centroid, which carries the weak value amplification.

For SHEL, the incident light is a linearly polarized Gaussian beam defined in the circular polarization eigenmodes. For example, with a pure horizontally polarized incidence beam as the pre-selected state,

then the post-selected state is $V \pm \varepsilon$.

$$|\Psi_i\rangle = |H\rangle = (|+\rangle + |-\rangle)/\sqrt{2} \tag{2.17}$$

$$|\Psi_f\rangle = -\frac{1}{\sqrt{2}}(e^{-i\varepsilon}|+\rangle - e^{i\varepsilon}|-\rangle) \tag{2.18}$$

Using the state definitions, the numerator and denominator of (2.11) become

$$\langle\Psi_f|\hat{A}|\Psi_i\rangle = \frac{i}{2}(e^{i\varepsilon} + e^{-i\varepsilon}) = i\cos\varepsilon \tag{2.19}$$

$$\langle\Psi_f|\Psi_i\rangle = \frac{i}{2}(e^{i\varepsilon} - e^{-i\varepsilon}) = -\sin\varepsilon \tag{2.20}$$

Thus, the weak value is obtained as:

$$A_w = -i\cot\varepsilon \tag{2.21}$$

Equation (2.21) follows directly from the general weak value definition in (2.11), specialized to the SHEL case. The parameter ε is called the post-selected angle or azimuth angle, corresponding to the small deviation added to the post-selected state that determines the degree of near-orthogonality between preselected and postselected states.

Applying the weak value to the SHEL shift amplifies the subwavelength beam shift. In addition, the observed amplified beam shift also considers the free evolution of Gaussian beam propagation at any given plane of z with an amplification factor denoted by $F = z/z_R$, where z_R is the Rayleigh length. Finally, the observed amplified beam shift can be defined as

$$\delta_{Aw} = F|A_W|\delta_r \tag{2.22}$$

Where δ_r is the original spin-dependent displacement at the interface.

Equation (2.22) shows that the SHEL shift is amplified by two factors, the weak value A_w and the free space propagation factor F. For example, upon $|H\rangle$ incident, the observed amplified beam shift can be obtained by substituting equation (2.9) into (2.22). Similarly, the same can be done for $|V\rangle$ incident.

$$\delta_{Aw}^{H} = \frac{z(r_p + r_s)\cot\varepsilon}{z_R k_0 \tan\theta_i r_p} \tag{2.23}$$

$$\delta_{Aw}^{V} = \frac{z(r_p + r_s)\cot\varepsilon}{z_R k_0 \tan\theta_i r_s} \tag{2.24}$$

2.4.2 Modification to the Weak Measurement

The expression in (2.22) represents the conventional weak measurement prediction, valid under the condition that $|A_w\delta_r| \ll w$, where w is the beam width and the weak interaction regime is satisfied. When this condition is satisfied, the Gaussian pointer wavefunction remains undistorted, and (2.22) holds. While most systems employing weak measurement are usually done in a weak regime, conventional weak measurement with first-order expansion is sufficient. When it's not satisfied, higher orders should not be neglected [142]. In the SHEL shift case, the weak regime is not always satisfied. When the incident angle approaches the Brewster angle (for $|H\rangle$), making δ_r large or if the pre- and post-selected states are nearly orthogonal, making $|A_w|$ large, the validity condition fails and (2.22) becomes inaccurate [143]. Those limitations motivate the introduction of several modifications to increase the accuracy of the weak measurement model for SHEL observation.

The modifications can be conducted using the second-order weak measurement, the expansion of the angular dependent reflection properties, and so on [144–147]. Chen et.al introduce the modified weak measurement where it does not use the truncated first-order expansion (2.15) and consider the angular dependency of reflection coefficient ($\partial r_p/\partial\theta_i$), particularly to overcome the divergence of the model for $|H\rangle$ at Brewster angle. Qin et al. modify the model by introducing not only the expansion of the Fresnel coefficient but also expanding the model to provide for arbitrary polarization and universal samples. In

this work, to improve the weak measurement model, the non-approximation of the unitary operator is applied, similar to what is introduced in Ref. [145], but the expansion of the Fresnel coefficient for $|H\rangle$ is omitted to avoid model complexity.

The non-approximation version of the weak measurement model in (2.16) can be expressed as

$$\langle\Psi_f|\hat{U}|\Psi_i\rangle \approx \langle\Psi_f|\Psi_i\rangle[\cos(k_y\delta_r) - iA_w\sin(k_y\delta_r)]|\Phi\rangle \tag{2.25}$$

This expression can be interpreted as a Gaussian pointer displaced by an effective amount $\delta^r_{Amod} = A^{mod}_w\delta_r$. Therefore, the modified weak amplified beam shift for $|H\rangle$ and $|V\rangle$ can be expressed as δ^H_{Amod} and δ^H_{Amod}.

$$\delta^H_{Amod} = \frac{zr_p(r_p + r_s)\sin(2\varepsilon)\cot\theta_i}{(r_p + r_s)^2\cos^2\varepsilon\cot^2\theta_i + 2k_0r_s^2z_R\sin^2\Delta} \tag{2.26}$$

$$\delta^V_{Amod} = \frac{zr_s(r_p + r_s)\sin(2\varepsilon)\cot\theta_i}{(r_p + r_s)^2\cos^2\varepsilon\cot^2\theta_i + 2k_0r_p^2z_R\sin^2\Delta} \tag{2.27}$$

Notice that (2.26) is similar to Eq. (27) in ref. [145] resulted from omitting the angular dependence of r_p ($\partial r_p/\partial\theta_i$), while (2.27) is the same as Eq. (29).

2.4.3 Experimental Implication of Weak Measurement in SHEL Observation

Experimentally, the weak measurements in observing the SHEL shift can be easily implemented by a pair of polarizers in the incident and reflection trajectories. A polarizer in the incident beam trajectory is used to define the pre-selected state $|\Psi_i\rangle$, for $|H\rangle$, the polarizer is set at 0°. The second polarizer, put in the reflected beam trajectory, is then set almost perpendicular to the first polarizer $|V \pm \varepsilon\rangle$ or $90° \pm \varepsilon$ to define the post-selected state $|\Psi_f\rangle$. As stated in the previous subsection, the post-selected angle ε determines the weak value amplification. Intuitively, the post-selected angle is relatively small, usually less than 5°. Figure 2.3 shows the schematic of the polarizer pair in the implementation of the weak measurement.

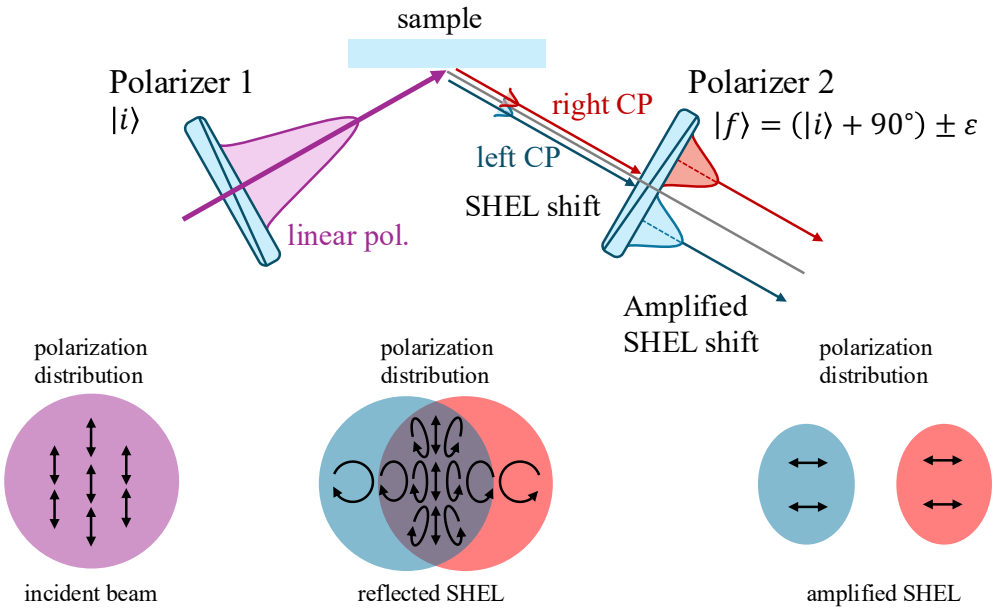


Fig. 2.3: Pair of polarizers defining the initial and final polarization state in a weak measurement scheme to amplify and observe the SHEL shift.

As mentioned earlier, in the occurrence of SHEL, the reflected light is of a different handedness of circularly polarized light. Therefore, using the weak measurement configuration, when the polarizer pair is in the cross-polarized state, the symmetrical splitting of the beam helps observe the occurrence of SHEL clearly. Figure 2.3 illustrates the pair of polarizers realizing the weak measurement scheme. The first polarizer (P_1) defined the initial state $|\Psi_i\rangle$, it can be $|H\rangle$, $|V\rangle$, diagonal, or even arbitrarily linear polarization. Upon reflection from the sample, the subwavelength SHEL shift occurs and goes through the second polarizer (P_2) that priorly set to define the final state $|\Psi_f\rangle$. Due to the weak value, the SHEL shift is significantly amplified after P_2. Additionally, the cross-polarizer state is when the pair of polarizers is perpendicular to each other $\langle\Psi_f|\Psi_i\rangle = 0$. As the CP components intersect, shown in the polarization distribution on the inset of Fig. 2.3, because the P_2 is perpendicular to P_1, the center part of the intersection will be canceled out, and symmetrical lobes with equal intensity are observed after P_2. This phenomenon is significantly apparent at the detector, making SHEL observation easier. When the two lobes of the two CP components are observable, it confirms the occurrence of SHEL upon reflection.

As previously stated, in weak measurement, a small deviation angle denoted by ε is essential in measuring the beam shift. SHEL observation with weak measurement is not done in a cross-polarizers configuration but with the addition of ε at P_2. The sign of ε defines the direction of the beam shift in y direction relative to the reference point. Figure 2.4 shows the schematic of ε addition and how it affects the observed intensity of the beams shift. In the cross-polarized state, $\varepsilon = 0$, the two symmetrical lobes can be observed, and the intensity is significantly low, due to cross-polarization, but still observable. The distance between two peaks of these lobes is $2A_w\delta_r$ as shown in Fig. 2.4 (a). Adding a small deviation angle ε will result in a prominent dominant peak with the sign of ε corresponding to the shifting direction of the centroid, as shown in (b) for a positive sign and (c) for a negative sign of ε, respectively. A particular distorted state happens when two asymmetrical lobes are observed, as presented in (d), which occurs when ε is so small that it makes the polarizer pair almost perpendicular. This distorted state should be avoided at all costs during measurement, as it can alter the accuracy of the beam shift measurement. When this distorted state is observed, it can be implied that the applied ε is

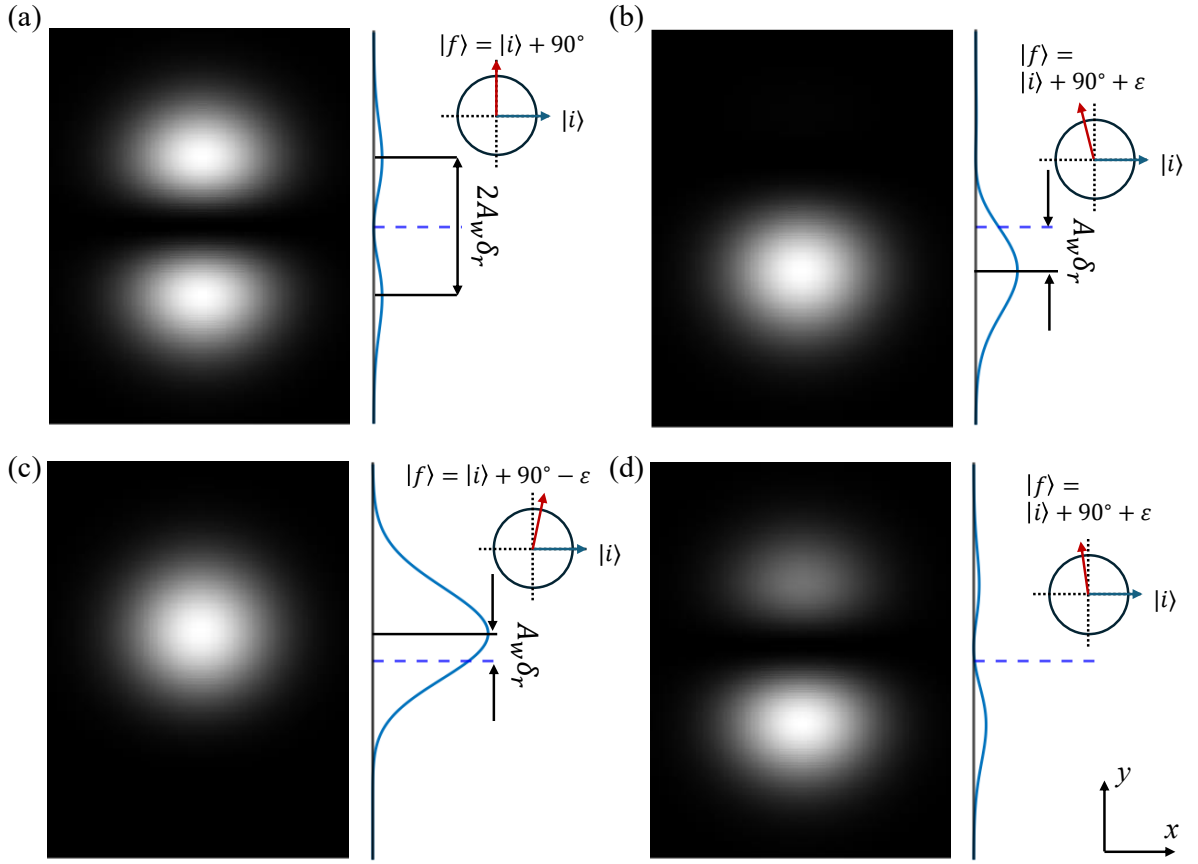


Fig. 2.4: Implication of ε value to the observed intensity of SHEL shift, (a) $\varepsilon = 0$, (b) $+\varepsilon$, (c)$-\varepsilon$, (d) distorted state when ε is too small and $\langle f|i\rangle \approx 0$

insufficient for measurement, and a larger value should be chosen.

2.5 Beam Propagation Factor

As mentioned in 2.4.1, the observed shift after weak measurements also includes the propagation factor. In the previous section, the amplified beam shift is explained from the point of view of where the phenomenon happens, which is at the interface. It uses the beam parameter w_0, which is the minimum beam waist, assumed to occur when the beam impinges at the interface. The formula specifically focused only on the part of the weak measurement, meaning it does not explain the whole optical system, which

may include several lenses. From the instrument design point of view, modeling the optical system became essential by considering the lens system that defines the amplification of an optical system. For SHEL reflection observation, a pair of telescopic lenses is commonly employed where the focal length of the first lens is shorter than the second one ($f_1 < f_2$). Derivation of the beam propagation factor is explained by considering the pair of lenses included in the setup. The final model of SHEL ellipsometry will help determine the optical system design and the desired amplification factor based on the specification of the laser beam diameter and the focal length of the lenses. Figure 2.5 shows the relation of Gaussian beam propagation without a lens system in (a) and Gaussian beam propagation with a telescopic lens system in (b). The first assumption in SHEL, upon reflection, is that the minimum waist (w_0) occurs at the interface, which is also where $z = 0$.

The beam propagation factor is widely understood as [148, 149]

$$F = \frac{z}{z_R} \tag{2.28}$$

Where z is the effective propagation length after reflection from the interface and $z_R = k_0 w_0^2/2$is the Rayleigh length. In practice, when using the telescopic lens, the minimum beam waist is the waist of the focused beam by L_1, then w_0 can be expressed as a function of the focal length of L_1 and beam spot size at the output of the Laser (w_{out} or D_{out}). The effective propagation distance z is equal to the focal length of the collimating lens, denoted by f_2.

$$w_0 = \frac{2f_1}{k_0 w_{out}} = \frac{4f_1}{k_0 D_{out}} \tag{2.29}$$

Then, z_R becomes

$$z_R = \frac{k_0 w_0^2}{2} = \frac{2f_1^2}{k_0 w_{out}^2} = \frac{8f_1^2}{k_0 D_{out}^2} \tag{2.30}$$

Substituting (2.30) to (2.28), the beam propagation factor can be expressed as a function of instrument parameters f_1, f_2, andw_{out} or D_{out}.

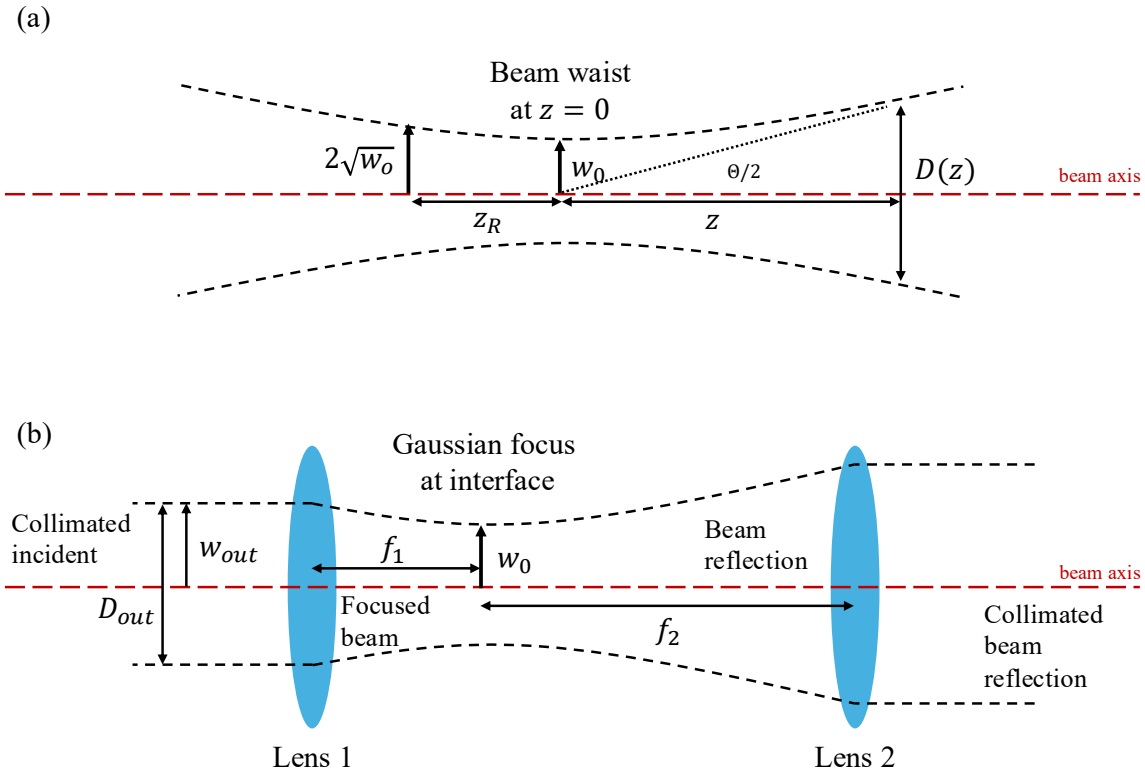


Fig. 2.5: Propagation factor of Gaussian beam (a) in free space, and (b) in a telescopic lens system.

$$F = \frac{k_0 f_2 w_{out}^2}{2 f_1^2} = \frac{k_0 f_2 D_{out}^2}{8 f_1^2} \tag{2.31}$$

2.6 Optical Interface Model

The physical properties being measured by SHEL ellipsometry can be retrieved based on the particular model of the optical interface. Additionally, understanding the light-matter interaction at material boundaries is central to the interface modeling for accurate parameter retrieval using SHEL ellipsometry. The interface defines the reflection, transmission, and phase evolution of the probing light. In practice,

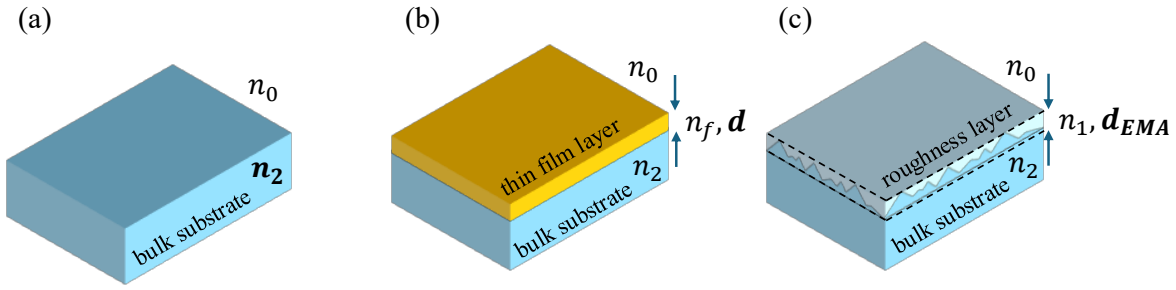


Fig. 2.6: Optical interface models, (a) air-glass, (b) thin film layer, and (c) roughness layer

three levels of interface complexity are commonly encountered and used in this work. From the simplest interface model, which is the air-glass interface, a thin film layer in between two parallel planar boundaries, and surface roughness that modifies the boundary into an effective transition medium, as displayed in Fig. 2.6. Each case can be modeled to provide the basis for the interpretation of physical parameters from the detected SHEL shift.

When using the simplest optical interface model, the air-glass model, the light interacts at the interface between two homogeneous isotropic media, consisting of the ambient (air) and a denser medium (glass/substrate), where light travels from a less dense medium to a denser medium. In the air-glass model, it is assumed there is no roughness in the second medium. For this kind of interface, the ellipsometry parameter is defined as the ratio of the Fresnel reflection coefficient of p to s.

$$\rho = r_p / r_s \tag{2.32}$$

With r_p and r_s being the complex Fresnel reflection coefficients.

$$r_s = \frac{n_0 \cos\theta_i - n_2 \cos\theta_t}{n_0 \cos\theta_i + n_2 \cos\theta_t}; r_p = \frac{n_2 \cos\theta_i - n_1 \cos\theta_t}{n_2 \cos\theta_i + n_0 \cos\theta_t} \tag{2.33}$$

Where n_0 and n_2 correspond to the refractive indices of the incident and transmitted media, respectively. The transmission angle can be resolved as the incidence angle and the refractive indices using

Snell's law:

$$n_0 \sin\theta_i = n_2 \sin\theta_t . \tag{2.34}$$

However, this holds for the assumption that both n_0 and n_2 are transparent non-absorbing media. Previously, in (2.9)-(2.10), besides depending on the incident angle, the SHEL shift amplitude also depends on the ratio of the complex Fresnel ratio. Thus, plugging the Fresnel formula and Snell's law into (2.9)-(2.10) enables the retrieval of refractive index from the measured shift, denoted as the "pseudo" refractive indices.

Moving forward to a more complex but realistic interface, which is the thin film layer model, where the optical interface consists of two planar boundaries: air-film and film-substrate boundary, which are also denoted as 01 interface and 12 interface. The sample is a thin film layer (thickness d, refractive indices n_1 deposited on a bulk substrate of refractive index n_2 as shown in Fig. 2.6 (b). Light incident from medium n_0 to the thin film surface, the optical response cannot be described by a single reflection event, but rather by the coherent superposition of multiple reflections and transmissions from the two parallel interfaces enclosing the film.

Consider a thin film thickness of d and refractive index of n_f between an ambient medium n_0 and a bulk substrate n_2. The incident light first encounters the air-film interface, then undergoes a partial reflection and transmission, and then propagates through the film and again undergoes partial reflection at the film-substrate boundary, where part of it is transmitted to the semi-infinite substrate. This repeats indefinitely, producing a series of reflected waves as illustrated in Fig. 2.6. If the complex Fresnel coefficient at each boundary is denoted as $r_{01p,s}, r_{12p,s}, t_{01p,s}, and t_{12p,s}$, then the final reflection coefficient r_{012} resulting from the air-film-substrate layer can be expressed as

$$r_{012} = r_{01} + t_{01}t_{10}r_{12}e^{-i\alpha} + t_{01}t_{10}r_{10}r_{12}^2 e^{-i2\alpha} + t_{01}t_{10}r_{10}^2 r_{12}^3 e^{-i3\alpha} + \ldots \tag{2.35}$$

This effective reflection coefficient can be compactly expressed due to $r_{01} = -r_{10}$ and $t_{01}t_{10} = 1 - r_{01}^2$

as

$$r_{012} = \frac{r_{01} + r_{12}e^{-i\alpha}}{1 + r_{01}r_{12}e^{-i\alpha}} \tag{2.36}$$

with α corresponds to 2β, the phase thickness of the film d, and θ_1 is the internal propagation angle inside the film that can be obtained via Snell's law.

$$\alpha = 2\beta = \frac{4\pi}{\lambda} n_f d \cos\theta_1 \tag{2.37}$$

$$n_0 \sin\theta_i = n_f \sin\theta_1 = n_2 \sin\theta_2 \tag{2.38}$$

The ellipsometer parameter remains as the ratio of the Fresnel reflection coefficient of the p to the s component. Therefore, for a thin film layer, ρ is defined as

$$\rho = \frac{r_{012,p}}{r_{012,s}} = \frac{(r_{01,p} + r_{12,p}\chi)(1 + r_{01,s}r_{12,s}\chi)}{(r_{01,s} + r_{12,s}\chi)(1 + r_{01,p}r_{12,p}\chi)} \tag{2.39}$$

where χ replaces the $\exp -i\alpha$ carrying the film layer thickness and refractive indices information, in this case, by knowing the refractive indices of air, thin film, and bulk layer, the film thickness can be retrieved based on (2.39) from SHEL shift measurement. This time, the refractive index of the medium can be complex, but it is all assumed homogeneous and optically isotropic, smooth (without roughness), and non-amplifying. Another condition to be met in applying this model is that the lateral dimension of the film must be significantly larger than the thickness to assume the multiple reflection and transmission are infinite [77].

Figure 2.7 displays the single-layer interface on parallel-plane boundaries, illustrating the oblique reflection by the thin film layer and the EMA roughness layer model. While the incident angle at the ambient is denoted by θ_i, which also corresponds to the experiment setup, θ_1 and θ_2 correspond to the angles of refraction in media 2 and 3, respectively.

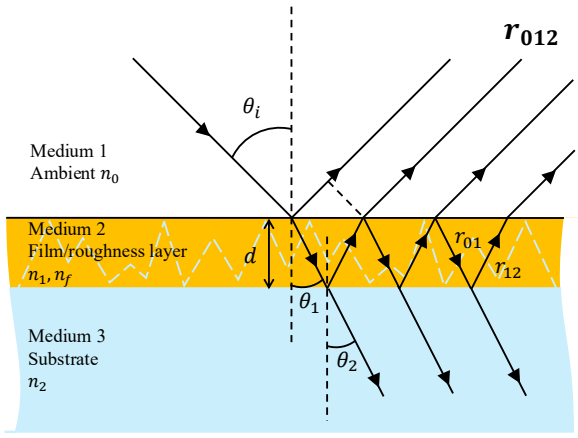


Fig. 2.7: Oblique reflection by a single layer (thin film or EMA roughness layer) with parallel-plane boundaries.

However, no real surface is perfectly smooth. Nanoscale surface roughness alters scattering and reflection behavior, making the direct application of the Fresnel model complicated. Additionally, as surface roughness can be considered random, it is rather impossible to model the light interaction geometrically. In ellipsometry, initially, it was only for the measurement of refractive index and film thickness. Later, it is also discovered that it is sensitive to the surface roughness. Surface roughness with a tenth of a wavelength can be modeled as a homogeneous effective medium layer with its own effective thickness and refractive index. Therefore, the roughness can be modeled similarly to the film thickness model. However, unlike in the thin film model where n_f is known, for surface roughness measurement, the refractive index n_1 is not known but assigned based on the Effective Medium Approximation (EMA). There are several EMA models; Bruggeman EMA is particularly well-suited for modeling surface roughness, where the roughness layer is treated as the composite of air and bulk material. The effective dielectric function of the roughness layer ϵ_{eff} is defined by solving (2.40), where f_a and f_b are the volume fraction of air and bulk substrate, and ϵ_a, ϵ_b are their respective dielectric functions [150]. For

the roughness layer, commonly the volume air fraction is $f_a = 0.5$ where $f_a + f_b = 1$. Then the effective roughness layer refractive index is taken as the square root of the ϵ_{eff}.

The homogenization of the roughness layer reflects the idea that probing light "averages" or "integrates" over inhomogeneities smaller than the wavelength. The thickness d_{EMA} assigned to the EMA layer is often considered proportional to the RMS roughness height. Thus, a point value of d_{EMA} reflects the RMS height of the area exposed by the beam cross-section on the interface.

$$f_a \frac{\epsilon_a - \epsilon_{eff}}{\epsilon_a + 2\epsilon_{eff}} + f_b \frac{\epsilon_b - \epsilon_{eff}}{\epsilon_b + 2\epsilon_{eff}} = 0 \tag{2.40}$$

$$n_1 = n_{eff} = \sqrt{\epsilon_{eff}} \tag{2.41}$$

By plugging this EMA concept into the thin-film formalism described previously, the reflection coefficient can be calculated as if the surface roughness were a homogeneous thin film with its effective index n_1. This approach has been extensively validated and is a standard operation in conventional ellipsometry; thus, it is rational to also embed this concept in SHEL ellipsometry, where the reflection coefficient modifies the SHEL shift. The physical parameter being observed can then be retrieved by solving the equation using the appropriate ρ.

2.7 Definition and Detection of the Beam Shift

Discussion over the theoretical foundation of the SHEL shift to the interface model has been carried out. Still, it is as important to understand the practical definition of the beam shift detection. In SHEL observation, the reflected beams are recorded by a CCD camera. Intuitively, SHEL shift is the $y$direction displacement of the beam's centroid measured relatively to a fixed reference coordinate, which acts as the supposed reflection trajectories, obtained from a two-lobe cross-polarized condition as illustrated in Fig. 2.8. All quantities are defined on the recorded intensity maps $I_\varepsilon(x, y)$ at setting ε.

It is important to construct a reference point by recording images at cross-polarized state ($\varepsilon = 0$)

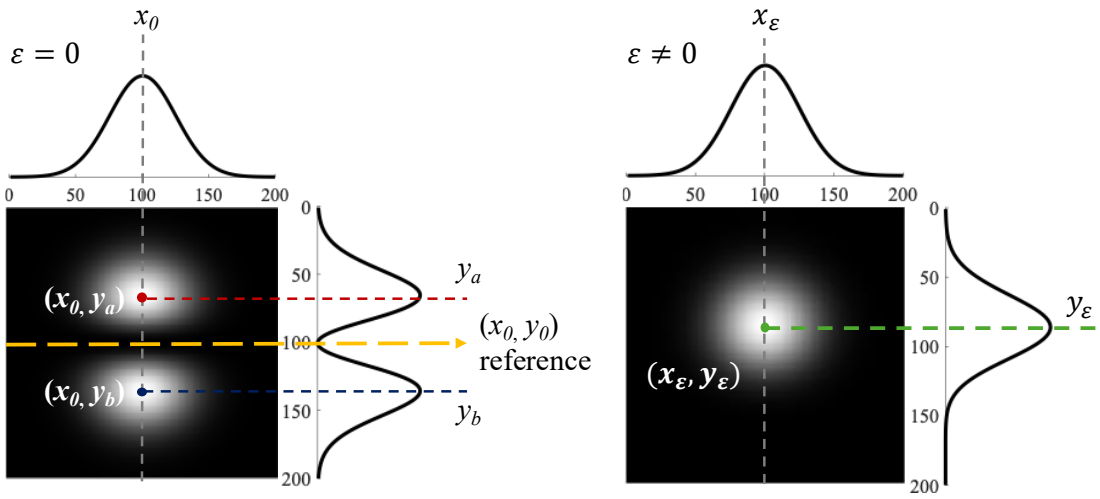


Fig. 2.8: Definition of SHEL beam shift based on the recorded images, based on experimental procedures, and ε value. Cross-polarizer ($\varepsilon = 0$) images are used to define the reference point and shifted beam centroid ($\varepsilon \neq 0$) y_ε distance to the reference y_0 is defined as the detected amplified SHEL shift.

where symmetrical intensities of two lobes are observed in $I_0(x, y)$. First step is to locate the global maximum $(x^*, y^*) = \arg\max I_0(x, y)$. Then fixing $x = x^*$, the one-dimensional row profile is extracted $I_{0y}(y) = I_0(x^*, y)$. From here, to suppress the noise while preserving the lobe locations, by specifying smoothing parameter p and weights w_i, a smoothing spline fitting is constructed $s(y)$ by minimizing (2.42) [151]

$$p \sum_i w_i (I_{0y}(y) - s(y))^2 + (1 - p) \int (\frac{d^2 s}{dx^2}) dx. \tag{2.42}$$

Then, two local maxima of $s(y_i)$ with the largest intensity at y_a and y_b are the peaks of the lobe. Therefore, the reference point is then set as (x_0, y_0).

$$x_0 = x^*; y_0 = \frac{y_a + y_b}{2} \tag{2.43}$$

Following the construction of the reference point is the centroid detection of beam shifts at nonzero

ε. For each image $I_\varepsilon(x, y)$ recorded, only the value of ε changes at P_2, therefore, no change of alignment is expected at the detector. Similarly to the $\varepsilon = 0$, all $y-$ data profiles are extracted at $x = x^*$ of located global maxima $I_{\varepsilon y} = I_\varepsilon(x^*, y)$. At a nonzero ε recording, it is expected to contain a single beam profile leading to a simple centroid detection via Gaussian fitting with a as amplitude, c related to the peak width, and y_ε is the centroid location [152]. Then the centroid is located at (x^*, y_ε).

$$g(y) = a \exp\Big[- (\frac{y - y_\varepsilon}{c})^2 \Big] \tag{2.44}$$

From here, the SHEL shift can be obtained by calculating the distance in the y-direction between the beam shift and the reference point. The sign of δ_ε defines the motion direction of the beam shift relative to the reference point. Since δ_ε is in pixel value, multiplying it by the camera's pixel size retrieves the measured amplified SHEL shift (δ_{Amp}) the Then, the resulting shift can be further used for the analysis and extraction of physical parameters. The process is summarized in Fig. 2.9 with the yellow block representing the reference construction ($\varepsilon = 0$) and the green block representing the nonzero ε process.

$$\delta_\varepsilon = y_0 - y_\varepsilon \tag{2.45}$$

2.8 SHEL Ellipsometry Framework

By unifying the concepts of SHEL, weak measurement, propagation factor, and interface modelling previously explained, the measurement can be formalized into a single framework. This framework, referred to as the SHEL ellipsometry model, expresses the polarization-dependent shift in terms of the optical and material parameters of the interface by also considering the hardware parameter through the beam propagation factor. The SHEL ellipsometry model used in this work consists of two models: (i) based on the conventional weak measurement, and (ii) based on the modified weak measurement.

The SHEL ellipsometry model based on the conventional weak measurement is given by

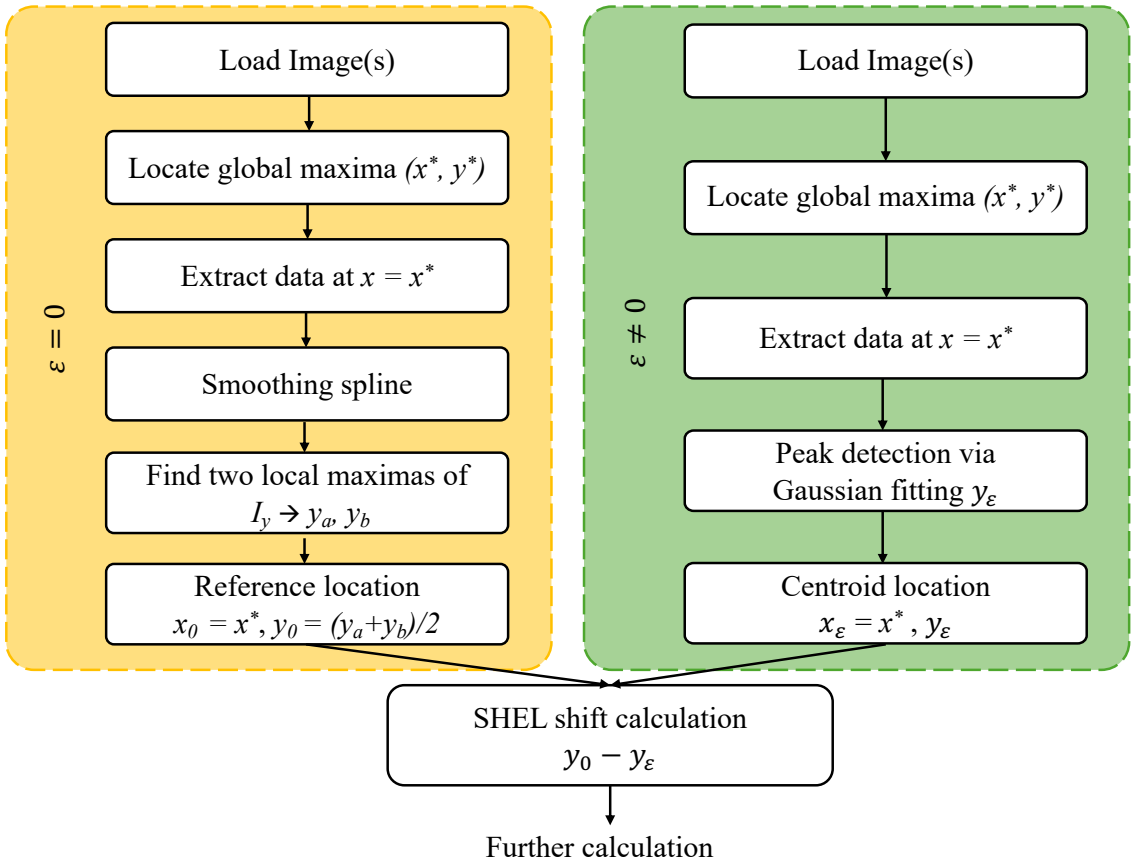


Fig. 2.9: Working flow of the image processing in detecting the beam shift, the yellow block corresponds to $\varepsilon = 0$ and the green block corresponds to $\varepsilon \neq 0$.

$$\delta_{A_w}^{H\pm}(\rho) = \mp\frac{(1+\rho^{-1})f_2 D_{out}^2}{8f_1^2 \tan\varepsilon \tan\theta_i} \tag{2.46}$$

$$\delta_{A_w}^{V\pm}(\rho) = \mp\frac{(1+\rho)f_2 D_{out}^2}{8f_1^2 \tan\varepsilon \tan\theta_i} \tag{2.47}$$

while the SHEL ellipsometry model based on the modified weak measurement can be derived from (2.26) and (2.27) by expressing it in tangent form through trigonometric identities into

$$\delta_{A_{mod}}^{H\pm}(\rho) = \mp\frac{2f_2(1+\rho^{-1})\tan\varepsilon \tan\theta_i D_{out}^2}{(1+\rho^{-1})^2 D_{out}^2 + 16f_1^2 \tan^2\varepsilon \tan^2\theta_i} \tag{2.48}$$

$$\delta_{A_{mod}}^{V\pm}(\rho) = \mp\frac{2f_2(1+\rho)\tan\varepsilon \tan\theta_i D_{out}^2}{(1+\rho)^2 D_{out}^2 + 16f_1^2 \tan^2\varepsilon \tan^2\theta_i} \tag{2.49}$$

Now that the SHEL ellipsometry model from (2.46) to (2.49) has been established as a function of ρ, it gives an intuitive understanding that this model can easily be used to measure physical parameters embedded in ρ by measuring amplified beam shift and using an appropriate interface model. Additionally, as the model is expressed in terms of hardware parameters f_1, f_2, and D_{out}, any change in experiment setup can easily be adjusted.

The complete measurement framework of Spin Hall Effect of Light (SHEL) ellipsometry is illustrated in Fig. 2.10. This flowchart summarizes the theoretical considerations discussed in this chapter and the experimental steps required to implement the technique. It ensures each stage is systematically carried out to guarantee repeatability of the measurement.

The process begins with the adjustment of the incident angle θ_i to the desired observation angle. As SHEL is an incident angle-dependent phenomenon, it is crucial to choose the appropriate incident angle, especially considering the incident polarization direction (e.g, horizontally polarized incidence). The incident angle adjustment is commonly realized by adjusting the alignment of the sample and reflection arm relative to the incident arm.

Once the sample is aligned correctly, a reference point for the shift detection is established by setting P_2 to a cross-polarized state relative to P_1 ($\varepsilon = 0$). Under this condition, two orthogonally polarized components of the reflected SHEL beam overlap symmetrically, producing a weak intensity two-lobed distribution at the detection plane. In this step, a sample tilting adjustment is necessary until the balance intensity is achieved. An additional measure is taken in the definition of the reference point by recording several frames of $\varepsilon \approx 0$ in the distorted state within a small range of $\pm\varepsilon$, then averaging the detected reference points. This step functions as a calibration point, ensuring beam displacements are detected relative to a well-defined reference.

The measurement stage proceeds by rotating P_2 to a non-zero ε value. This introduces an intentional imbalance between the polarization components, manifested as a spatial displacement of the beam in the y-direction. Images of the beam shifts are recorded using a CCD/CMOS detector. The recorded images are processed to calculate the SHEL shifts by comparing the centroid y position to the reference point and calculating its distance. These shifts encode information about the interaction of the light with the sample; thus, through appropriate modeling, they can be related to physical parameters such as refractive index, thin film thickness, and surface roughness.

In summary, the SHEL ellipsometry framework consists of several steps, including experiment and data analysis based on theoretical modeling. The integration of spin–orbit interaction and the ellipsometry framework translates theoretical advances into a practical metrology instrument, enabling characterization of optical and structural properties with nanoscale sensitivity.

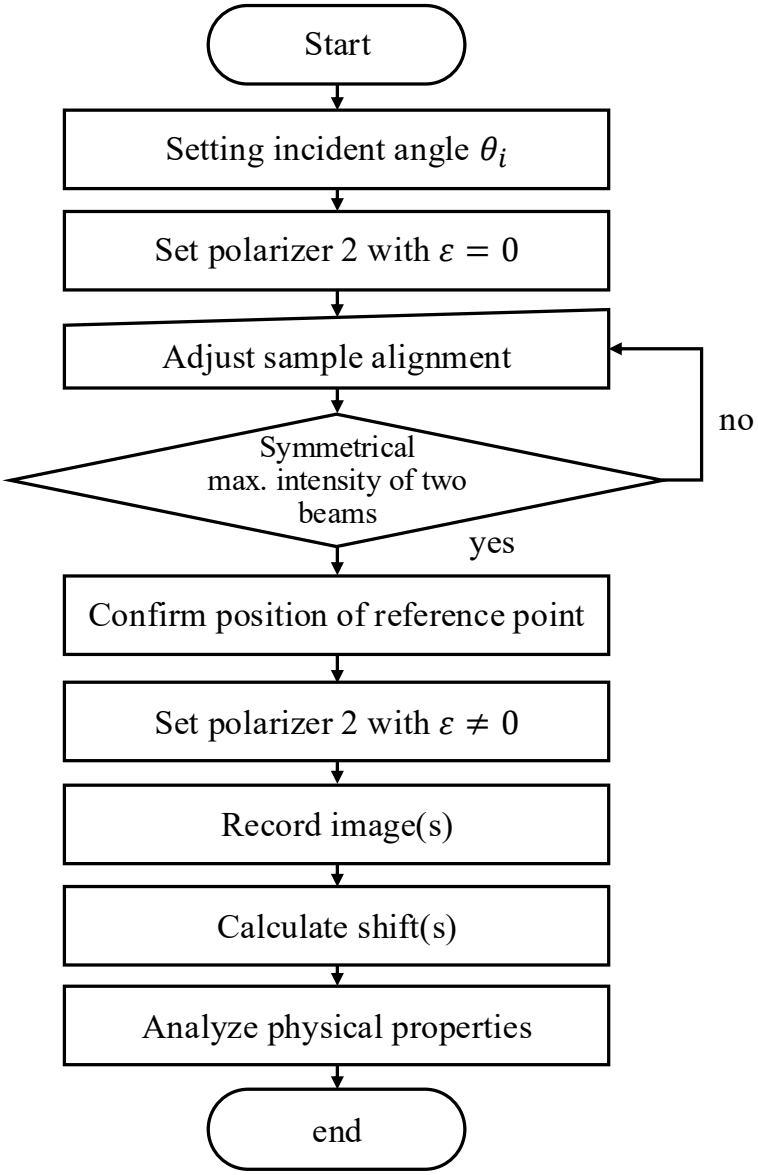


Fig. 2.10: Flowchart of measurement procedure using SHEL ellipsometry

Chapter 3

Proof-of-Concept of the Spin Hall Effect of Light Ellipsometry

3.1 Introduction

In this research, measurements of physical properties are performed through the observation of subwavelength beam shifts resulting from the varying properties at an optical interface. These shifts arise from variations in material properties and are detected using the weak measurement technique introduced in Chapter 2. Weak measurement amplifies the small beam shift by exploiting a predefined initial and final polarization state, typically realized with a pair of polarizers. When the polarizers are set nearly orthogonal, the subwavelength shift is amplified, making the Spin Hall Effect of Light (SHEL) more readily observable.

The oblique-incidence geometry and the use of a polarizer pair resemble the ellipsometry framework, in which optical properties are inferred from polarization-dependent interactions. However, unlike conventional ellipsometry, which relies on rotating elements such as polarizers or retarders depending on the configuration, SHEL ellipsometry requires only static polarizers. The absence of moving parts enhances stability and makes the method suitable for long-term measurements.

SHEL ellipsometry has been applied to diverse precision measurements, including refractive index, nano-film thickness, optical conductivity, and even temperature. Its versatility arises from the ability to model the optical interface according to the property of interest. In this chapter, we extend the method to demonstrate SHEL ellipsometry as a novel instrument for surface roughness characterization. As a preparatory step and proof of concept, the refractive index and thin film thickness are first measured to verify the accuracy and reliability of the framework.

This chapter is organized as follows. Section 3.2 elaborates on the experimental setup of SHEL ellipsometry, followed by Section 3.3, which explains the measurement result and the discussion of refractive index, thin film thickness, and surface roughness measurement. Finally, the chapter findings are summarized in 3.4.

3.2 Experimental Setup

Figure 3.1 shows the experimental setup of SHEL ellipsometry that can be divided into three parts: the incident arm, the detection arm, and the sample stage. The incident arm is fixed all the time and consists of a Laser He-Ne (λ=633 nm), focusing lens L1, and a Glan-Thompson polarizer to pre-define the polarization state of the incident light. Commonly, other works on SHEL observation use a half-wave plate to adjust the beam direction to modulate the intensity [113, 137, 140]. However, in this research, we don't use the half-wave plate to avoid the temperature-dependent error from the phase retarder. The sample stage consists of a double-angle rotation mount, an xy translation stage, and a sample holder. The double-angle rotation mount sets the incident angle by rotating both the sample stage and the detection arm, as shown in Fig. 3.2. Lastly, the detection arm consists of a sheet polarizer to define the reflected polarization state, collimating lens L2, and a CCD camera to record the shifted beam.

The light source in this experiment is a Helium-Neon Laser with $\lambda = 632.8nm$ manufactured by Melles Griot with manufacturing number 05-LHP-151 with linear polarization. The helium-neon laser is the most common and easiest to use light source, which is also widely used in the study of the Spin Hall Effect of Light. A detailed specification of the laser is presented in Table 3.1.

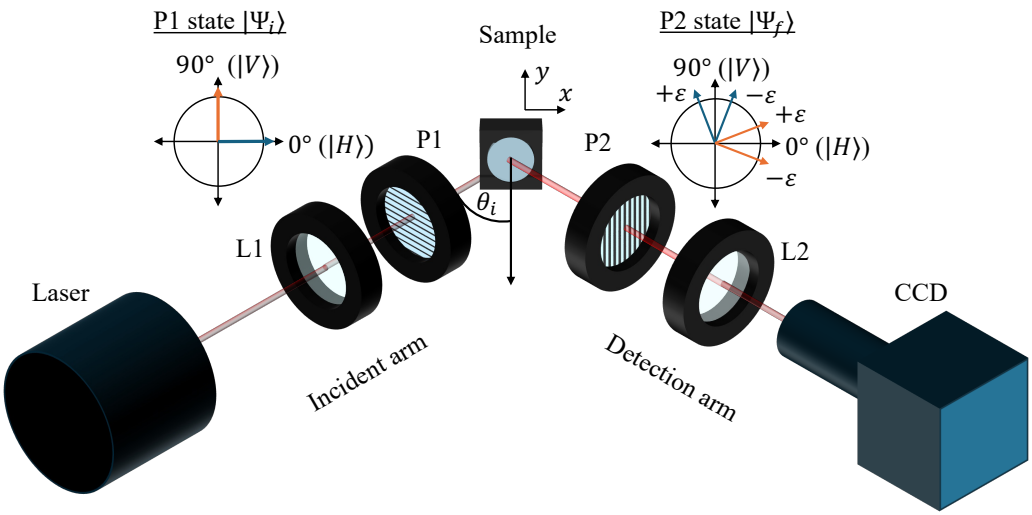


Fig. 3.1: Experimental setup of SHEL Ellipsometry

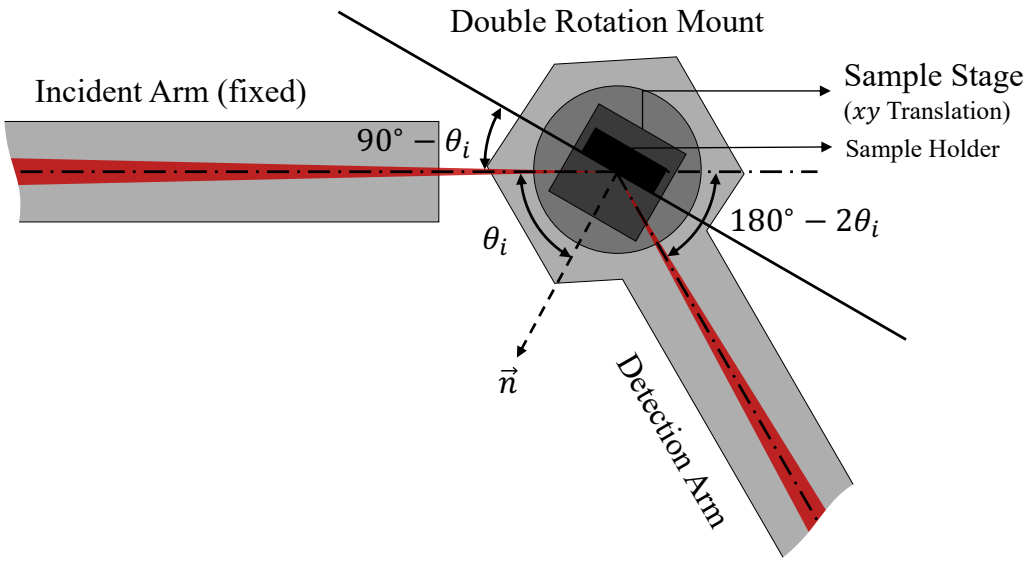


Fig. 3.2: Schematic of Incident Angle Control by Double Rotating Mount

Table 3.1: Specification of He-Ne Laser.

Manufacturing No	05-LHP-151
CW Output Power	5 mW
Beam Diameter	0.8 mm
Beam Divergence	0.1 mrad

The pair of polarizers realizes the weak measurement technique. Firstly, the pair is set perpendicular to each other. For example, when using a horizontal $|H\rangle$ incident, the GLP is set 0^o while the sheet polarizer is set 90^o. This cross-polarized setup is crucial for observing the symmetrical splitting of the SHEL, confirming the occurrence of the SHEL phenomenon, and for recording the image reference used to define the beam centroid's datum, as explained in Chapter 2.

The first polarizer in the incident arm (P1) defined the incident polarization, which is a Glan-Thompson Polarizer (GLP), an optical device made of two cemented calcite prisms that transmit linearly polarized light. The transmitted component is polarized along the crystal's extraordinary axis, while the orthogonal component undergoes total internal reflection and is removed. When addressing the $|H\rangle$, then the GLP is set 0° and transmits s-polarized light. The GLP used in this research is manufactured by Optosigma with manufacturing number GTPB-06-18SN.

On the other hand, the reflected light polarization state is defined by P2, which is a polarizer sheet made from dichroic dye film with aligned dye molecules absorbing light polarized along their axis, while transmitting the orthogonal polarization component. Since it is mounted in a rotating mount, the physical dimension of the hardware limits the polarizer in the detection arm. Thus, a polarizer sheet is utilized instead of another GLP. The polarizer sheet is Sigmakoki SPF-30C-32. It is mounted in a Sigmakoki SGSP-40YAM rotating mount that helps define the ε for the weak measurement setup. The rotating mount has a rotary resolution of 0.0025°/pulse and a positioning accuracy of 0.1°, making it useful in adjusting the ε. Table 3.2 shows the specification of the polizer sheet and the rotating mount.

The pair of lenses L1 and L2, where $f_1 < f_2$, creates a telescope system that amplifies the beam based on the fundamental Gaussian propagation behavior. In this setup, $f_1 = 100mm$ while the $f_2 = 175mm$. Since the lens pair added an amplification factor, naturally, the biggest possible amplification factor is

Table 3.2: Specification of Polarizer Sheet and Rotating Mount.

Polarizer Sheet	
Manufacturing No.	SPF-30C-32
Suitable Wavelength	400 - 700 nm
Coating	AR coating both sides
Rotating Mount	
Manufacturing No.	SGSP-40YAM
Resolution	0.0025°
Maximum Speed	$30°/s$
Position Accuracy	0.1°
Position Repeatability	0.02°

desired. Nevertheless, it is limited by the hardware dimensions. Besides giving the propagation factor, L1 also defines the beam size at the sample, while L2 collimates the reflected beam to the detector. Table 3.3 shows the specifications of L1 and L2.

Table 3.3: Specification of Lenses

	Lens 1	Lens 2
Focal Length	100 mm	175 mm
Type	N-BK7 Convex Lens	
Manufacturer	Thorlabs	
Manufacturing No	LA1050A	LA1399A

Beam observation and image recording are conducted using a CCD camera manufactured by The Imaging Source with manufacturing number DMK51BU02.WG. It comes without any protective glass to avoid any interference fringes or Newton's rings, which are usually formed in a detector with a cover glass. The CCD has a high sensitivity for low-intensity light, which is suitable for detecting weak signals of SHEL. The parameters, such as gain and exposure time, remain unchanged during measurements to ensure experiment consistency. Table 3.4 shows the detailed specification of the CCD.

Lastly, the picture of the complete experiment setup is shown in Fig. 3.3.

Table 3.4: Specification of CCD Camera

Resolution	1600×1200 (1.9MP)
Pixel Size	$4.4\mu m \times 4.4\mu m$
Frame Rate	12 fps
Shutter Speed	1/1000 s - 30 s
Sensitivity	0.05 lux

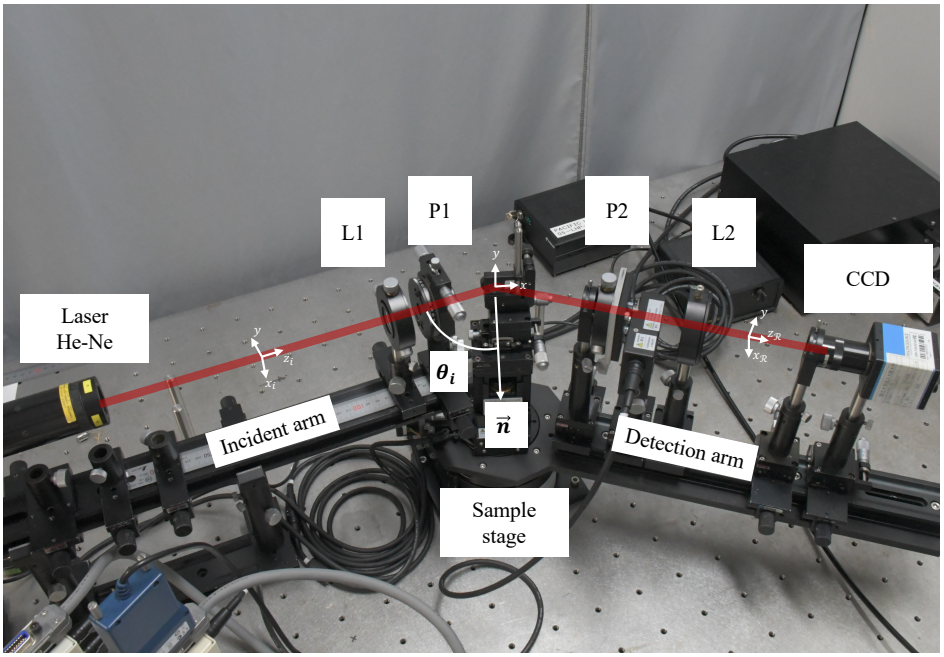


Fig. 3.3: Picture of the Complete Experiment Setup

3.3 Measurement Application

In this section, we show how SHEL ellipsometry is applied to measure various physical properties. Based on the complexity of the interface model and the mode of measurement, it will be divided into refractive index measurement by single spot measurement, film thickness measurement by line scanning measurement, and surface roughness measurement by scanning area measurement.

3.3.1 Refractive Index

Numerical Calculation

First, it begins with a numerical simulation to study the behavior of the SHEL shift upon varying refractive indices from the air-glass interface. For both $|H\rangle$ and $|V\rangle$, the SHEL shift is calculated for varying refractive indices from 1.30 to 1.50. Additionally, it is observed for incident angles from $40° - 70°$. Figure 3.4 shows the calculated SHEL shift to incident angle based on (2.9)-(2.10), (a) for $|H\rangle$ incident and (b) for $|V\rangle$ incident.

From Fig. 3.4, it can be seen that the range of shift under $|H\rangle$ incident is significantly larger than $|V\rangle$. Additionally, Fig. 3.4(a) shows interesting behavior where the shift is negatively symmetrical relative to a particular point. Another interesting thing to note is that the graph shifts along the incident angle with increasing refractive indices in Fig. 3.4(a). This point where the shift changes sign happens when the incident angle coincides with the Brewster's angle (θ_B) of the sample, where $\theta_B = tan^{-1} n_2/n_0$. It can also be seen that approaching the θ_B, the shift grew exponentially large, showing promising potential for measurement. Yet, with $|H\rangle$, SHEL observation cannot be performed at $\theta_i = \theta_B$. This anomaly near Brewster's angle happens due to the strong coupling phenomena from a weak measurement point of view. In contrast, with $|V\rangle$ there is no limitation regarding Brewster's Angle since r_p is available and the weak coupling is retained at all incident angles. However, since the range of shift in $|V\rangle$ is essentially small, it would be more challenging to detect an even lower rate of change of the physical properties. Both incident angles show how SHEL is sensitive to the refractive index change. Furthermore, the $|H\rangle$ sensitivity to the sample's Brewster's angle further indicates the potential of utilizing the measurement of SHEL shift in discriminating different refractive indices.

Affecting Parameters

For the proof-of-concept, a measurement experiment is conducted to retrieve the refractive index of known samples using SHEL ellipsometry, where the retrieved refractive index is introduced as pseudo-

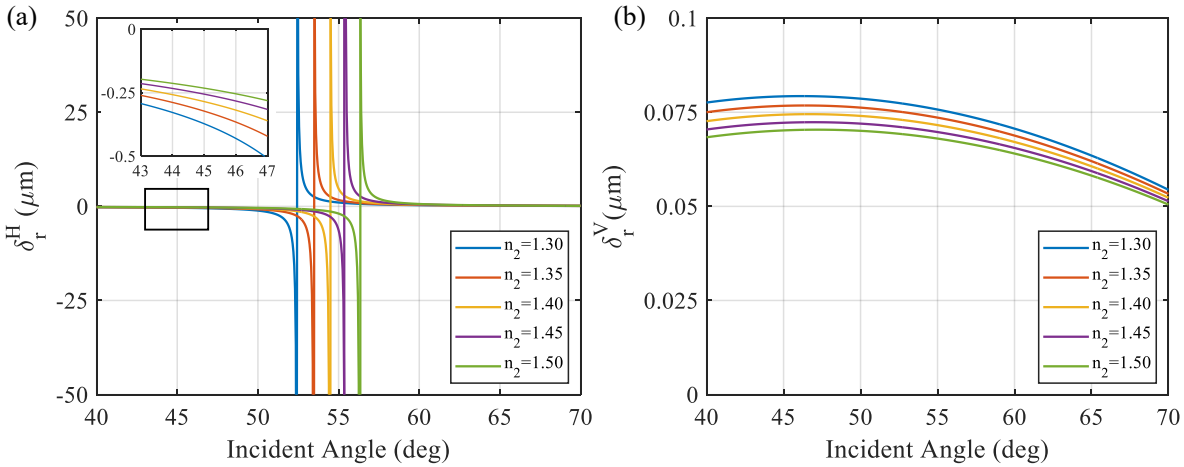


Fig. 3.4: Numerical calculation of SHEL shift upon varying refractive index (a) for $|H\rangle$ and (b) for $|V\rangle$

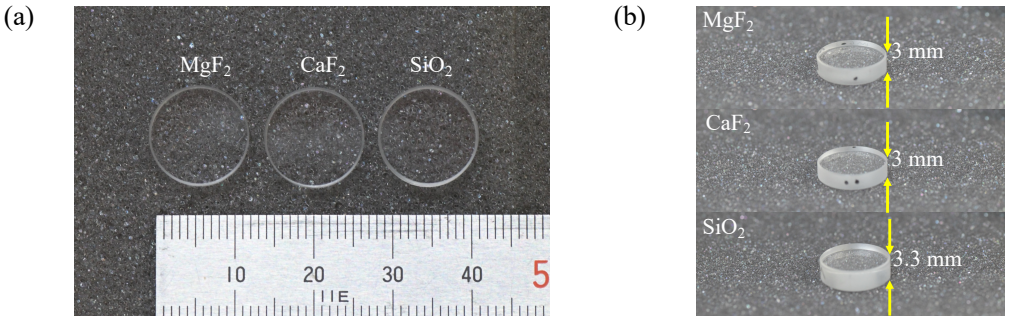


Fig. 3.5: Sample with known refractive index value, (a) top view, (b) side view

refractive index. For the refractive index experiment, three samples of known refractive index were used. These three samples are made of different materials: MgF_2, CaF_2, and SiO_2 as shown in 3.5. These samples are optical windows with a one-inch diameter, while MgF_2 and CaF_2 have a thickness of 3 mm; the SiO_2 sample is slightly thicker, with a thickness of 3.3 mm. Additionally, although intrinsically MgF_2 is anisotropic, for the refractive-index retrieval experiment, it is treated as an effective refractive index, neglecting its anisotropic behavior.

Firstly, an experiment is conducted to evaluate the weak measurement models and the incident polarization, and how well the measurements agree to the considered models. The experiment is conducted upon both incident polarizations along the incident angle range of $40° - 70°$. The first sample is an optical flat made from SiO_2 with $n = 1.456; \theta_B \approx 55.5°$. The ε use in $|H\rangle$ and $|V\rangle$ is different. For $|H\rangle$ the ε are $0.5°, 1.0°, 1.5°$, while for $|V\rangle$ the ε are $0.1°, 0.3°, 0.5°$. Figure 3.6 shows the measurement results, (a-c) are $|H\rangle$ with its respective ε from small to large, (d-f) are $|V\rangle$ also with its respective ε from small to large. The measurement result is represented by black circles, a solid red line representing the conventional weak measurement model calculated based on (2.46)-(2.47), and a blue solid line representing the modified weak measurement model calculated based on (2.48)-(2.49). It shows how the modified model compensated the area near Brewster's angle for $|H\rangle$. For the $|V\rangle$, we observe that with the increasing ε, both weak measurement models are getting closer and nearly overlapping in (g). From both $|H\rangle$ and $|V\rangle$, the measurement result agrees better with the modified weak measurement model. Thus, the modified weak measurement model is used in this research instead of the conventional weak measurement model for the data analysis.

Next is the evaluation of the measurement result. For $|H\rangle$ the negative symmetry at the $\theta_i = \theta_B$ are apparent for all three values of ε. It is also observed that with increasing ε, the shift range at the incident far from θ_B is smaller while the graph is getting sharper. The shift slope in the vicinity of θ_B gets sharper with the selection of higher ε. The graph also shows that near the Brewster angle, the measurement result does not agree with either model of weak measurement. However, with the increased value of ε, the area of disagreement between the measurement and the modified weak measurement model is narrowing. In

$|V\rangle$, the measurement result is also closer in accuracy to the model in higher ε. This measurement shows how the combination of θ_i and ε is pivotal in SHEL ellipsometry.

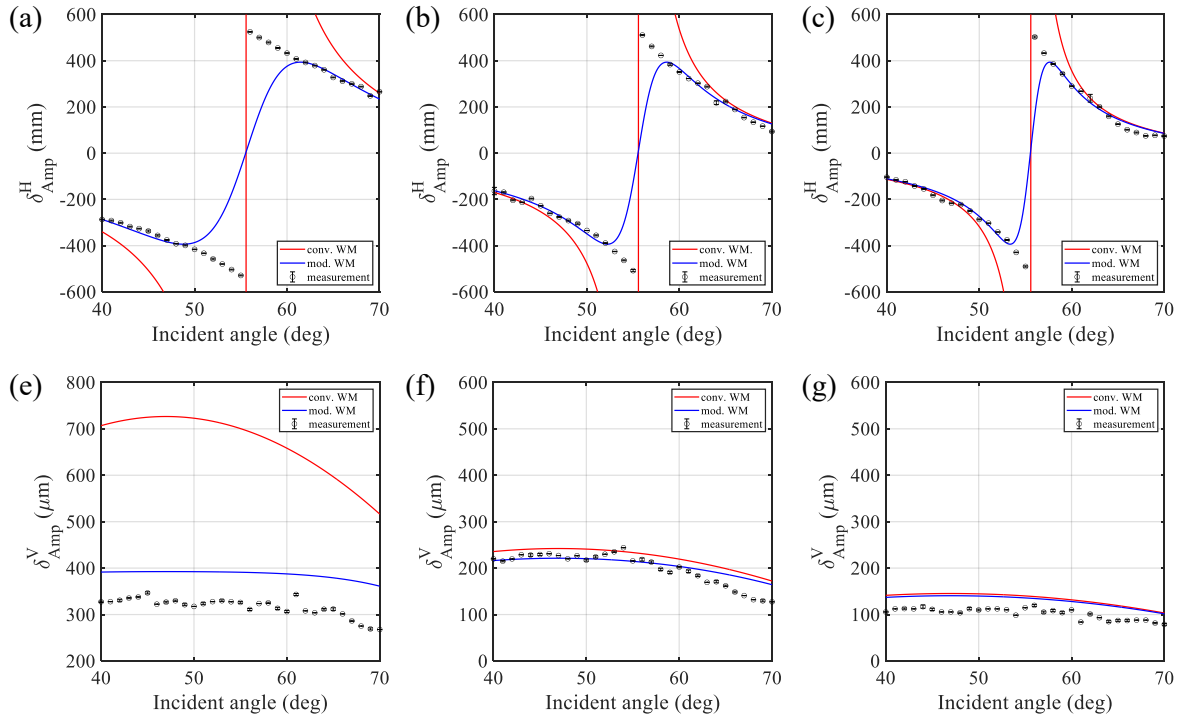


Fig. 3.6: SHEL shift measurement on varying incident angle from 40◦ to 70◦ with $|H\rangle$ incident (a) $\varepsilon = 0.5^o$; (b) $\varepsilon = 1.0^o$; (c) $\varepsilon = 1.5^o$; and with $|V\rangle$ incident (d) $\varepsilon = 0.1^o$; (e) $\varepsilon = 0.3^o$; (f) $\varepsilon = 0.5^o$

Comparison Measurement

Previously, it has been shown how the measurement agrees with the SHEL ellipsometry model. This part uses comparison measurement to demonstrate the actual application of SHEL ellipsometry. Three optical windows made from different materials with known refractive indices from their specifications were observed: MgF_2 (n = 1.37), CaF_2 (n = 1.43), and SiO_2 (n = 1.45), shown in 3.5. The windows' diameters are 1 inch, with thicknesses of 3 mm and 3.3 mm. Static measurements were carried out with 30 data points for each parameter. The incident angle for all the measurements was kept at $\theta_i = 50°$. For the $|H\rangle$ incident, the post-selected azimuth angles were $0.5°, 1.0°, 1.5°$, while for the $|V\rangle$ incident, the

post-selected angle was $0.1°, 0.3°, 0.5°$.

Figure 3.7 shows the comparison between the shift measurement of MgF_2 and CaF_2 for $|H\rangle$ with $\varepsilon = 1.5°$ and $|V\rangle$ with $\varepsilon = 0.5°$. Figure 3.7 shows how the measurement can distinguish the two materials from both the shift amount and the respective Brewster's angle, where the shift changes sign. In Fig. 3.7 (b), the shift value relatively shows a consistent feature where the shift of CaF_2 is smaller than MgF_2, even though the measurement results stray from the theoretical values.

Finally, the pseudo-refractive index is retrieved from the measured shift by solving the SHEL ellipsometry model with the air-glass interface model. Figure 3.8 shows the accuracy graph comparing the measured refractive index to the actual refractive index for both $|H\rangle$ and $|V\rangle$, respectively. The results from the $|H\rangle$ incident measurements exhibit greater accuracy against the known values compared to the $|V\rangle$ incident. Furthermore, the trend in the $|H\rangle$ measurements aligns well with the actual refractive index value. Conversely, the $|V\rangle$ incident measurements at $\varepsilon = 0.3°$ and $\varepsilon = 0.5°$ present a misleading trend and do not yield the correct refractive index value. This measurement is more prone to errors due to the minimal shift. Consequently, the shift variations stemming from different medium properties are even less pronounced, making them harder to detect. While Brewster's angle of the sample does not constrain the $|V\rangle$ incident, the narrow shift range in this setup makes it a less preferable choice. This experiment highlights the capability of SHEL ellipsometry in accurately determining the physical properties of samples, as demonstrated by comparing the pseudo-refractive index with the known refractive index of the samples.

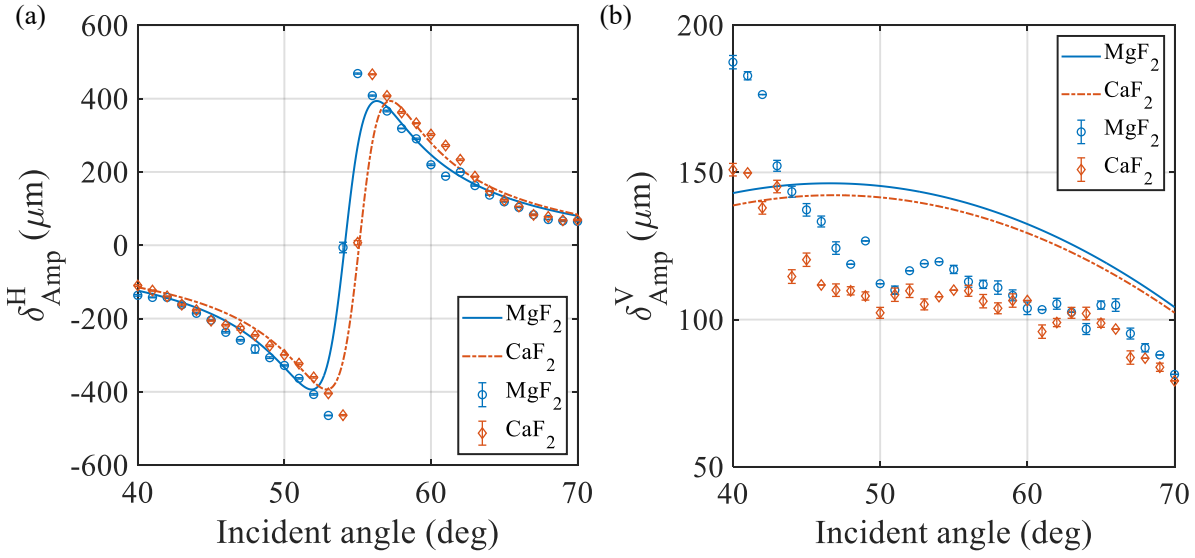


Fig. 3.7: Comparison of samples with different refractive index: MgF_2 ($n = 1.37; \theta_B \approx 54°$) and CaF_2 ($n = 1.43; \theta_B \approx 55°$), (a) using $|H\rangle$ with $\varepsilon = 1.5°$ and (b) using $|V\rangle$ with $\varepsilon = 0.5°$

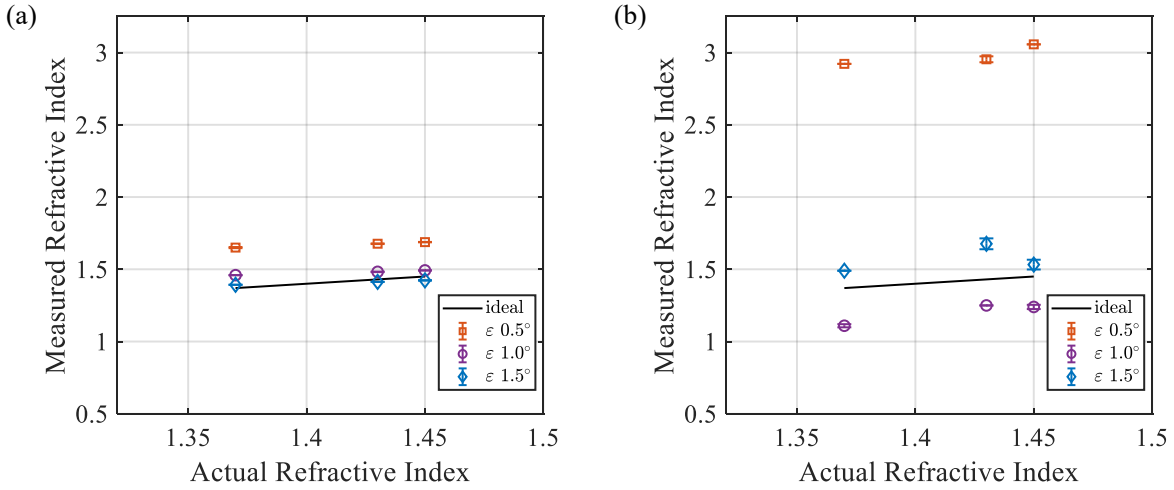


Fig. 3.8: Measurement result of refractive indices (a) using $|H\rangle$ and (b) using $|V\rangle$

3.3.2 Film Thickness

Numerical Calculation

The next physical property to be observed is the influence of film thickness. For this measurement, two interface layers result in multiple reflections. For film thickness measurement, both the refractive index of the bulk substrates and the film layer are known. Thus, film thickness d can be derived from solving the SHEL ellipsometry according to the single-layer model. Numerical calculation is conducted for a scenario of a gold (Au) nanolayer deposited on top of a BK7 substrate. SHEL shift is calculated both for $|H\rangle$ incident and $|V\rangle$ incident as depicted in Fig. 3.9 (a) and (b) respectively. The Au ($n = 0.1433 + 3.6080i$) nano layer is calculated from 0.5 nm to 10 nm and is also compared to the air-glass model-BK7 ($n = 1.515$) model without Au nano layer deposition ($d = 0$ nm). Both incident angle shows similar behavior as in the air-glass model, with $|H\rangle$ having a significantly larger SHEL shift range compared to $|V\rangle$. In addition, the shift range gets smaller as the layer thickness increases. For $|V\rangle$, it can be observed that the maximum shift is moving towards a larger incident angle with increased thickness. Nevertheless, the calculation shows the potential of SHEL ellipsometry in measuring nanofilm layer thickness with sub-nm resolution.

Sample Preparation

For the film thickness experiment, a simple sample was prepared. Using a sputtering machine, a gold nanolayer was deposited on top of bulk substrates. Two kinds of substrates were used, BK7 and SiO_2, with specifications in the Table. 3.5. The Au layer is deposited in four different deposition times, 60 s, 120 s, 180 s, and 240 s, as shown in Fig. 3.10 (a). The bulk substrate was divided into five areas, including the area that was not exposed to the sputtering. Figure 3.10 (b) shows the final sample Au layers on top of the SiO_2 substrate. There are different layer thicknesses observed from the color gradation, where longer deposition times appear darker. Under constant power, layer thickness has a linear relationship to the deposition time, with a short deposition time may result in a discontinuous

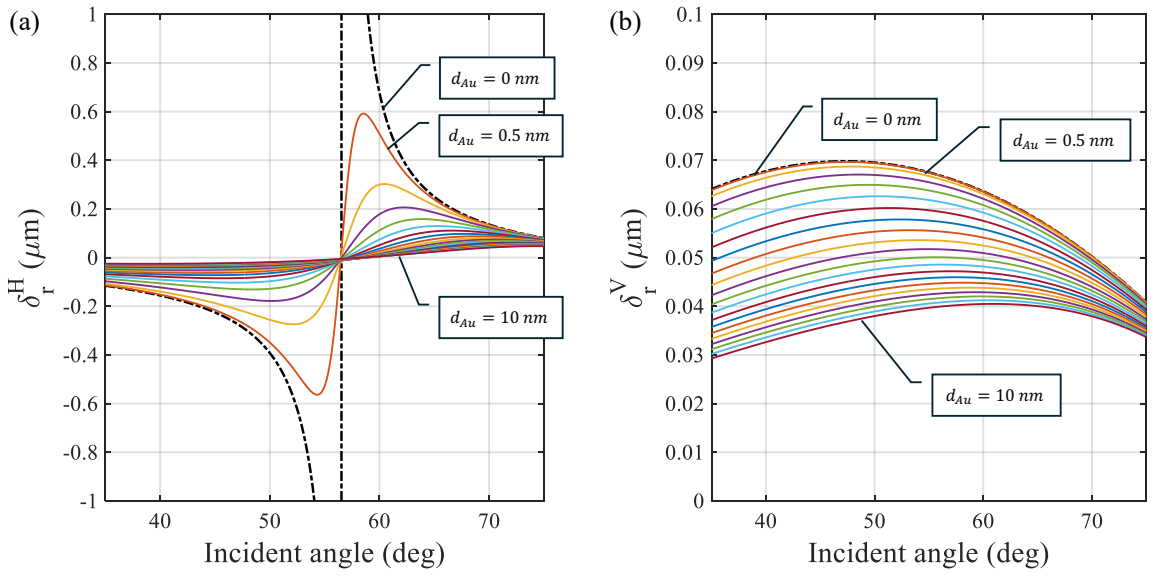


Fig. 3.9: Numerical calculation of SHEL shift to incident angle of varying Au film thickness from 0.5 nm to 10 nm on a BK7 substrate (a) using $|H\rangle$ and (b) using $|V\rangle$

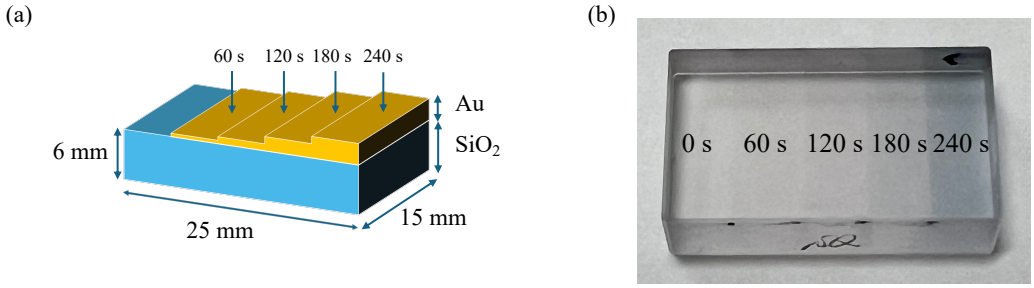


Fig. 3.10: Sample preparation of gold film thickness on BK7 and SiO_2 (a) design of film layer and deposition time (b) sample of gold film layer on SiO_2 substrate

island layer instead of a continuous flat layer [153, 154]. SHEL ellipsometry is expected to distinguish between different deposition times from the measured beam shifts, thereby reflecting the differences in layer thickness information.

Measurement Result

The measurement use $|H\rangle$ incident conducted at $\theta_i = 51^\circ$ and $\varepsilon = 1.5^\circ$. As the sample is prepared with a varying layer thickness similar to a stair, line scanning measurement with an overlap beam is carried out to see whether the SHEL ellipsometry can retrieve the stair-like structure.

Figure 3.11 shows the measured amplified shift from (a) the varying gold film layer on SiO_2 and (b) the varying gold film layer on BK7 substrates. From both samples, the expected stair-like structures are evident from the measured shift. Additionally, with the increased deposition time, the measured shift grows smaller, proving the inverse proportionality relation between SHEL shift and film thickness, agreeing with the theoretical prediction. Most importantly, the nanoscale thickness variation of the gold layer, despite not being precisely controlled, is detectable by SHEL ellipsometry. The reconstructed stair-like structure also demonstrates SHEL ellipsometry potential, offering the capability for surface morphology characterization.

Table 3.5: Specification of substrates used as the base of gold film growth

Material	SiO_2	BK7
Manufacturer	Sigmakoki	
Prod. Code	OFSQ-1525R06-20	OFB-1525R05-20
Dimension (mm)	15×25	
Thickness (mm)	6	5
Flatness	$\lambda/20$	$\lambda/20$
Surface Quality (Scratch-Dig)	20-10	10-5
Coating	uncoated	

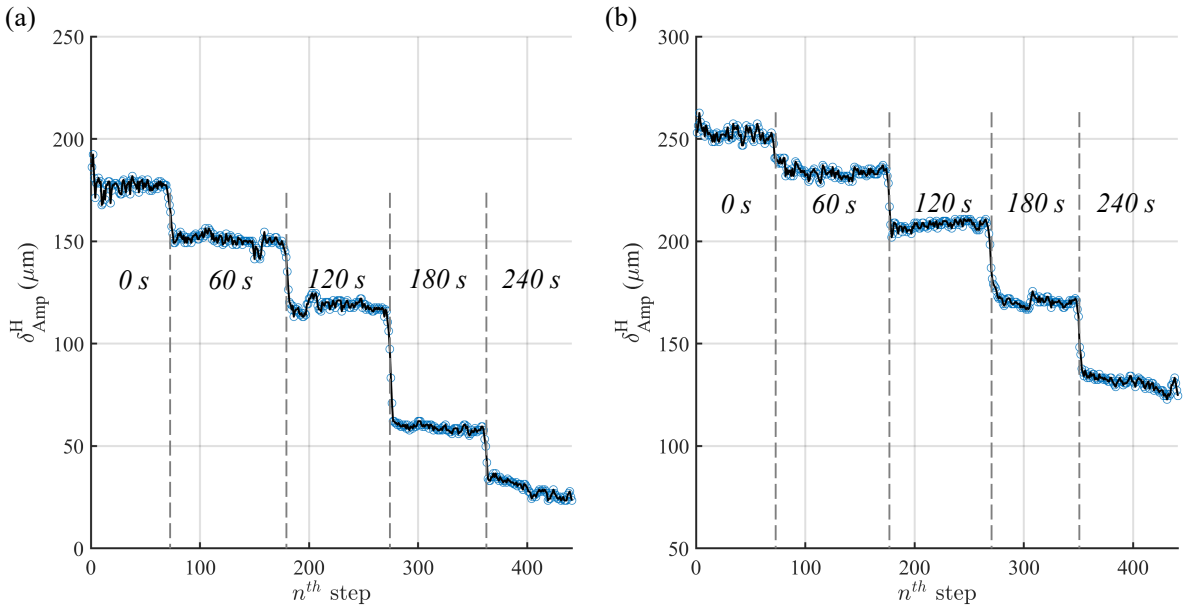


Fig. 3.11: Measured SHEL shift using $|H\rangle$ of (a) gold film layer on SiO_2 and (b) gold film layer on BK7

3.3.3 Surface Roughness

Numerical Calculation

Figure 3.12 depicts the original SHEL shift affected by the effective medium approximation of the roughness layer. The analysis covers a range of roughness equivalent thicknesses from 2 nm to 10 nm, and compares with the Fresnel model that assumes 0 nm roughness at the air-glass boundary. In Fig. 3.12 (a), the influence of d_{EMA} on the SHEL shift using horizontal polarization incident is shown, revealing that the SHEL shift varies with modifications with varying d_{EMA}. Figure. 3.12 (b) shows the calculation of the SHEL shift under vertical polarization incidence. In this model, surface roughness affects SHEL shift similarly to interference in a single-layer film. As can be seen, the surface roughness affects the SHEL shift more significantly in $|H\rangle$ incident compared to $|V\rangle$. Additionally, the influence of surface roughness on the SHEL shift value is not as rapid as the film thickness influence of a complex refractive index film. This happens due to the effective refractive index of the roughness layer being a real number from the calculation of Bruggeman EMA. Even so, this numerical calculation shows that nanoscale effective roughness inherently influences the SHEL shift.

Scanning Measurement

A key objective of this work is to reconstruct a two-dimensional mapping of the observed surface via raster scanning. As illustrated in Fig. 3.1, the sample stage is mounted on a motorized xystage, and data is collected by recording the beam shift at each point as the stage moves. To achieve good resolution, the scanning steps overlap and are smaller than the focused beam diameter as shown in 3.13. The beam waist in this setup is 101 μm, with a scanning step of 50 μm applied in both the x and y directions for all measurements. Once data are gathered from all points along the scanning line, each point is processed using the SHEL ellipsometry model to extract the target parameters, and the 2D mapping is then reconstructed. Thus, the d_{EMA} value retrieved at each point represents the averaged effective roughness of the area illuminated by the beam cross-section.

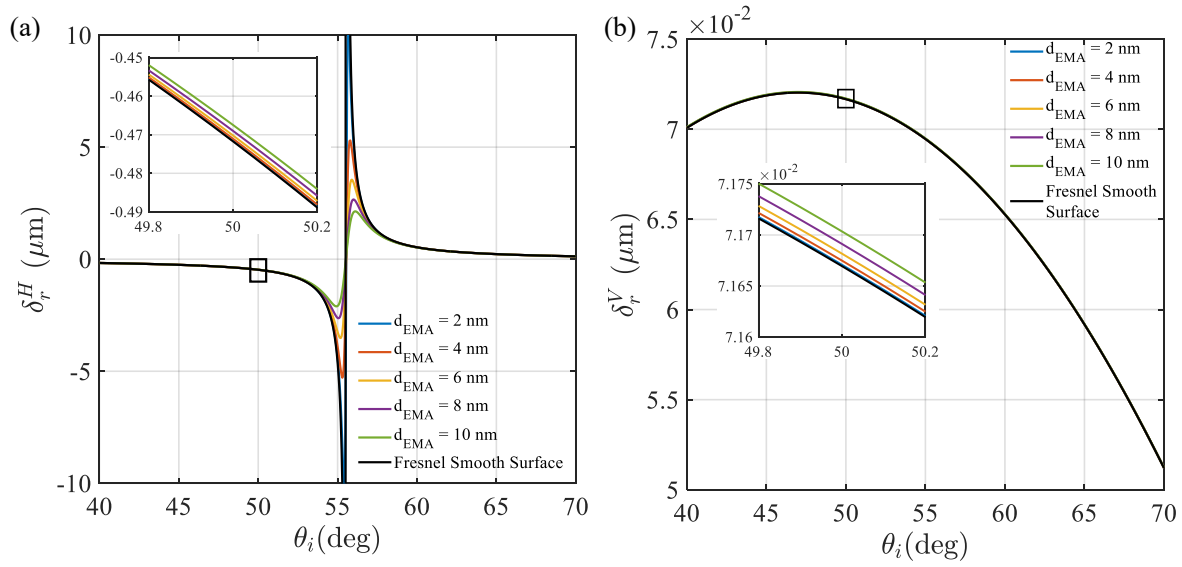


Fig. 3.12: Numerical calculation of the influence of surface roughness on SHEL shift (a) $|H\rangle$ incident, (b) $|V\rangle$ incident

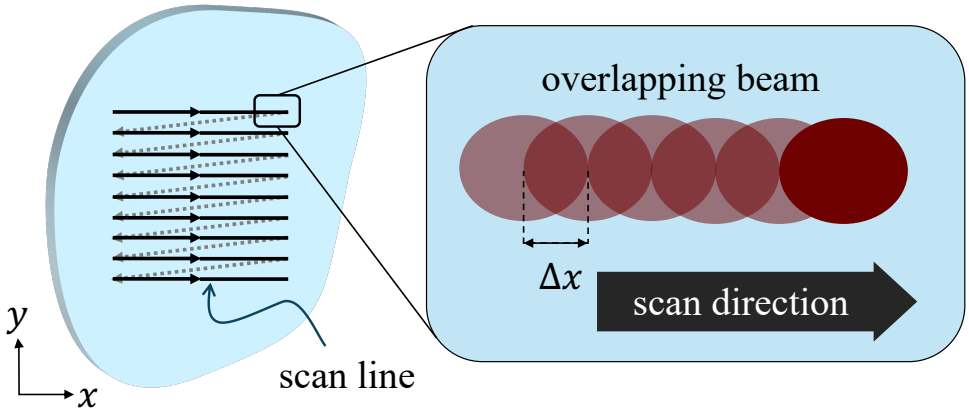


Fig. 3.13: Schematic of raster scanning and overlapping beam scanning process

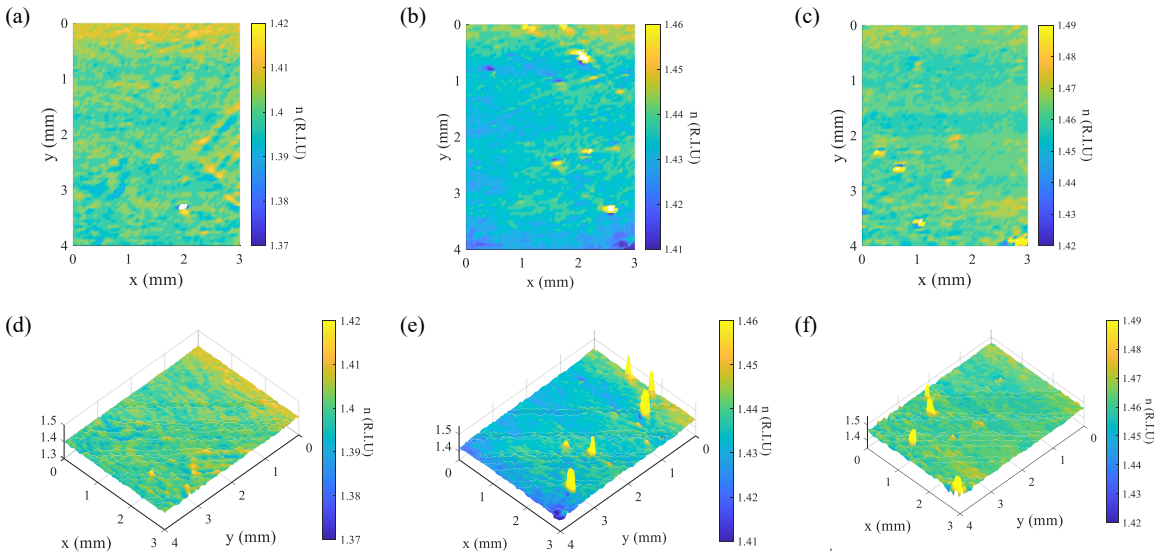


Fig. 3.14: Scanning result of three different optical flats for MgF_2, CaF_2, SiO_2 in (a-c) 2D reconstruction and (d-f) 3D reconstruction

Figure 3.14 (a)-(c) presents the scanning results of the same samples measured in 3.3.1, which include MgF_2, CaF_2, and SiO_2. The scanning was conducted with $\theta_i = 50°$ and $\varepsilon = 1.5°$. It is important to note that both θ_i and ε remain unaltered during the scanning process. The scanning area for each sample measures 3 mm x 4 mm. The reconstruction displays the retrieved pseudo-refractive index of the samples, as indicated by the color bar. The distribution of the retrieved pseudo-refractive index from the surface suggests the presence of a physical quantity that causes its value to vary. From the plot in Fig. 3.14, the measurements reveal intriguing scratch-like features on the object that may originate from the actual condition of the sample. It is important to note that any feature larger than the nano-scale, whether originating from the sample or debris on the sample, could create significant scattering that cannot be detected by SHEL ellipsometry. This typically appears as an outlier value, for instance, represented as a yellow saturated value in Fig. 3.14. In addition to examining the two-dimensional distribution, the average pseudo-refractive index consistently reflects accuracy in relation

to the actual refractive index values: MgF_2 (n = 1.37), CaF_2 (n = 1.43), and SiO_2 (n = 1.45). SHEL ellipsometry measurements propose a novel approach to evaluating surface roughness in terms of the pseudo-refractive index. Since the mean pseudo-refractive index can indicate the general refractive index value, the variance of the pseudo-refractive index may represent the degree of roughness. Consequently, it can be advantageous for comparative roughness measurements of samples made from the same material with varying roughness information.

The second scanning experiment utilized a different sample: a high-precision polished fused silica optical flat (n= 1.45) with a 30 mm diameter and 10 mm thickness (Sigmakoki HMPQP-30C10-20), illustrated in Fig. 3.17 (a). As per its specifications, this optical flat features a 95% clear aperture, indicating that the remaining 5% may have imperfections or may not meet the required surface quality for its intended application. The full-field wavefront imaging of the sample using Zygo WLI at a wavelength of 632.8 nm, as provided by the manufacturers, is shown in Fig. 3.15. This figure illustrates that the outer part has a different surface height compared to most of the surface, with a surface rms of 0.008 waves. For additional supporting data, a measurement at three different locations of the samples, at the center, outer part, and the roll-over part, was conducted using Mitutoyo Hyper QV WLI 606, shown in Fig. 3.16 with the resulting Sa of 3.66 nm, 13.99 nm, and 3.30 μm. From the two WLI imaging results, various levels of roughness can be anticipated on the outer section; additionally, an edge indentation, typical for optical elements, is present at the outer extremity.

A comparison between the center and outer areas was conducted using SHEL ellipsometry with the same experimental parameters as before, but the scanning area measured 2 mm x 3 mm. Measurement results for the center and edge areas are displayed in Fig. 3.17 (b) and (c), respectively. It is evident that the center region exhibits a consistent shift value that suggests a uniform degree of roughness. In contrast, the edge area experiences greater varying shifts: the section in the top right corner is closer to the center of the sample, while moving further towards the edge reveals a significantly amplified shift. The yellow strip in the bottom left corner of the reconstruction indicates an extreme value associated with the rollover indentation area. This indentation is notably rough compared to the overall surface of the

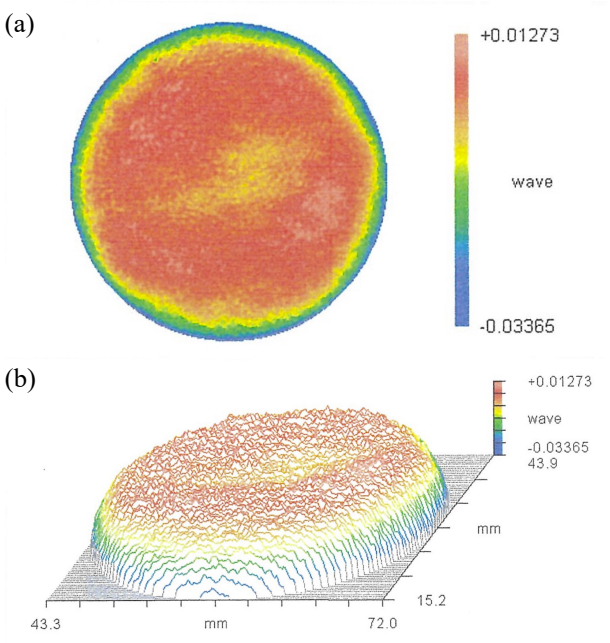


Fig. 3.15: Full-field WLI scanning from product manual of SiO_2 optical flat (a) 2D reconstruction, (b) 3D reconstruction

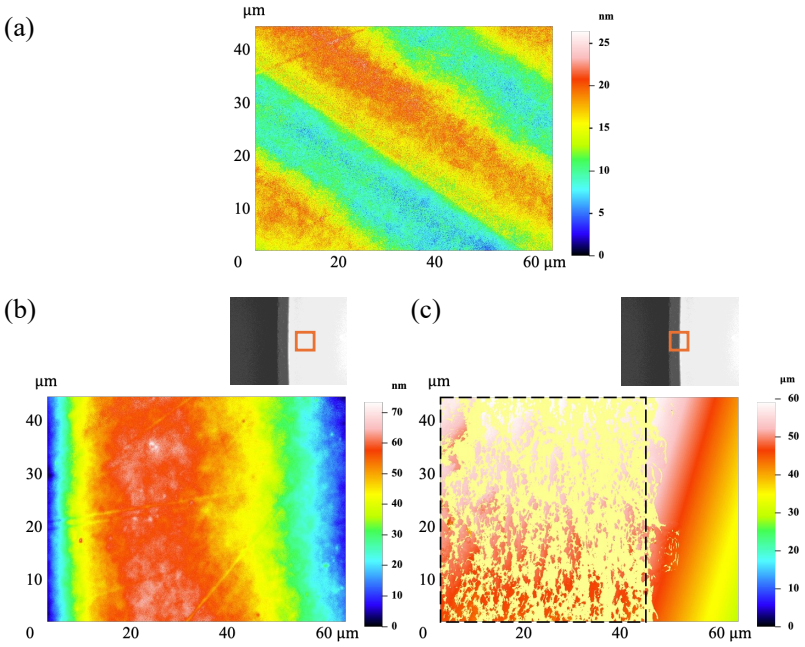


Fig. 3.16: WLI scanning of SiO_2 (a) central area, (b) outer diameter area, and (c) roll-over area

optical flats, resulting in increased scattering. Next, scanning was performed across the four quadrants of the optical flat, covering an area of 3 mm x 5 mm, as represented by the yellow squares in Fig. 3.18 (a). Figure 3.18 (b)-(d) illustrates the reconstructions of these four quadrants. The reconstructions display similar general features, revealing varied surface roughness, with the center exhibiting relatively smooth characteristics against the rough area at the bottom, which features a clear transition marked by the black dashed line. In the rough area, the measured refractive index demonstrates greater variability compared to the actual refractive index values of the samples. Moreover, lower refractive index values are observed in this rough region, potentially due to the slight slope profile of the outer ring compared to most areas, resulting in incident angle errors. The experiments depicted in Fig. 3.14 to Fig. 3.18 suggest that SHEL ellipsometry scanning can accurately capture the surface conditions of the sample. In addition, the raster scanning conducted in these results was conducted over a large area in milimeter scale. Since the scanning step is only 50 μm, the scanning process can take hours to finish. Thus, the results shown in Fig. 3.18 can also be taken as proof of a good stability of SHEL ellipsometry even though, in this stage, the environmental parameters such as temperature and humidity did not vary extremely during measurement.

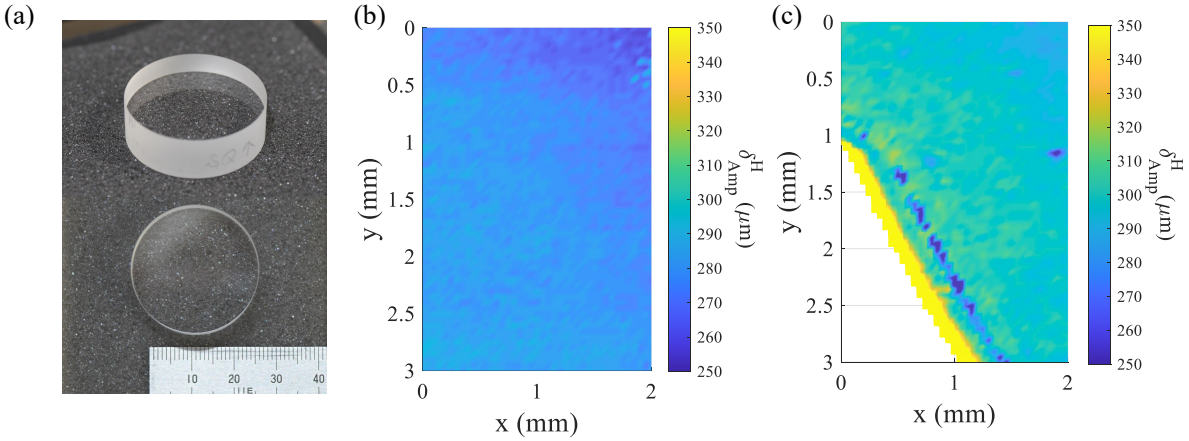


Fig. 3.17: SHEL scanning on (a) SiO_2 optical flat, (b) center area, and (c) edge area

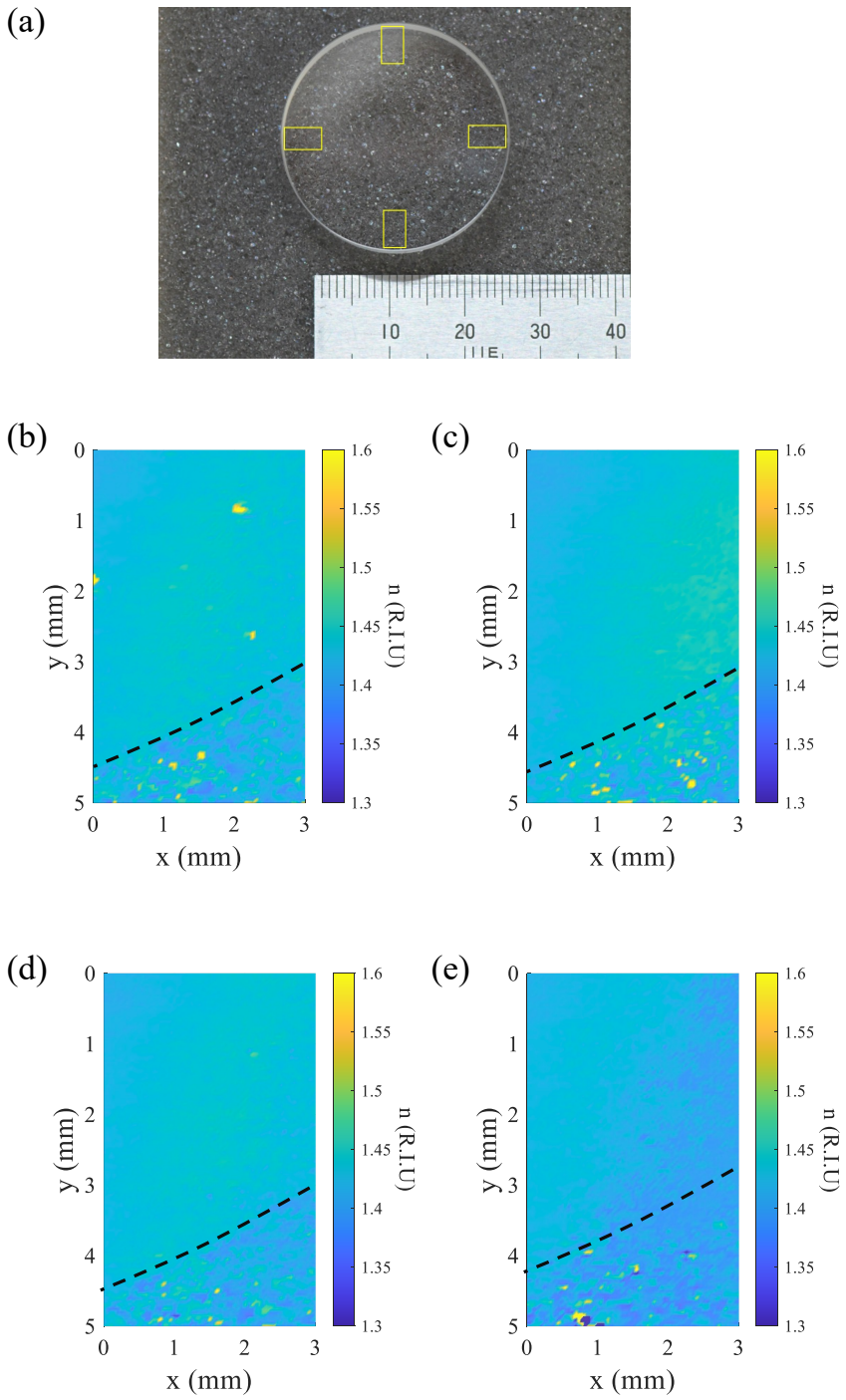


Fig. 3.18: SHEL scanning of SiO_2 (a) scanning area (b-e) result of the four area scanning

Comparison Measurement

The preceding measurement can be considered relatively qualitative due to the absence of precise data regarding the actual values of the varying levels of surface roughness. In the current experiment, we undertook a comparative analysis of two distinct surface roughness levels of the identical material. The specimen utilized is a single-surface optical flat made of SiO_2 (n = 1.45, Edmund #43-400-000), which indicates that the front and rear surfaces of the optical flat differ: the front surface is precisely polished, whereas the rear surface is not. To validate this information, a measurement using an Atomic Force Microscope (AFM) was executed across a scanning area of 20 x 20 μm with 256 scan lines. As shown in Fig. 3.19(a) and Fig. 3.19(b), the polished and unpolished surfaces manifest distinct roughness levels. Quantitatively, the polished segment displays a Sa value of 0.605 nm, while the unpolished segment reveals a higher Sa value of 1.25 nm. The AFM measurement verified the differing roughness levels of the front and rear surfaces.

SHEL ellipsometry scanning was performed on both sides of the optical flat, covering an area of 3 mm x 4 mm. In ellipsometry studies, the parameter d_{EMA} is recognized to correlate with the RMS roughness measured by a profilometer for that same area [76, 150]. The reconstructions from SHEL ellipsometry are presented in Fig. 3.19 (c) and Fig. 3.19(d) for the polished and unpolished surfaces, respectively. The calculated areal surface roughness values in terms of d_{EMA} are 48.65 ± 6.73 nm for the polished surface and 55.89 ± 11.76 nm for the unpolished surface. These results indicate how varying polishing conditions affect the surface thickness and roughness. The polished area shows a lower d_{EMA} than the unpolished one, which demonstrates the effectiveness of scanning SHEL ellipsometry in assessing surface roughness. This technique, which employs the EMA model, is particularly well-suited for samples with a known refractive index (n_2) to ensure precise analysis.

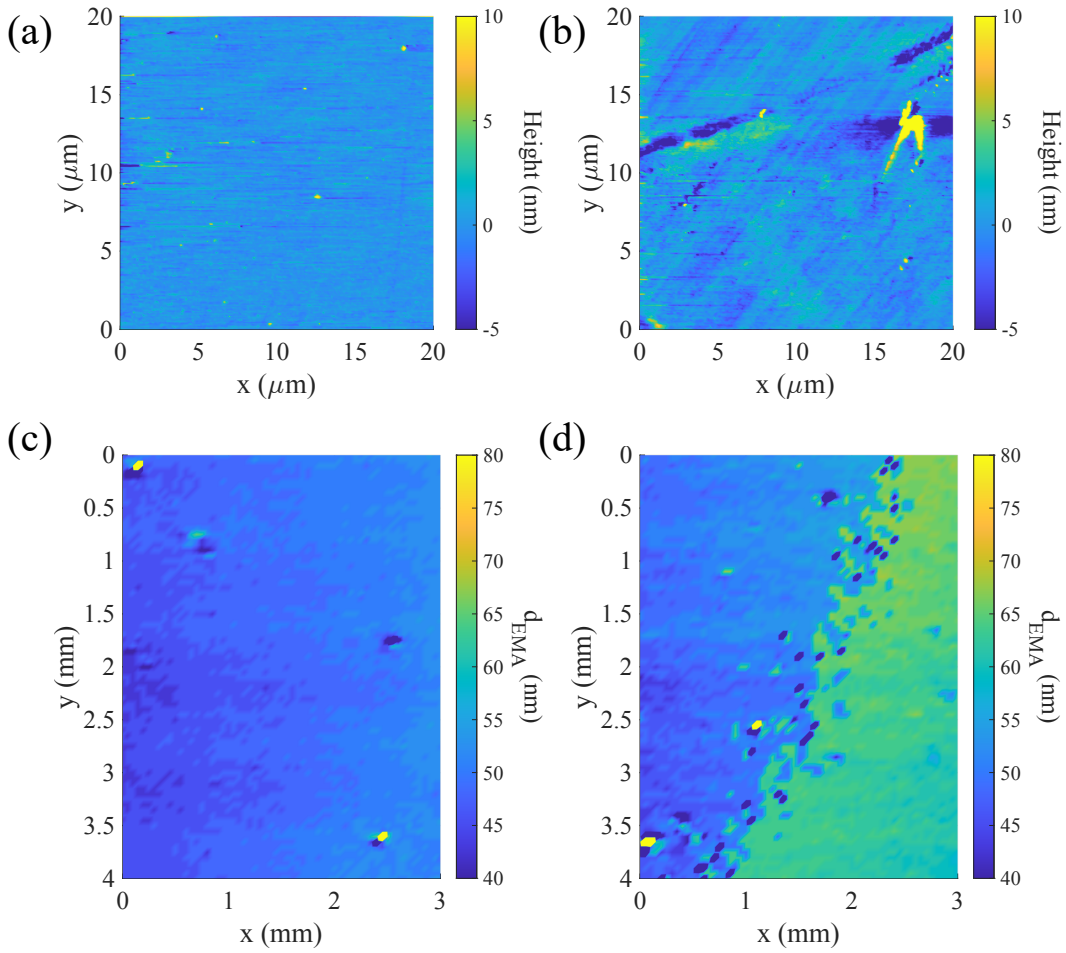


Fig. 3.19: Comparison scanning of AFM and SHEL ellipsometry of SiO_2 optical flat (a) AFM of polished surface, (b) AFM of unpolished surface, (c) SHEL ellipsometry of polished surface, (d) SHEL ellipsometry of unpolished surface

SHEL ellipsometry is considered an area-integrating technique since the surface data obtained from measurements at each location reflects the integral information of a specific area under the beam exposure [155]. Comparing AFM and SHEL ellipsometry results reveals that SHEL ellipsometry can effectively differentiate between polished and unpolished surfaces. However, an exact numerical comparison is not feasible due to the varying principles of surface extraction used [156, 157]. It is crucial to understand that a direct comparison between AFM and SHEL ellipsometry should not be made due

to the differing parameters and scanning areas; SHEL ellipsometry scans a much larger area compared to AFM [158].

Accuracy, precision, and repeatability form the foundation of any reliable measurement system, and these qualities are equally critical in the context of nanoscale optical metrology. Experimental validation suggests that the proposed SHEL ellipsometry framework demonstrates strong performance in terms of both precision and repeatability, as evidenced by the consistency of refractive index determination and the agreement of roughness scanning at the four quadrants. Comparatively, the scanning measurement shows a promising sensitivity to nanoscale surface variation, especially in the central part of the sample, where WLI shows its measurement limitation of susceptibility to fringe noise affecting the reconstruction (Fig. 3.16 (a)). Additionally, the comparative measurement of different degrees of polished surface also supports the powerful ability of SHEL compared to that of AFM. However, the lack of calibration standards for nanoscale roughness [159] limits the direct assessment of the accuracy. Additionally, specific angle parameters in SHEL ellipsometry play crucial roles that impact amplification and measurement results, yet compensating for angle error is also challenging, contributing to the uncertainty. Future studies should be made to assess the accuracy, such as correlation analysis between AFM and SHEL ellipsometry across varying known surface roughness levels.

This chapter demonstrates that SHEL observation using weak measurement is analogous to ellipsometry in that the polarization states of incident and reflected light are crucial. Since the polarizer pair in SHEL ellipsometry is not dynamically rotating and remains static during measurement, systematic error from the rotating retarder/analyzer will not be produced. Equally important is the fact that this method does not require a phase retarder, meaning it avoids the inherent temperature sensitivity associated with retarders. As a result, SHEL ellipsometry exhibits superior stability during extended measurements, as confirmed by scanning-based experiments. In terms of modeling flexibility, the framework allows surface properties to be described according to the assumed medium: under the air-glass (smooth surface) assumption, the SHEL response can be interpreted through a distribution of pseudo-refractive indices, for thin film layer the SHEL response can retrieve the film thickness, whereas under the rough-surface

assumption, the characteristics are more appropriately expressed as an effective thickness within the Bruggeman EMA model.

Additionally, the sample mounted in the xy translation stage demonstrates the scalable SHEL ellipsometry from pointwise measurement in static mode and expandable to 1D scanning in either axis to raster scanning capable of performing reconstruction of surface conditions across the sample without limitations on the applicable area size. For the retrieval of refractive index and surface roughness, we have dealt with a non-absorbing medium. However, we also have shown that the varying thickness of gold nanofilm, which has a complex refractive index, shows agreement with the expectation, although the calculation of thickness was not performed. Nevertheless, the applicability of SHEL ellipsometry could be extended to accommodate materials with absorption by applying the expanded model available from the referenced literature [146, 147]. Moreover, the adoption of arbitrary incidence polarization angles would further broaden the method's flexibility and adaptability to different measurement conditions, thereby extending its range of usability.

The demand for subnanometer areal surface inspection is rapidly increasing with the advancement of materials, metasurfaces, and high-precision optical systems. This proposed instrument offers a simple hardware setup without sample size constraints while enabling nanoscale surface characterization. Although it does not provide direct measurements, its efficiency competes with existing methods such as AFM and SEM. Moreover, the inferred surface information can be flexibly modeled to suit different sample types, allowing SHEL ellipsometry to analyze a broad range of materials. This adaptability makes it valuable for diverse applications, from precision glass polishing to metamaterial development.

3.4 Conclusions

This chapter elucidates the demonstration of the Spin Hall Effect of Light as a basis for measuring several physical properties that are conventionally accessed through ellipsometry. Firstly, the confirmation of the theoretical model of the three targeted parameters with the experiment shows a good agreement, establishing confidence in the proposed SHEL ellipsometry as an optical measurement tool. Moreover,

the influence of the post-selected azimuth angle on the measurement result is evident from the retrieval of the pseudo-refractive index. Secondly, the 1D scanning of the varying gold film thickness shows how SHEL can reconstruct the surface morphology information, with the measured shift showing a relation to the varying deposition time. Third, scanning SHEL ellipsometry successfully reconstructed nanometer-scale surface features, where comparative measurements of polished and unpolished samples validated SHEL ellipsometry as a novel roughness characterization technique. The effective roughness could be expressed in terms of either a pseudo-refractive index or an equivalent roughness thickness d_{EMA}, depending on the available knowledge of the sample properties.

SHEL ellipsometry demonstrated high sensitivity to parameter variations at the interface, enabling nanoscale measurement across arbitrary sample sizes and providing rapid assessments over large illuminated areas. However, similar to other nanometer-scale instruments, validating the absolute thickness and roughness values obtained from SHEL ellipsometry remains challenging. Future assessment methods may include correlation analysis or the development of calibration procedures and techniques.

Nevertheless, the work presented in this chapter has been a proof-of-concept of the proposed SHEL ellipsometry. While the feasibility of retrieving surface and optical parameters has been established, the issue of the enlarged SHEL shift near the Brewster angle has not been addressed in detail. As evaluated in this chapter, the SHEL shift for horizontal polarized incidence shows an interesting feature that implies potential for increased measurement sensitivity around the Brewster angle. The following chapter, therefore, investigates SHEL ellipsometry operated near Brewster incidence, focusing on how to access the angular incidence in this range and how this enhancement can improve the measurement of SHEL ellipsometry.

Chapter 4

High Sensitivity Measurement at Near Brewster Incidence

4.1 Introduction

Building on the demonstration of SHEL ellipsometry in the previous chapter, this chapter focuses on the observation and application of the SHEL shift near Brewster's angle. Since SHEL is inherently dependent on the incidence angle, its behavior is particularly distinctive under conditions where the Fresnel reflection coefficients exhibit strong polarization asymmetry. For horizontally polarized ($|H\rangle$) incidence, this occurs near the Brewster angle, where $r_p \to 0$, leading to a pronounced amplification of the SHEL shift.

Several related studies have pointed out the potential of Brewster-incidence SHEL for enhancing measurement sensitivity. However, a well-known challenge persists: the conventional SHEL theoretical model often deviates from experimental results in the immediate vicinity of the Brewster angle. Understanding this discrepancy and determining how to exploit the Brewster condition effectively remains essential for advancing SHEL-based metrology.

This chapter explains in detail the physical significance of Brewster's angle in the SHEL phenomenon

and addresses the mismatch between theory and experiment. Numerical simulations are first presented to examine the angle dependence of the SHEL shift, both with respect to the incidence angle and the weak measurement post-selection parameter. These predictions are then experimentally tested, comparing SHEL shifts observed at far-from-Brewster and near-Brewster incidence. Finally, the near-Brewster configuration is employed for three representative measurement applications: refractive index characterization, gradual thickness variation in nanogold films, and areal surface roughness mapping. Through these studies, this chapter discusses how operating near Brewster's angle, together with optimized weak measurement parameters, unlocks the enhanced sensitivity of SHEL ellipsometry.

4.2 Anomaly of SHEL Shift at Brewster Angle

4.2.1 Polarization and Angular Dependence of SHEL

Even though beam shifts can occur during both transmission and reflection, they are generally more pronounced in reflection, making the reflective configuration more suitable for precision measurements. In the case of the SHEL shift, it is commonly observed using a Gaussian beam with linear polarization as the incident light. The simplest form of linear polarization is horizontal and vertical polarization, and the combination of both can be used to define any arbitrary orientation of polarization.

Since SHEL is a polarization-dependent phenomenon, the regulation of the polarization behavior upon reflection also applies, which includes its anomalous behavior at the Brewster angle. One of the propositions of polarization behavior on reflection from transparent media is considering the Brewster angle, which is related to the refractive indices of the media at the interface $\theta_B = \tan^{-1} \frac{n_2}{n_1}$ with $n_2 > n_1$ where both are the refractive indices [160]. At θ_B, the p-polarized component is completely transmitted, meaning the reflection coefficient instantly becomes zero. This phenomenon can be understood through the calculation of the complex Fresnel reflection coefficient for a range of incident angles, assuming a He-Ne laser propagates from an air medium incident on a fused silica with a refractive index of 1.45, the result is shown in 4.1 (a). As can be seen, the value of r_p extinct at $\theta_i = \theta_B$ while r_s remains.

Consequently, when the incident beam is unpolarized, then the reflected beam will be $s-$polarized, but if the incident beam is $p-$polarized, then no reflection is observed, as illustrated in panels (b) and (c), respectively.

As described in (2.9)-(2.10), the magnitude of the SHEL shift depends on the ratio of the Fresnel reflection coefficient representing the polarization dependence; additionally, it also has a dependency on the incidence angle. Since the p-polarized component is suppressed at the Brewster angle ($r_p = 0$), it affects the Fresnel coefficient ratio between s and p components in (2.9). When $r_p \to 0$, which is in the area near the Brewster angle, the Fresnel ratio $\frac{r_s}{r_p}$ is getting exponentially larger, as shown in the red dashed line in 4.1 (a), resulting in a significant growth of the SHEL shift accordingly. Conversely, in the incident angle far from the Brewster region, the Fresnel ratio is smaller, corresponding to a reduced shift amplitude [108]. Additionally, the SHEL shift changes sign around the Brewster angle, due to the phase discontinuity in the reflection coefficient, characterized by a phase jump of π [108, 161]. Because both the amplitude and phase of the Fresnel coefficients are sensitive to the incident angle and the optical properties of the interface, the Brewster region offers heightened sensitivity, making it especially valuable for sensing applications.

Previously in Chapter 3, we have shown the general behavior of SHEL shift observation under both the $|H\rangle$ and $|V\rangle$ incidence, where it shows how the feature of SHEL shift is significantly different. Upon $|H\rangle$ incidence, the SHEL shift on varying incident angle shows a considerably larger range than that upon $|V\rangle$ incidence. Upon $|H\rangle$, the SHEL shift upon reflection from the bulk substrate is shown resonating at the sample's corresponding Brewster incident as shown in 4.2 (a). The curves appear to be shifted in the direction of the incident angle. When the curves cross the $y = 0$ axis, the incident angle coincides with the Brewster angle, shown by the horizontal line of each curve. This behavior is particular for $|H\rangle$ incidence due to the p-polarized component.

For the other two cases of multi-reflection interface of film thickness and thickness equivalent surface roughness, the SHEL shift behavior upon $|H\rangle$ incidence is shown in Fig. 4.2 (b) and (c). In (b), the interface model assumes a nanogold film on top of a SiO_2 substrate with varying thickness; on the other

hand, (c) shows the interface of SiO_2 with varying roughness in equivalent thickness value. This figure shows how the SHEL, due to varying physical parameters, is more prominent in the region near the Brewster angle. Moreover, Fig. 4.2 (d) shows how SHEL shifts to varying equivalent thickness values at different incident angles, highlighting the sensitivity represented by the curve's slope, where the incident angle near the Brewster angle shows a higher slope, representing higher sensitivity. Intuitively, for SHEL-based measurement, it will be significantly easier to distinguish different properties in the area near Brewster incidence than in a region far from the sample's Brewster angle. It is important to note that in the multi-reflection interface cases, the Brewster angle corresponds to that of the bulk substrate. From this theoretical foundation and calculation, we can infer that exploiting the near Brewster incidence benefits measurement.

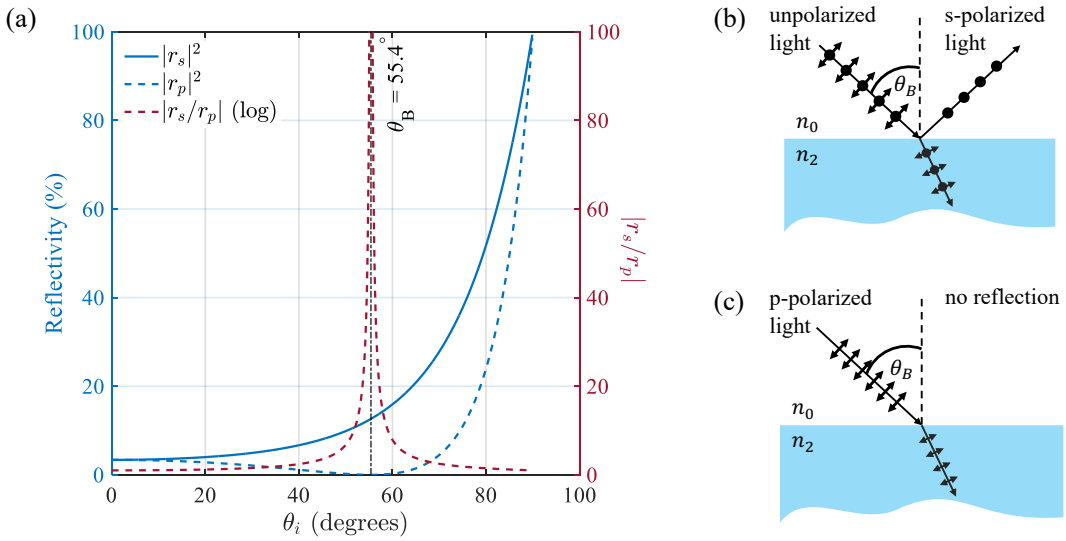


Fig. 4.1: (a) Calculation of Fresnel reflection coefficient and illustration of the polarization component at Brewster angle incident (b) for unpolarized incident beam, (c) for p-polarized incident beam

4.2.2 Angular Parameter in Weak Measurement Observation of SHEL

As previously mentioned, the SHEL is highly dependent on the incident angle in an oblique configuration, where variations in this angle significantly influence the magnitude of the SHEL displacement. In addition to the incident angle, the azimuth angle (ε) plays a pivotal role in weak measurement schemes used to observe the SHEL shift, as it directly affects the amplification factor described in (2.46) to (2.49). Typically, the choice of ε is made based on experimental intuition. It is usually kept small (e.g., $\varepsilon < 5°$) to maintain the near-orthogonality condition between pre- and post-selected states [100, 162]. Nevertheless, choosing a value that is too small can compromise the weak interaction regime [145]. For a fixed incident angle, there exists a specific azimuth angle that optimizes the amplification [162].

Figure 4.3 illustrates the computed SHEL displacement across a range of incident angles for azimuth angles between 0.25° and 5°. The analysis is based on the air-glass interface using the modified weak measurement model in (2.48). As shown, the amplified shifts exhibit an antisymmetric trend centered around the Brewster angle θ_B. Increasing ε leads to a steeper response, indicating the combined influence of both angular parameters on the observed SHEL shift.

Earlier studies have highlighted the difficulty in measuring SHEL near θ_B, primarily due to discrepancies between theoretical predictions and experimental results. One proposed workaround is to use $\varepsilon = 45°$ [144], which improves agreement between model and data near θ_B, although at the cost of losing weak value amplification, yielding a factor of 1, with any gain arising solely from the beam propagation factor. One of the findings in the previous chapter also implies that agreement between theoretical and experimental results can be improved by increasing ε.

This chapter demonstrates that it is still feasible to obtain amplified SHEL measurements near θ_B by adopting a considerably large ε, chosen to optimize post-selection angle. Figure 4.4 presents theoretical predictions of the amplification behavior across angular parameter space. The amplification factor ($G_{Amod} = \delta^H_{Amod}/\delta^H_r$) accounts for both weak value enhancement and beam propagation. Figure 4.4 (a) provides a two-dimensional map of G_{Amod} with respect to incident and azimuth angles, with the red dashed line denoting θ_B for $n_2 = 1.45$. Notably, at $\varepsilon = 0$, no SHEL shift is observed,

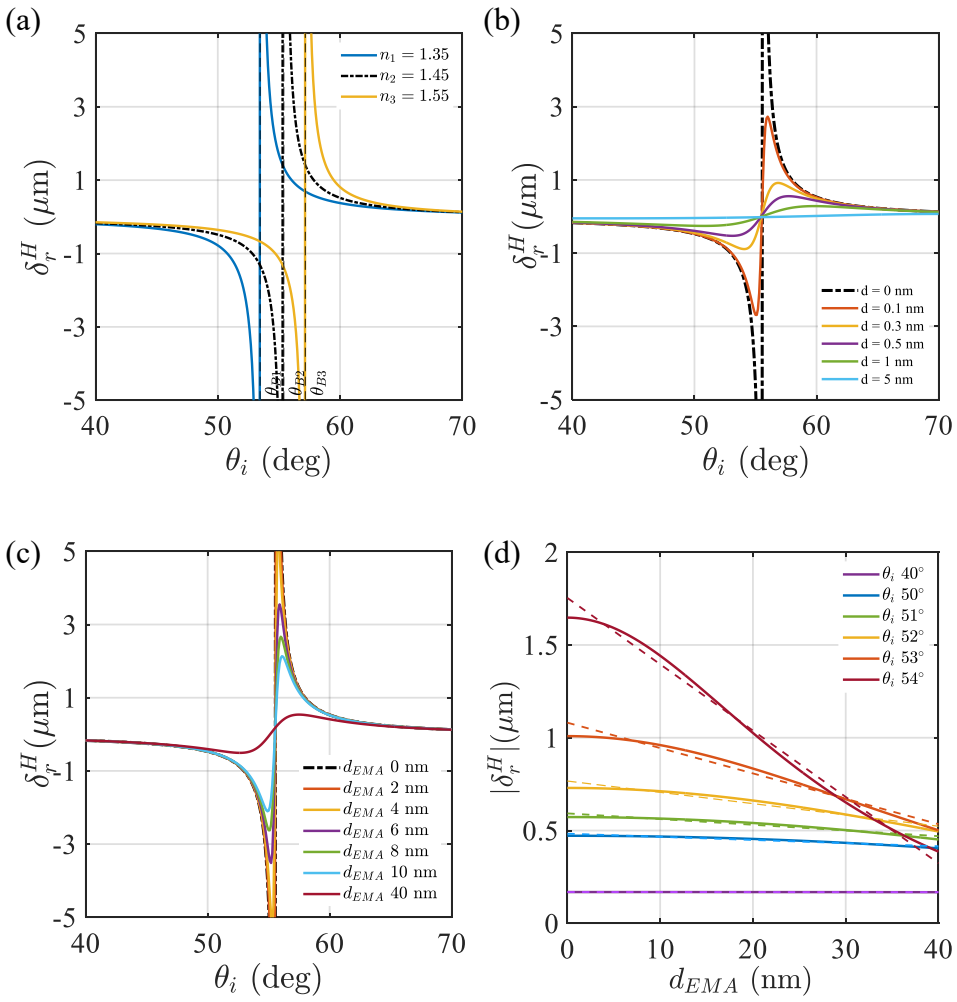


Fig. 4.2: Original SHEL shift to incident angle due to varying physical properties, (a) refractive index, (b) varying film thickness, (c) varying thickness equivalent surface roughness, (d) absolute SHEL shift to d_{EMA}

contradicting assumptions of exponential enhancement [162]. A darkened region near θ_B represents minimal amplification. Figure 4.4 (b) further visualizes G_{Amod} as a function of incident angle, with each line corresponding to a different ε. Solid lines represent conventional small angles [100, 162], while dashed lines reflect larger azimuth angles. Regardless of ε, the amplification consistently drops to zero at θ_B, highlighting the null SHEL shift at this point. While larger azimuth angles reduce the overall amplification, they broaden the angular range of gradual amplification variation, thus narrowing the region of rapid changes near θ_B. This behavior supports using a larger-than-usual azimuth angle for incident angles close to the Brewster angle. Figure 4.4 (c) shows the variation of amplification with ε for incident angles between 50° and 55°. The optimal ε for each incident angle, determined by $\partial G_{Amod}/\partial\varepsilon = 0$ [162], is marked by black circles. Lastly, Fig. 4.4 (d) plots the optimal ε against θ_i, highlighting that near-Brewster incidence requires a substantially large azimuth angle for effective SHEL measurement.

4.3 Observation of SHEL Shift at Near Brewster Incidence

The experimental setup, instrumentation, and components employed in this section are identical to those described in the preceding chapter. However, this subsection provides a more detailed account of the measurement procedures, particularly those related to the configuration of angular parameters. In addition, a more in-depth analysis is presented regarding the observations and the influence of angular parameters on the Spin Hall Effect of Light (SHEL) shift.

A common concern in SHEL-based experiments is ensuring the accuracy of the angular parameter configuration. The weak measurement scheme plays a crucial role in enabling the observation of the SHEL shift. A fundamental step in this process is verifying the occurrence of beam splitting. This begins with configuring the system for oblique incidence at a chosen angle, with polarizers P_1 and P_2 arranged in mutual orthogonality and no azimuthal offset ($\varepsilon = 0$). Under these conditions, a symmetrical beam splitting along the y-axis should be observable on the CCD, indicating the presence of the SHEL shift.

Figure 4.5 illustrates the expected beam profile at the CCD for specific angular configurations,

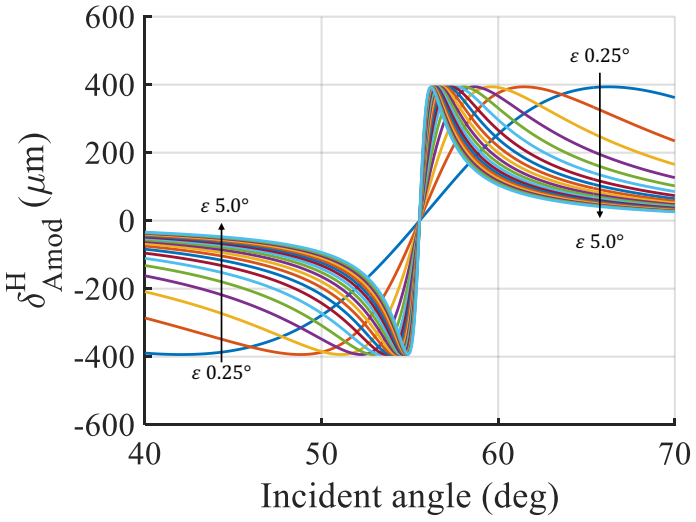


Fig. 4.3: Influence of the varying azimuth angle on Amplified SHEL shift

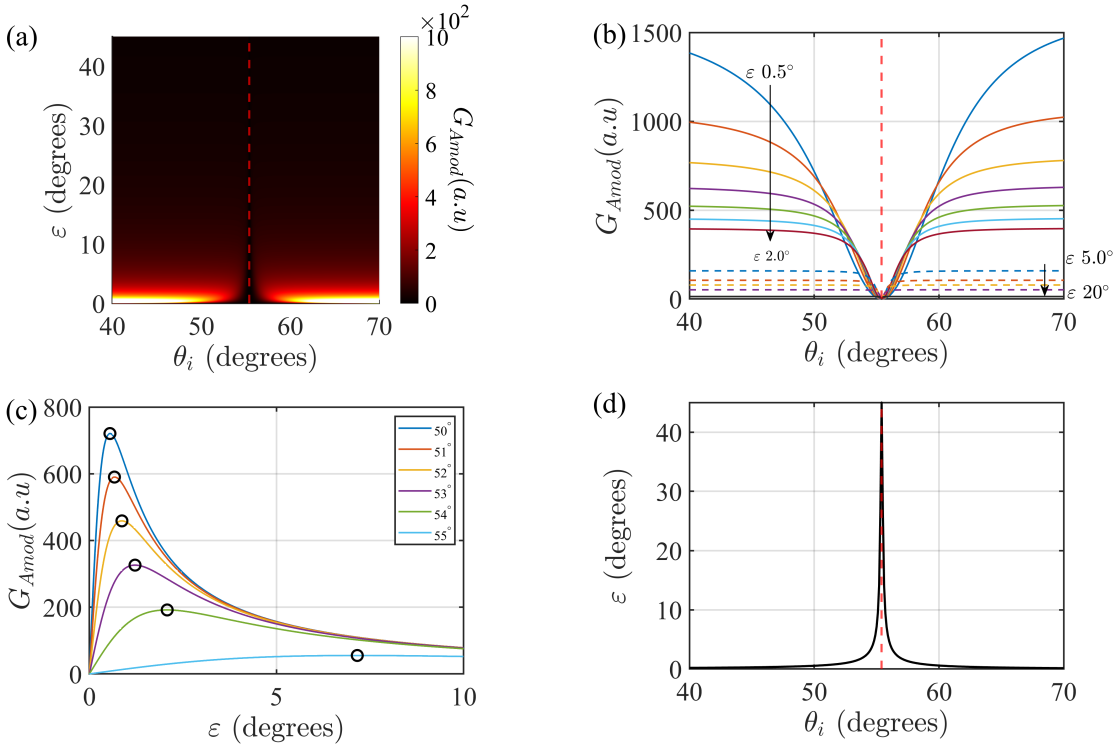


Fig. 4.4: Amplification factors $G_{Amod} = \delta^H_{Amod}/\delta^H_r$ in Weak Measurement Observation of SHEL, (a) influence of angular parameters, (b) influence of incident angle, (c) influence of azimuth angle, (d) optimal angular parameters

showing both simulated predictions and experimental results at incident angles of 50° and 60°. These angles are located on opposite sides of the Brewster angle of the sample. As shown in Fig. 4.3, $\theta_i = 50°$ is below the Brewster angle, whereas $\theta_i = 60°$ lies above it. The reversal in the direction of the SHEL shift across these angles under the same azimuthal conditions demonstrates the angular dependency of the phenomenon, with the shift direction changing as the incident angle crosses the Brewster threshold. Additionally, the sign of the azimuth angle reverses the shift direction but does not necessarily affect the magnitude of the shift. Therefore, in many cases, both the shift and the azimuth angle are considered in terms of their absolute values.

An intriguing question arises regarding how the beam with SHEL appearance is observed exactly at the Brewster incidence. Figure 4.6 displays the images of SHEL at the Brewster angle. At orthogonality, the same expected symmetrical beam-splitting profile is observed. The orthogonality at Brewster angle is also known as the null-reflection angle because at this state, the lowest intensity distribution is observed

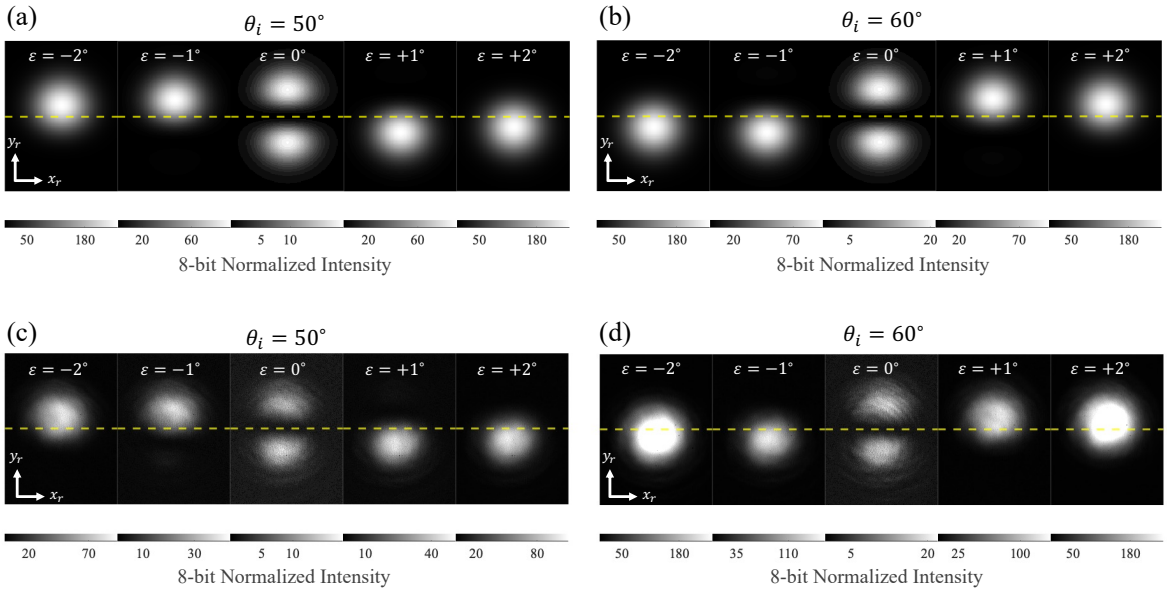


Fig. 4.5: SHEL shift simulation compared to the experimental observation (a) simulation at $\theta_i = 50°$, (b) simulation at $\theta_i = 60°$, (c) observation at $\theta_i = 50°$, (d) observation at $\theta_i = 560°$

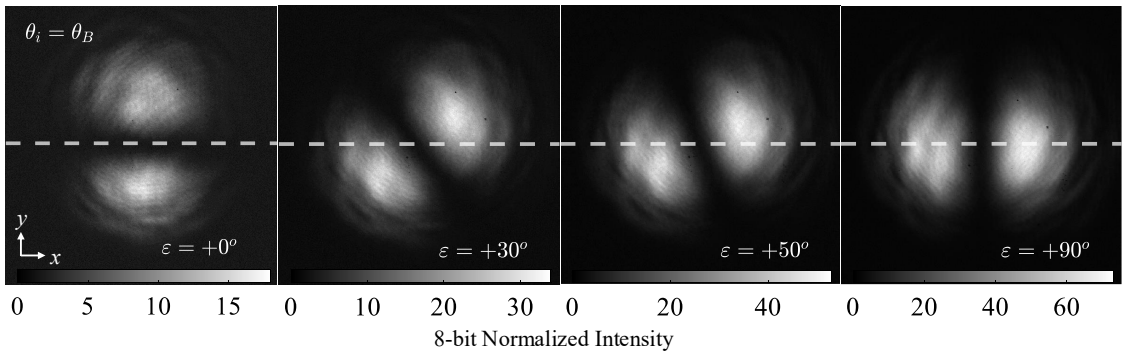


Fig. 4.6: Observation of SHEL shift at the Brewster angle

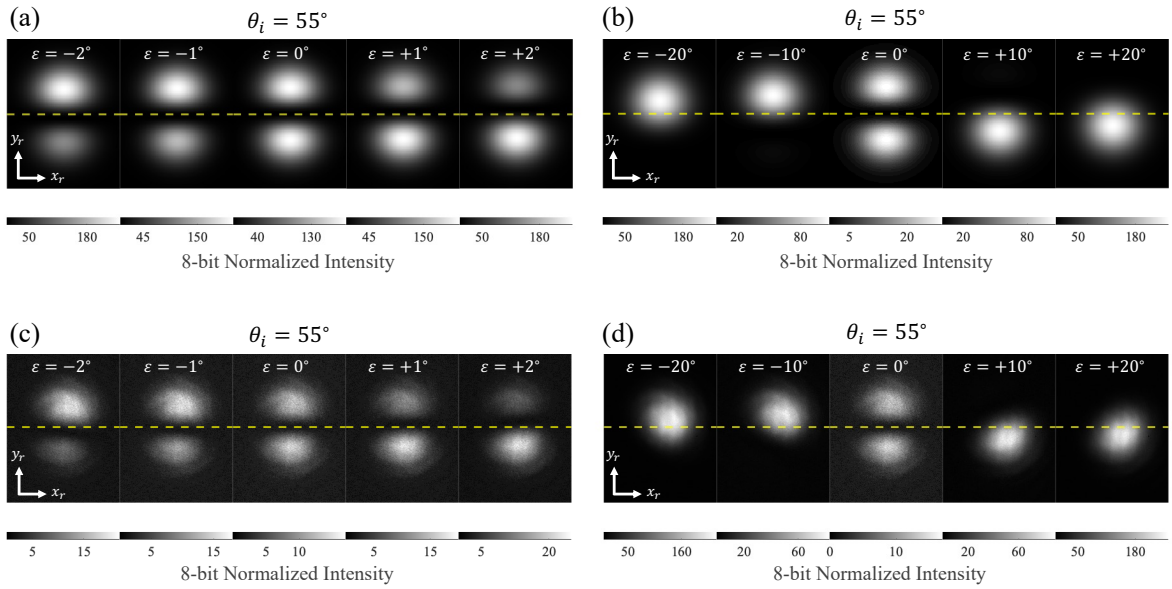


Fig. 4.7: SHEL shift simulation compared to the experimental observation at near Brewster incidence considering the optimal post-selected angle criteria (a) simulation with small ε, (b) simulation with large ε, (c) observation with small ε, (b) observation with large ε

due to $r_p = 0$. However, the null-reflection angle is different from the polarization angle since it's related to the orthogonality of the polarizers [163]. However, unlike how a small azimuth angle addition shifts the beam in y-direction shown in the previous figure, it will not affect the beam. When adding a large azimuth angle, even tens of degrees, the beam will not be shifted in y-direction, it appears as if the split beam is rotating at its centroid instead. This is the anomaly of the SHEL at Brewster angle that happens due to the dominance of the Goos-Hanchen or the in-plane spin shift at Brewster angle. Moreover, this anomaly strictly happens at Brewster incidence; a slight deviation of the incident angle will reduce the dominance of the in-plane spin shift and cause the SHEL shift to appear stronger. As can be seen from Fig. 4.6 when $\varepsilon = 90^\circ$ or when P_1 equals to P_2, the in-plane shift occurs. In this configuration, a slight deviation from the Brewster incidence will cause the beam splitting to be asymmetrical. Thus, this anomaly is advantageous in making sure the incident angle setup is accurate, given the refractive index of the target sample is known. On the other hand, when the refractive index of the sample is unknown, this anomaly can help approximate the refractive index through searching for this anomaly over a range of incident angles.

Lastly, observations of the SHEL beam in the region near the Brewster incident angle were conducted, taking into account the post-selected state, which forms the primary focus of this chapter. As indicated in Fig. 4.4(c), the optimal azimuth angle for an incident angle of $\theta_i = 50^\circ$ is found to be greater than 7°. Figure 4.7 presents both the theoretical prediction and experimental observation of the SHEL shift at near-Brewster incidence ($\theta_i = 55^\circ$), evaluated across two ranges of azimuth angles. Panels (a) and (c) show the observed beam profiles for azimuth angles smaller than the optimal value, while panels (c) and (d) correspond to azimuth angles exceeding the optimal range.

As shown in panels (a) and (c), beam splitting is still apparent but becomes increasingly asymmetrical, with one side displaying a more dominant intensity, an outcome anticipated when the azimuth angle is set below the optimal value. Conversely, panels (c) and (d) illustrate a more pronounced beam shift, consistent with the results shown in Fig. 4.5, which correspond to cases where the azimuth angle is sufficiently large. For SHEL shift-based measurements, the appearance of a clearly dominant beam

on the CCD serves as a reliable indicator that the weak measurement condition has been adequately achieved.

These systematic observations of the SHEL shift across varying angular parameters, including regions far from, near to, and at the Brewster angle, provide a valuable reference for the reliable implementation and interpretation of SHEL experiments.

4.4 Measurement of Physical Properties Using SHEL Ellipsometry at Near Brewster Incidence

Building on the understanding of angular parameters developed in the previous section, this part focuses on the application of SHEL ellipsometry in measuring physical properties. The roles of incident and azimuth angles, previously discussed in detail, are now applied in a practical measurement setup. By adjusting the post-selection angle in relation to the incident angle to achieve the desired amplification factor, measurements near Brewster incidence can be carried out effectively. The approach is tested through SHEL shift measurements to incident angle, followed by the retrieval of refractive indices, line scanning of varying film thickness, and surface scanning of a smooth optical window.

For the evaluation of the angular parameters through shift measurement, an optical flat made of fused silica (SiO_2) with specified n=1.458, a thickness of 3.3 mm, and a half-inch in diameter is used as the target sample. Figure 4.8 shows the measurement of amplified shift to incident angle represented by the orange circle in comparison to the theoretical calculation shown as a solid blue line. Panel (a) displays the measurements over a broad incident angle at the range of $40° - 70°$ with the commonly employed azimuth angle values of $\varepsilon = 1°, 1.5°, 2°$, while (b) focuses on a narrower range near the Brewster angle ($54° - 57°$), employing larger azimuth angles. As seen in panel (a), the measured shift generally agrees with the theoretical calculation up to a certain point. A noticeable discrepancy between measurement and calculation arises near Brewster incidence, particularly at the region where the slope of the shift-versus-angle curve undergoes a reversal, showing that the commonly employed azimuth angle

is ineffective for near Brewster incidence. As the azimuth angle increases, the discrepancy gets smaller. In Fig. (b) the larger azimuth angles are employed ($\varepsilon = 5°, 10°, 15°$) for the narrow range of incident angle near Brewster incident, where the measured shift agrees very well with the theoretical value and demonstrates that the measurement near Brewster's incidence has been enabled by enlarging the ε while still preserving the amplification factor from weak measurements.

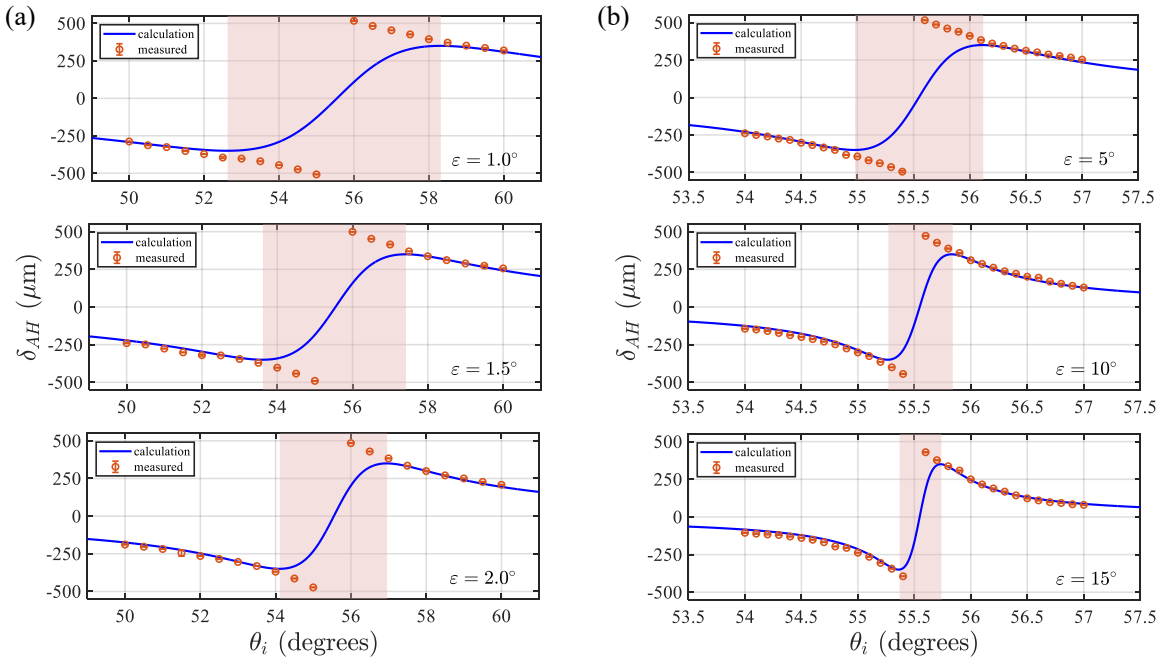


Fig. 4.8: Observation of SHEL shift to incident angle at different regions (a) far from Brewster angle and (b) near Brewster incidence, considering the optimal post-selected angle criterion

After the shift measurement, the pseudo-refractive index of the sample can be retrieved by solving the SHEL ellipsometry model based on the air-glass interface model. Table 4.1 and Table 4.2 display the retrieved pseudo-refractive indices from the parameters from Fig. 4.8 (a) and (b), respectively. In Table 4.1, no valid solution can be obtained from the calculation for incident angles between 54° and 57°, as the measured shifts deviate significantly from the expected theoretical values. Similarly, for $\theta_i = 53°$ and $\theta_i = 58°$, the calculation fails when the azimuth angle is set to $\varepsilon = 1.0°$. This sort of retrieval failure is more likely when the chosen azimuth angle is smaller than the optimal value required at each incident angle, as illustrated in Fig. 4.4. For instance, at $\theta_i = 53°$ and 58°, it is advisable to select azimuth angle values greater than 1°. Table 4.2 summarizes the calculated pseudo-refractive indices, demonstrating that increasing the azimuth angle ε enables solutions in the near-Brewster incidence regime. The associated percentage errors remain within an acceptable range, confirming that reliable measurements can be obtained near Brewster incidence. Consistent with earlier observations, no solution is found at $\theta_i = 55°$ when $\varepsilon = 5°$, as this value falls below the optimal azimuth angle required for successful extraction. In contrast, at $\theta_i = 56°$, a solution is obtainable with $\varepsilon = 5°$, even though the optimal value is slightly lower at 4.76°, suggesting that factors beyond azimuth angle selection may contribute to discrepancies. These findings imply that the optimal azimuth angle at each incident angle serves as a practical lower bound for experimental implementation.

$$\varepsilon > \varepsilon_{opt} \tag{4.1}$$

Following the initial measurements, the experimental setup was employed to characterize a nanogold film deposited on a SiO_2 substrate. The sample was fabricated via gold sputtering, producing five distinct regions corresponding to deposition times of 0 s, 60 s, 120 s, 180 s, and 240 s, respectively. As deposition time correlates linearly with film thickness, a one-dimensional thickness profile could be reconstructed by scanning across the sample. The measurement was performed by fixing the incident angle and selecting a specific azimuth angle, while translating the sample along the x-axis. At each position along the scan line, a local thickness was inferred based on the measured beam shift.

Table 4.1: Pseudo refractive index n and corresponding percentage error for different incident angles θ_i.

θ_i	n			error (%)		
	$\varepsilon = 1.00°$	$\varepsilon = 1.50°$	$\varepsilon = 2.00°$	$\varepsilon = 1.00°$	$\varepsilon = 1.50°$	$\varepsilon = 2.00°$
50	1.4834	1.4666	1.4525	1.74	0.59	0.38
51	1.4644	1.4683	1.4566	0.44	0.71	0.10
52	n/a	1.4722	1.4692	n/a	0.97	0.77
53	n/a	1.4612	1.4638	n/a	0.22	0.40
58	n/a	1.4454	1.4465	n/a	0.86	0.79
59	1.4440	1.4301	1.4460	0.96	1.92	0.82
60	1.4252	1.4359	1.4554	2.25	1.52	0.18

Table 4.2: Refractive index n and corresponding percentage error at different incident angle θ_i for near Brewster incidence operation.

θ_i	n			error (%)		
	$\varepsilon = 5°$	$\varepsilon = 10°$	$\varepsilon = 15°$	$\varepsilon = 5°$	$\varepsilon = 10°$	$\varepsilon = 15°$
54	1.4578	1.4544	1.4470	0.02	0.24	0.76
54.5	1.4569	1.4593	1.4501	0.07	0.09	0.54
55	n/a	1.4608	1.4592	n/a	0.19	0.09
56	n/a	1.4510	1.4496	n/a	0.48	0.58
56.5	1.4528	1.4511	1.4422	0.36	0.48	1.08
57	1.4528	1.4399	1.4308	0.36	1.24	1.86

Figure 4.9 displays the detected shift along the scan line for two measurement configurations: $\theta_i = 51^\circ, \varepsilon = 2^\circ$ (solid blue line) and $\theta_i = 54^\circ, \varepsilon = 5^\circ$ (dashed red line), corresponding to far-from and near Brewster incidence, respectively. The step-like pattern in the data reflects the discrete deposition zones. Notably, the measurement at $\theta_i = 51^\circ$ fails to resolve all five regions, with the third and fourth areas appearing merged, indicating low contrast at this angle. On the other hand, the near-Brewster configuration successfully captures all five steps, clearly resolving each deposition region. This result further confirms that near-Brewster incidence enhances the sensitivity of SHEL-based film thickness measurements due to the better contrast of the shift.

To conclude the experimental investigations, a two-dimensional scan was carried out to generate a spatially resolved optical surface profile of the target sample, which consisted of a half-inch SiO_2 optical window. In this procedure, the sample was systematically raster-scanned along both the x and y axes, with the Spin Hall Effect of Light (SHEL) shift being recorded at each scanning point. The resulting data produced a two-dimensional map corresponding to the local variations in effective thickness caused by surface roughness, thereby enabling a detailed reconstruction of the sample's surface topography. The outcomes of this scan are illustrated in Fig. 4.10. The measurement covered a surface area of 4 mm $\times$ 5 mm, utilizing a step size of 50 μm to ensure high spatial sampling resolution.

As a reference, atomic force microscopy (AFM) measurements revealed a surface roughness value (Sa) of approximately 1.2 nm across a 20 μm $\times$ 20 μm area on the rear surface, and 0.6 nm on the front surface of the window, AFM reconstruction can be found in Fig. 3.19 (a) and (b). As evident from Fig. 4.10, the configuration employing near-Brewster incidence yields a more pronounced and detailed surface profile compared to the configuration using an incident angle farther from Brewster's angle. This observation reflects an improvement in spatial resolution and measurement sensitivity, highlighting the advantage of operating near Brewster's angle in SHEL-based surface profiling.

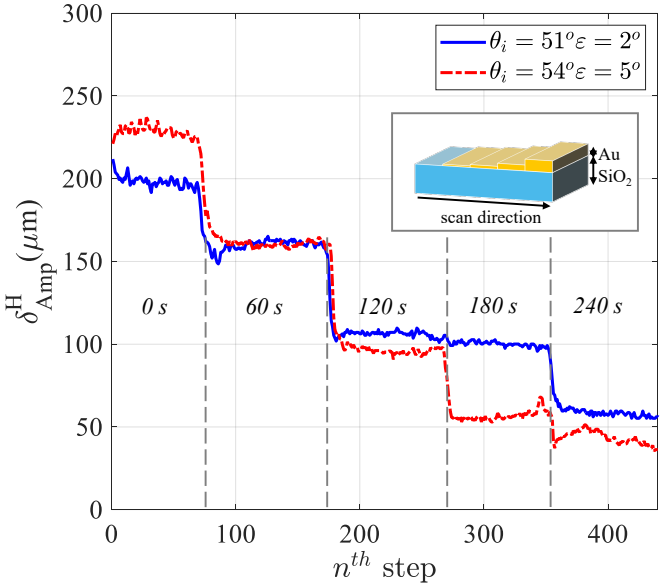


Fig. 4.9: Comparison of SHEL shift due to nanofilm thickness observed at different regions

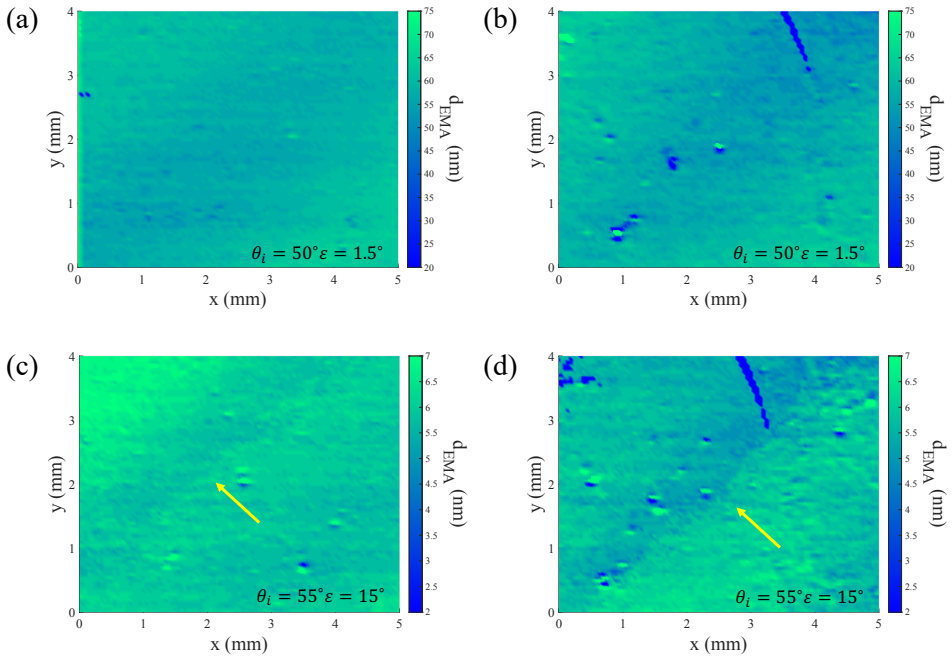


Fig. 4.10: Surface roughness measurement using SHEL ellipsometry observed at different regions (a) front face, (b) rear face, (c) front face with near Brewster incidence, (d) rear face with near Brewster incidence

4.5 Comparison to Conventional Ellipsometry

One of the most important questions regarding the development of SHEL ellipsometry is the benchmarking to conventional ellipsometry. Here, a systematic comparison was designed to evaluate the performance of SHEL ellipsometry compared to a conventional one. Rotating analyzer ellipsometry (RAE) was employed as a reference technique to retrieve the ellipsometry parameter ($|\rho|$) with the configuration set in the order of laser, polarizer, sample, analyzer, and a CCD camera. This configuration was selected due to its highest similarity compared to the setup used for SHEL ellipsometry. The parameter to compare is the absolute ellipsometry parameter, $|\rho|$. While SHEL ellipsometry retrieves ρ from the beam shift measurement, RAE retrieves ρ from intensity fitting.

In the RAE configuration, the incident beam was prepared in a diagonal linear polarization state (45° with respect to the plane of incidence) to represent equal value of $p-$ and $s-$ components, and was set by both the laser direction and the polarizer to get optimum intensity. The analyzer was rotating in the range of 0 to 180 degrees for a step of 10 degrees to analyze the polarization change after reflection. The measurement was conducted for a range of incident angles of $50° - 60°$. Then CCD records the reflected intensity as a function of the analyzer angle (A_k) and producing a sinusoidal modulation from the interference between the $p-$ and $s-$polarized reflection components. For each incident angle, three datasets were recorded. For this comparison, the sample was SiO_2 optical flat that was used previously. For this measurement, since the sample is SiO_2, a lossless assumption is taken into account.

Because the RAE is an intensity-based measurement, a dark reference image (D_{avg}) was recorded to avoid any intensity bias. Subtracting (D_{avg}) from raw intensity images ($I_{raw}(x, y; A_k)$), obtained the corrected intensity images for each analyzer angle ($I_{corr}(x, y; A_k)$). Then, from the corrected intensity, a uniform range of interest (ROI) of 800×800 pixels is applied to all images, and the intensity at analyzer angle is defined as the integration of intensity over the fixed ROI.

$$I(A_k) = \sum_{(x,y)\in \mathrm{ROI}} I_{\mathrm{corr}}(x, y; A_k) \tag{4.2}$$

Following the calculation of intensity from each analyzer angle from $0° - 180°$, the intensity function at each incident angle was modeled to a standard sinusoidal function where the magnitude of the ellipsometry parameter can be retrieved based on the following relationship:

$$I(A) = a + bcos(2A) + csin(2A); c \propto |\rho| cos\Delta \tag{4.3}$$

$$|\rho| = \sqrt{\frac{1 + b/a}{1 - b/a}} \tag{4.4}$$

where a, b, and c are the fitting parameters and Δ is the phase difference. Since the assumption of the sample is lossless, then $\Delta \approx 0$. Figure 4.11 shows the RAE employs in this work including (a) the experiment configuration, (b) samples of recorded intensity at analyzer A, and (c-d) the measured intensity as a function of analyzer angle and its corresponding fitting. With this procedure, conventional ellipsometry and SHEL ellipsometry can be compared directly. For SHEL ellipsometry, the setting of ε at each θ_i follows the gain calculation so that the requirement in 4.1 is fulfilled.

The result of the measurement is shown in Fig. XX with RAE result presented as blue diamonds, while the SHEL result is presented in red circles, while the ideal value in the solid black line is calculated from the Fresnel formula for He-Ne laser propagating from air to SiO_2 ($n = 1.458$). These measurements confirm that SHEL ellipsometry accesses the same optical properties as measured by conventional ellipsometry. Both RAE and SHEL reproduce the V-shaped dependence $|\rho|$ with a minimum at the Brewster angle and closely follow the theory curve.

For incident angles far from the Brewster angle, it can be inferred that SHEL ellipsometry has a comparable accuracy to conventional ellipsometry. However, an interesting trend emerges in the vicinity of the Brewster angle (54°–56°). As explained before, in the vicinity of Brewster angle $|\rho|$ approaches zero sharply. Since the RAE is intensity-based, it shows some deviation at this region due to the intensity contrast collapse that leads to lower SNR, and makes it more susceptible to background light noise. On the other hand, SHEL data remains well-centered around the theory curve despite the low intensity contrast, showing its advantage in retaining measurement robustness where conventional ellipsometry becomes ill-conditioned. Another advantage of SHEL ellipsometry compared to the intensity-based polarization analysis in conventional ellipsometry is also related to the SHEL anomaly behavior at the Brewster angle. In conventional ellipsometry or other intensity-based measurements, determining the Brewster angle location with precision is a challenging task. On the other hand, SHEL overcame this challenge by exploiting the anomaly at Brewster angle, as shown previously in Fig. 4.6. A small deviation of incident angle will result in asymmetrical splitting beam intensity in the $x-$direction when $P_1 = P_2$, leading to a more robust determination of incident angle and avoiding angular error. Lastly, the RAE data were obtained from three repeated measurements per angle, whereas the SHEL data represent averages over 30 repetitions. Despite the asymmetrical statistical sampling of the measurements, it still serves as a proper comparison to demonstrate SHEL ellipsometry performance in the realm of the ellipsometry technique.

An easy comparison between RAE to SHEL is summed up in Table 4.3.

Table 4.3: Comparison of conventional ellipsometry and SHEL ellipsometry

	Conventional Ellipsometry	**SHEL Ellipsometry**
Physical observable	Intensity-based measurement	Displacement-based measurement
Retrieved parameter	$\rho = r_p/r_s$	
Near Brewster angle behavior	Sensitivity degrades	Enhanced robustness
Sensitivity mechanism	Polarization extinction	Weak-value amplification

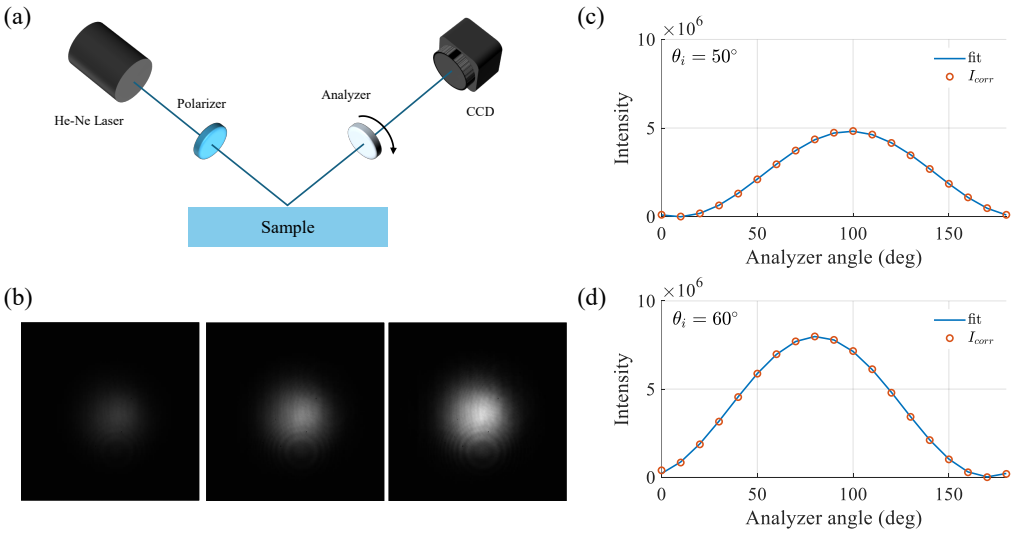


Fig. 4.11: Rotating analyzer ellipsometry (a) schematic of optical configuration, (b) samples of recorded intensity measurement (c-d) intensity as analyzer angle and the corresponding sinusoidal fitting

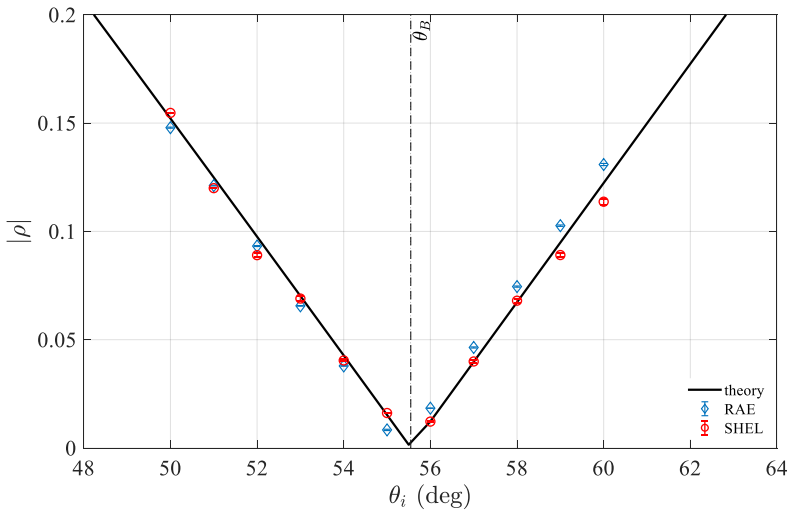


Fig. 4.12: Measurement results of $|\rho|$ from $50° - 60°$ from RAE and SHEL comparet to Fresnel formula theoritical calculation

The results presented in this chapter provide a comprehensive exploration of SHEL ellipsometry operated near the Brewster incidence and demonstrate how this regime enhances both the magnitude of the beam shift and the sensitivity of the measurement. The theoretical SHEL ellipsometry model reveals the angular dependency of SHEL shift, both the setup incidence angle and the weak measurement post-selected angle. The imbalance between the Fresnel reflection coefficients r_p and r_s near the Brewster angle for $|H\rangle$ leads to the amplification of the SHEL shift. By evaluating the amplification factor G_{Amod} of SHEL ellipsometry, the angular dependency is clarified and the mechanism by which the near Brewster condition can be accessed to improve the performance of SHEL ellipsometry.

Experimentally, the observations confirmed the theoretical predictions of amplified shifts near Brewster incidence (NBI) and showed that deliberate enlargement of ε based on the optimal post-selection minimized the discrepancy between theoretical and experimental values. The measurement implications were further demonstrated through three targeted parameter measurements. Refractive indices are successfully retrieved at NBI with a proper post-selection angle, resulting in an error of less than 1%. In the case of thin-film characterization, the gradual deposition of nanogold films was more clearly distinguished by the NBI, allowing precise monitoring of nanoscale thickness changes. Finally, in 2D area roughness mapping, the larger shift magnitudes translated into higher signal-to-noise ratios, enabling improved contrast and retrieving better spatial detail of the surface. Collectively, these applications highlight the practical utility of operating in the near-Brewster regime, where slight variations in optical or structural parameters can be captured with enhanced clarity. Furthermore, comparison between SHEL to RAE shows how SHEL ellipsometry accesses the same optical parameter at the interface to conventional ellipsometry, with SHEL ellipsometry demonstrating comparable accuracy for far from Brewster incidence, while showing enhanced sensitivity and robustness at near Brewster region. Additionally, SHEL ellipsometry has an advantage at the Brewster angle compared to conventional ellipsometry in determining the Brewster angle location.

Despite these advantages, several aspects remain to be refined. First, the present model neglected the explicit angular dependence of the Fresnel coefficients to simplify parameter retrieval. Several prior

works imply that incorporating this factor can increase the accuracy of SHEL ellipsometry; therefore, refined models should be considered [145, 147]. Second, both in Chapter 3 and in this chapter, the incidence angle chosen as an experiment parameter can be regarded as being relatively close to the Brewster angle, as these angles are defined as having a good sensitivity. For incident angles outside the high sensitivity window, for example $\theta_i < 45^\circ$ or $\theta_i > 65^\circ$ for SiO_2, SHEL shifts become vanishingly small, and the method may lose effectiveness. Hardware constraints may in practice prevent access to the optimal angular window, motivating exploration of techniques to boost sensitivity in such "out-of-range" conditions. One promising direction is the use of almost-balanced weak measurement (ABWM) schemes, where a pair of post-selected states is employed, for example, through utilizing a Wollaston prism. Prior studies have reported more than ten-fold amplification compared to standard weak measurement [164, 165], suggesting that ABWM could substantially extend the applicability of SHEL ellipsometry.

4.6 Conclusions

In this chapter, we demonstrate the application of the Spin Hall Effect of Light (SHEL) ellipsometry at near-Brewster incidence. Under this condition, the horizontally polarized beam exhibits a large SHEL shift, arising from the pronounced difference between the Fresnel reflection coefficients. A relatively large post-selection azimuth angle was employed, preserving the amplification effect and enabling accurate detection of the enhanced shift at near Brewster incidence.

SHEL ellipsometry with near Brewster incidence was successfully applied to three target parameter measurements. First, refractive indices can be retrieved with errors below 1%, confirming the method's quantitative accuracy. Second, the gradual deposition of nanogold thin films was resolved, demonstrating better sensitivity to nanoscale thickness variations compared to far from Brewster incidence. Third, two-dimensional scans of an optical window yielded spatially detailed roughness maps, where the reconstructions show improved surface profile. Together, these results establish near-Brewster SHEL ellipsometry as a precise, non-contact, and scalable tool for optical and structural characterization.

Comparison to rotation angle ellipsometry shows that SHEL ellipsometry accesses the same optical

parameter. While having comparable accuracy at far from the Brewster region, at the near Brewster region, SHEL ellipsometry offers high sensitivity and enhanced robustness for measurement compared to conventional ellipsometry, further validating its position in the realm of ellipsometric techniques.

At the same time, certain limitations remain. The current SHEL ellipsometry models neglect the angular dependence of Fresnel coefficients. Inclusion of this parameter in the SHEL ellipsometry model could further improve retrieval accuracy and needs to be explored. The reliance on angles in a good sensitivity window also constrains applicability, suggesting the need for a solution that can extend sensitivity to out-of-range incidence conditions. Promising future directions include the integration of almost-balanced weak value (ABWV) schemes for greater amplification and the development of reliable calibration procedures for absolute roughness and thickness measurements.

Overall, this chapter has addressed the angular requirements of SHEL ellipsometry and shown that operating near the Brewster angle unlocks the enhanced sensitivity of SHEL ellipsometry, strengthening its promising utility for non-invasive optical metrology.

Chapter 5

Conclusions

In this research, we have investigated the Spin-Orbit Interaction (SOI) of light, in particular the Spin Hall Effect of Light (SHEL), as the basis for a novel ellipsometer framework. Even though SHEL ellipsometry does not necessarily follow conventional ellipsometry concepts, it shares similarities with the widely known ellipsometry through several aspects: measurement based on the polarization-dependent interaction and employment of a pair of polarizers in an oblique setup. Ultimately, SHEL ellipsometry provides a scalable and extendable metrological tool capable of measuring multiple parameters (refractive index, thin film thickness, and surface roughness) in different schemes, from point-wise to 2D areal imaging. Since the parameter is derived from the subwavelength beam shift rather than ellipsometric angles, SHEL ellipsometry completely avoids the reliance on a constantly rotating element and temperature-sensitive retarder, common sources of instability in conventional ellipsometers. The proposed SHEL ellipsometry is developed in two stages: proof-of-concept and high-sensitivity measurement region, which leads to the establishment of a novel ellipsometric framework for metrology. The development of the concept has been deliberately discussed through the preceding chapters.

Chapter 1 presented the societal and technical background, motivation, and objectives of this work. It highlighted the demand for precision metrological tools in nanoscale material characterization and the limitations of each established instrument. We have touched on the conventional ellipsometry limitations

that include its reliance on rotating optical components and temperature-sensitive retarders, as well as the need for fast, stable, nanoscale metrology. In this chapter, we have also identified refractive index, thin film thickness, and surface roughness as target parameters, as these parameters are known to be simultaneously probed by ellipsometry, thereby defining the scope of the thesis. Besides that, the concept of spin-orbit interaction of light and its role in precision metrology has also been introduced.

Chapter 2 established the theoretical framework by positioning SHEL observation with weak measurement as the main logic of SHEL ellipsometry. As in conventional ellipsometry, SHEL ellipsometry approaches utilize polarization-dependent phenomena at an interface, with slight differences in observation and amplification through pre- and post-selected polarization states, achieved via weak measurement by a pair of polarizers. Additionally, amplification is also achieved from the Gaussian beam propagation factor manifested from a pair of telescopic lens systems. The optical interface model was shown to link material properties with polarization-dependent reflection, enabling the retrieval of physical parameters. Finally, a practical definition of beam displacement from an image-processing perspective was introduced, ensuring a consistent transition from theory to experiment. The chapter concluded with a definition of the SHEL ellipsometry model and an integrated flowchart summarizing the experimental procedure.

Chapter 3 presented the proof of concept for SHEL ellipsometry. Experimental demonstrations were carried out, and different parameters were investigated. The result confirmed that pseudo-refractive index retrieval aligns with actual values, showing significantly better measurement in horizontally polarized incidence. The varying thickness of the gold nanolayer deposited on different bulk substrates reflects as stair-like profiles in the observed line scan amplified SHEL shifts. The relation of the measured shifts to deposition time demonstrated how SHEL ellipsometry can reconstruct surface morphology evolution. A two-dimensional raster scan of the surface roughness shows good repeatability and stability of long-term measurement. Importantly, the areal scan result successfully distinguishes the difference of roughness as small as 0.6 nm from AFM results and presents it as equivalent EMA thickness. The roughness was shown to be representable either as a pseudo-refractive index or as an equivalent EMA thickness,

depending on prior knowledge of the sample. The measurement scheme was shown to be extendable from single-point to 2D areal mapping, demonstrating its scalability for specialized needs.

Chapter 4 builds upon the foundation in Chapter 3. As it is found that horizontally polarized incidence resulted in better accuracy and has an angular anomaly related to the Brewster angle, Chapter 4 extended the framework to high sensitivity measurement at near-Brewster-incidence (NBI) operation. Here, angular anomalies were observed: at the Brewster angle, the GH shift dominates, and the weak measurement parameter does not yield a transverse shift. This anomaly was shown to have two benefits: calibration of the incident angle when the Brewster angle is known, and refractive index estimation when it is unknown. To operate SHEL ellipsometry at NBI, the weak measurement parameter is not the same as those utilized at other incident angles. As there is a dependency of ε on θ_i, the optimal post-selected angle concept is found as the minimum limit of the measurement condition rather than as the best value. Validations were also carried out on the three parameters: refractive index, thin film thickness, line scanning, and 2D surface scanning. The refractive index retrieval achieved errors below 1%, confirming the quantitative accuracy of the method. In addition, nanoscale gold thin-film deposition was resolved with better sensitivity to thickness variations compared to far-from-Brewster incidence, and 2D scans produced improved roughness maps with enhanced surface profile reconstruction. The experimental validations confirm the enhanced sensitivity of SHEL ellipsometry by near Brewster incidence operation. Comparison to rotation angle ellipsometry shows that SHEL ellipsometry accesses the same optical parameter while offering high sensitivity and enhanced robustness in the near Brewster region.

Despite the promising performance demonstrated in Chapters 3 and 4, the applicability of SHEL ellipsometry is governed by several limitations that arise from the underlying optical physics, model assumptions, material constraints, and practical implementation of the technique. These limitations do not diminish the validity of the presented results. Instead, they define the operational domain within which SHEL ellipsometry provides reliable and meaningful information.

From an optical-physics perspective, SHEL originates from the spin-orbit coupling at reflection,

and the shift can be in the order of tens of nanometers or less prior to amplification. Consequently, weak-measurement amplification is required for experimental detection. Such amplification, however, remains valid only within the weak-coupling regime. When the interaction is too strong or the post-selected angle is too close to orthogonality, it can degrade achievable precision, as has been addressed in Chapters 3 and 4. Furthermore, as demonstrated in Chapter 4, SHEL response exhibits strong angular selectivity with maximal sensitivity occurring near the Brewster angle, where the Fresnel ratio is large. This behavior highlights the necessity of prior knowledge of the sample's optical properties in order to access the limited high-sensitivity angular range. Far outside this regime, the Fresnel ratio is reduced, leading to diminished sensitivity. In addition, because SHEL is inherently defined for finite optical beams rather than ideal rays, the technique is intrinsically sensitive to beam distortion and exhibits resolution constraints imposed by the beam size.

From a measurement point of view, the SHEL signal comes from the interaction of a finite-width Gaussian beam with the sample. In the two-dimensional raster scan in this work, the retrieved SHEL shifts represent spatially averaged values over the beam cross-section at the sample plane instead of strictly height-resolved measurements. As a result, the reconstructed surface profiles correspond to effective interface properties within each illuminated area. The lateral resolution of the reconstructed areal mapping is thus determined by the beam diameter and the scanning step size employed in the translation stage during experiments. Therefore, surface features with lateral dimensions smaller than the beam size are perceived as average and cannot be resolved individually.

The retrieval of the target parameter depends on the interface modelling, which shows a high requirement for interface knowledge and a well-defined physical model. Measurement of the surface roughness relies on the effective medium approximation. For the investigation in this study, the measured roughness amplitudes lie in the sub-nanometer to a few-nanometer range, as designed by the EMA requirement of roughness less than $\frac{\lambda}{10}$. EMA is most accurate for a surface with high spatial frequency or fine random roughness, and in contrast, is inaccurate for a low spatial frequency surface. In addition, EMA considers vertical height variation and is blind to lateral irregularity. The retrieved effective

thickness should not be interpreted as a direct geometry height, but rather as a model-dependent, optically equivalent parameter. Quantitative benchmarking with other instruments, therefore, requires consistent definitions and calibration procedures. Nevertheless, the comparative study presented in Chapter 3 demonstrates that SHEL ellipsometry yields results consistent with established techniques within its valid modeling regime. Surfaces with larger roughness amplitudes, lateral periodicity, or multiscale features are beyond the EMA regime and would require alternative modelling approaches.

With respect to spatial resolution, it is important to highlight that the present measurements demonstrate sub-nanometer sensitivity in the vertical/axial direction. In contrast, the lateral resolution remains fundamentally limited by the optical beam size and scanning strategy. This asymmetry between axial and lateral resolution highlights that SHEL ellipsometry is optimized for detecting subtle interfacial variations rather than resolving fine lateral topography.

Material-related limitations of SHEL ellipsometry are also important to be addressed. Materials lacking a suitable optical interface, insufficient refractive-index contrast, or coherent light–matter interaction capable of producing a measurable spin-dependent shift are unsuitable for SHEL ellipsometry measurements. An interface with a lack of refractive index contrast, such as two media with nearly identical refractive indices, is unfit for producing the necessary spin-dependent splitting. Highly rough or diffusive surfaces can scatter light excessively, thereby burying the weak SHEL signal. Strong optical absorption can further suppress SHEL and reduce robustness, posing practical challenges for measurement. By contrast, optically smooth dielectric, anisotropic materials, metals, and certain metamaterials have been shown to demonstrate the SHEL phenomenon in various studies, indicating that these material categories are not excluded in principle but may require more elaborate experimental configurations and modeling strategies.

From a practical standpoint, the fixed-angle, near-Brewster configuration employed in this dissertation reflects a trade-off between sensitivity and operational flexibility. While this configuration limits applicability outside a narrow angular range, it is well-suited for repeatable, high-throughput measurements under controlled conditions, as commonly required in semiconductor fabrication environments. In

this context, the material and implementation constraints of SHEL ellipsometry do not merely represent limitations but instead define a measurement regime that is well matched to semiconductor process monitoring and thin-film characterization.

The work presented in this dissertation enables several technically well-defined directions for further exploration. The use of structured beams carrying orbital angular momentum (OAM) offers a direct route to introducing additional spin-orbit coupling channels and enhancing SHEL sensitivity. Extensions to nanostructured, structure-layered, and metamaterial films would allow the method to probe engineered optical responses beyond smooth dielectric interfaces. Moreover, incorporating additional spin-orbit effects, such as those in vortex retarders, may enable full-polarization or more advanced ellipsometric schemes. The reliance on the limited angular sensitivity window that constrains SHEL ellipsometry suggests the need for approaches such as almost-balanced weak value (ABWV) schemes to extend applicability to the ”out-of-range” regime.

Beyond technical extensions, this work demonstrates that the Spin Hall Effect of Light, traditionally studied as a fundamental quantum optics phenomenon, can be systematically applied as quantitative metrology observables. By integrating spin–orbit interaction physics, weak measurement, and optical interface modeling into a coherent scheme, this dissertation establishes a new ellipsometry technique that uses spin-dependent beam displacement as the primary sensing mechanism, rather than intensity or phase alone. With scalability from pointwise to 2D mapping and extendability toward new beam types and material systems, SHEL ellipsometry positions itself as a complementary approach within optical metrology, suited for measurements requiring high sensitivity to nanoscale interfacial variations. In particular, this capability is directly relevant to semiconductor and nanofabrication applications, such as monitoring thin-film thickness, assessing interface quality, and evaluating surface roughness in dielectric and multilayer structures.

In conclusion, the results presented in this thesis establish SHEL ellipsometry as a practical measurement framework that translates fundamental concepts from quantum and spin–orbit optics into a robust optical metrology tool. This work demonstrates that phenomena traditionally regarded as subtle

or purely fundamental can be harnessed to achieve sub-nanometer sensitivity in realistic experimental conditions. This represents a concrete step toward bridging quantum-optical theory and industrially relevant measurement technologies.

Bibliography

[1] D. Schaming and H. Remita. Nanotechnology: from the ancient time to nowadays. *Foundations of Chemistry*, 17:187–205, 2015.

[2] J.E. Hulla, S.C. Sahu, and A. Hayes. Nanotechnology: History and future. *Human & Experimental Toxicology*, 34(12):1318–1321, 2015.

[3] Nadeem Baig, Irshad Kammakakam, and Wail Falath. Nanomaterials: A review of synthesis methods, properties, recent progress, and challenges. *Materials advances*, 2(6):1821–1871, 2021.

[4] G. Guisbiers, S. Mejía-Rosales, and F.L. Deepak. Nanomaterial properties: size and shape dependencies. *Journal of Nanomaterials*, 2012:180976, 2012.

[5] Samer Bayda, M. Adeel, T. Tuccinardi, M. Cordani, and F. Rizzolio. The history of nanoscience and nanotechnology: From chemical–physical applications to nanomedicine. *Molecules*, 25, 2019.

[6] S. Luby. Nanoscience – from manipulation of atoms to human needs. *European Pharmaceutical Journal*, 68:84–88, 2021.

[7] K. Khalid, X. Tan, H.F. Mohd Zaid, Y. Tao, C.L. Chew, D. Chu, M. Lam, Y. Ho, J.-W. Lim, and L.C. Wei. Advanced in developmental organic and inorganic nanomaterial: a review. *Bioengineered*, 11:328–355, 2020.

[8] S. Modi, Rajendra Prajapati, G. K. Inwati, Nikky Deepa, V. Tirth, V. Yadav, K. Yadav, S. M. Fakhrul Islam, Prakhar Gupta, Do-Hyeon Kim, and Byong hun Jeon. Recent trends in fascinating applications of nanotechnology in allied health sciences. *Crystals*, 2021.

[9] Abid Haleem, M. Javaid, R. Singh, Shanay Rab, and R. Suman. Applications of nanotechnology in medical field. *Global Health Journal*, 2023.

[10] N. Zheludev and E. Plum. Reconfigurable nanomechanical photonic metamaterials. *Nature nanotechnology*, 11 1:16–22, 2016.

[11] Takuo Tanaka and A. Ishikawa. Towards three-dimensional optical metamaterials. *Nano Convergence*, 4, 2017.

[12] Adrija Sinha, Faizan Z. Simnani, Dibyangshee Singh, A. Nandi, Anmol Choudhury, P. Patel, E. Jha, R.S. Chouhan, N. Kaushik, Y. Mishra, P. Panda, M. Suar, and S. Verma. The translational paradigm of nanobiomaterials: Biological chemistry to modern applications. *Materials Today Bio*, 17, 2022.

[13] Nadeem Joudeh and D. Linke. Nanoparticle classification, physicochemical properties, characterization, and applications: a comprehensive review for biologists. *Journal of Nanobiotechnology*, 20, 2022.

[14] P. Biswas, S.A. Polash, D. Dey, M.A. Kaium, A.R. Mahmud, F. Yasmin, S. Baral, M.A. Islam, T.I. Rahaman, A. Abdullah, T.I. Ema, D.A. Khan, S. Bibi, H. Chopra, M. Kamel, A. Najda, M. Fouda, U.S.M. Rehan, M. Mheidat, R. Alsaidalani, M.M. Abdel-Daim, and M.N. Hasan. Advanced implications of nanotechnology in disease control and environmental perspectives. *Biomedicine & Pharmacotherapy*, 158:114172, 2023.

[15] Nayem Hossain, Md. Hosne Mobarak, Mariam Akter Mimona, Md. Aminul Islam, A. Hossain, F. Zohura, and Mohammad Asaduzzaman Chowdhury. Advances and significances of nanoparticles in semiconductor applications – a review. *Results in Engineering*, 2023.

[16] Charles M. Lieber. Semiconductor nanowires: A platform for nanoscience and nanotechnology. *MRS Bulletin*, 36:1052–1063, 2010.

[17] Payal and P. Pandey. Role of nanotechnology in electronics: A review of recent developments and patents. *Recent Patents on Nanotechnology*, 2021.

[18] Sharidya Rahman and Yuerui Lu. Nano-engineering and nano-manufacturing in 2d materials: marvels of nanotechnology. *Nanoscale Horizons*, 2002.

[19] Mindy D. Bishop, G. Hills, T. Srimani, C. Lau, Denis Murphy, Samuel H. Fuller, J. Humes, A. Ratkovich, M. Nelson, and M. Shulaker. Fabrication of carbon nanotube field-effect transistors in commercial silicon manufacturing facilities. *Nature Electronics*, 3:492–501, 2020.

[20] J. Liddle and G. Gallatin. Nanomanufacturing: A perspective. *ACS Nano*, 10(3):2995–3014, 2016.

[21] C. Rao and K. Biswas. Characterization of nanomaterials by physical methods. *Annual Review of Analytical Chemistry*, 2:435–462, 2009.

[22] Ping-Chang Lin, Stephen Lin, Paul C. Wang, and R. Sridhar. Techniques for physicochemical characterization of nanomaterials. *Biotechnology Advances*, 32(4):711–726, 2014.

[23] B. Fadeel, A. Fornara, M. Toprak, and K. Bhattacharya. Keeping it real: The importance of material characterization in nanotoxicology. *Biochemical and Biophysical Research Communications*, 468(3):498–503, 2015.

[24] A. Iglesias-Juez, G. Chiarello, G. Patience, and M. Guerrero-Pérez. Experimental methods in chemical engineering: X-ray absorption spectroscopy—XAS, XANES, EXAFS. *Canadian Journal of Chemical Engineering*, 2021.

[25] Ying-Jie Zhu, Neal Olson, and T. Beebe. Surface chemical characterization of 2.5-microm particulates (pm2.5) from air pollution in salt lake city using TOF-SIMS, XPS, and FTIR. *Environmental Science & Technology*, 35(15):3113–3121, 2001.

[26] A. Priebe, J. Barnes, T. Edwards, Emese Huszar, L. Pethő, and J. Michler. Elemental characterization of al nanoparticles buried under a cu thin film – TOF-SIMS vs. STEM/EDX. *Analytical Chemistry*, 2020.

[27] Vinayak M. Adimule, B. Yallur, Debdas Bhowmik, and A. H. J. Gowda. Morphology, structural and photoluminescence properties of shaping triple semiconductor YxCoO:ZrO2 nanostructures. *Journal of Materials Science: Materials in Electronics*, 32:12164–12181, 2021.

[28] Lydia Ouarez, A. Chelouche, T. Touam, R. Mahiou, D. Djouadi, and A. Potdevin. Au-doped ZnO sol-gel thin films: An experimental investigation on physical and photoluminescence properties. *Journal of Luminescence*, 2018.

[29] H. Fujiwara, Joohyun Koh, P. Rovira, and R. Collins. Assessment of effective-medium theories in the analysis of nucleation and microscopic surface roughness evolution for semiconductor thin films. *Physical Review B*, 61:10832, 4 2000.

[30] R. Tokas, S. Jena, S. Thakur, and N. Sahoo. Effect of angle of deposition on micro-roughness parameters and optical properties of HfO_2 thin films deposited by reactive electron beam evaporation. *Thin Solid Films*, 609:42–48, 2016.

[31] A. Tejada, S. Braunger, L. Korte, S. Albrecht, B. Rech, and J. A. Guerra. Optical characterization and bandgap engineering of flat and wrinkle-textured FA0.83Cs0.17Pb(I1–xBrx)3 perovskite thin films. *Journal of Applied Physics*, 123:175302, 2018.

[32] A. Hamidi, K. Meziane, A. E. Hichou, T. Jannane, A. Liba, J. Haskouri, P. Amorós, and A. Almaggoussi. Refractive index controlled by film morphology and free carrier density in undoped ZnO through sol-ph variation. *Optik*, 158:1139–1146, 2018.

[33] G. Georgescu and A. Petris. Analysis of thickness influence on refractive index and absorption coefficient of zinc selenide thin films. *Optics Express*, 27(24):34803–34823, 2019.

[34] J. Gonzalez-Leal, R. Prieto-Alcón, M. Stuchlik, M. Vlcek, S. Elliott, and E. Márquez. Determination of the surface roughness and refractive index of amorphous as40s60 films deposited by spin coating. *Optical Materials*, 27:147–154, 2004.

[35] Chun Guo, M. Kong, Weidong Gao, and Bincheng Li. Simultaneous determination of optical constants, thickness, and surface roughness of thin film from spectrophotometric measurements. *Optics Letters*, 38(1):40–42, 2013.

[36] Peter Nestler and Christiane A. Helm. Determination of refractive index and layer thickness of nm-thin films via ellipsometry. *Optics Express*, 25:27077, 10 2017.

[37] Y. Akaltun, M. Yıldırım, A. Ates, and M. Yıldırım. The relationship between refractive index-energy gap and the film thickness effect on the characteristic parameters of cdse thin films. *Optics Communications*, 284:2307–2311, 2011.

[38] J. A. Pradeep and P. Agarwal. Determination of thickness, refractive index, and spectral scattering of an inhomogeneous thin film with rough interfaces. *Journal of Applied Physics*, 108:043515, 2010.

[39] Ichiko Misumi, Kentaro Sugawara, Ryosuke Kizu, Akiko Hirai, and Satoshi Gonda. Extension of the range of profile surface roughness measurements using metrological atomic force microscope. *Precision Engineering*, 56:321–329, 3 2019.

[40] Teodor P Gotszalk, Pawe l Janus, Andrzej Marendziak, and Roman F Szeloch. Uncertainty of atomic force microscopy measurements. *Optica Applicata*, 37:397–403, 2007.

[41] Hisayoshi Sato, Masanori O-Hori, and Kazuo Nakayama. Surface roughness measurement by scanning electron microscope. *CIRP Annals*, 31:457–462, 1 1982.

[42] C. Dwyer, C. Maunders, C. L. Zheng, M. Weyland, P. C. Tiemeijer, and J. Etheridge. Sub-0.1 nm-resolution quantitative scanning transmission electron microscopy without adjustable parameters. *Applied Physics Letters*, 100, 5 2012.

[43] James C Wyant. White light interferometry. In *Holography: a tribute to yuri denisyuk and emmett leith*, volume 4737, pages 98–107. SPIE, 2002.

[44] Sungtae Kim, Yangjin Kim, Naohiko Sugita, and Mamoru Mitsuishi. Surface measurement of silicon wafer using harmonic phase-iterative analysis and wavelength-scanning fizeau interferometer. *Precision Engineering*, 75:142–152, 5 2022.

[45] Mingyu Liu, Chi Fai Cheung, Mingjun Ren, and Ching-Hsiang Cheng. Estimation of measurement uncertainty caused by surface gradient for a white light interferometer. *Applied Optics*, 54:8670, 10 2015.

[46] P. Lehmann, S. Tereschenko, and Weichang Xie. Fundamental aspects of resolution and precision in vertical scanning white-light interferometry. *Surface Topography: Metrology and Properties*, 4, 2016.

[47] U. P. Kumar, W. Haifeng, N. K. Mohan, and M. P. Kothiyal. White light interferometry for surface profiling with a colour ccd. *Optics and Lasers in Engineering*, 50:1084–1088, 2012.

[48] Kaihua Cui, Qian Liu, Huang Xiaojin, Zhang Hui, and Lulu Li. Scanning error detection and compensation algorithm for white-light interferometry. *Optics and Lasers in Engineering*, 148:106768, 2022.

[49] Quangsang Vo, F. Fang, Xiaodong Zhang, and Huimin Gao. Surface recovery algorithm in white light interferometry based on combined white light phase shifting and fast fourier transform algorithms. *Applied optics*, 56 29:8174–8185, 2017.

[50] P. Hariharan and M. Roy. White-light phase-stepping interferometry for surface profiling. *Journal of Modern Optics*, 41:2197–2201, 1994.

[51] Poul Erik Hansen, Sabrina Rostgaard Johannsen, Søren Alkærsig Jensen, and Jonas Skovlund Møller Madsen. Enhanced measurement accuracy for nanostructures using hybrid metrology. *Frontiers in Physics*, 9, 1 2022.

[52] Morten Hannibal Madsen and Poul-Erik Hansen. Scatterometry—fast and robust measurements of nano-textured surfaces. *Surface Topography: Metrology and Properties*, 4:023003, 4 2016.

[53] C. Raymond, M. Murnane, S. Prins, S. Sohail, H. Naqvi, J. McNeil, and J. Hosch. Multiparameter grating metrology using optical scatterometry. *Journal of Vacuum Science & Technology B*, 15:361–368, 1997.

[54] Shao-Pow Lin, Lihong V. Wang, S. Jacques, and F. Tittel. Measurement of tissue optical properties by the use of oblique-incidence optical fiber reflectometry. *Applied optics*, 36 1:136–43, 1997.

[55] Jérémy Riviere, P. Peers, and A. Ghosh. Mobile surface reflectometry. *Computer Graphics Forum*, 35, 2014.

[56] Y. Mizuno, N. Hayashi, Hideyuki Fukuda, K. Song, and Kentaro Nakamura. Ultrahigh-speed distributed brillouin reflectometry. *Light, Science & Applications*, 5, 2016.

[57] D. E. Aspnes. Spectroscopic ellipsometry — past, present, and future. *Thin Solid Films*, 571:334–344, 11 2014.

[58] A. Sytchkova, A. Belosludtsev, Lina Volosevičienė, R. Juškėnas, and R. Simniškis. Optical, structural and electrical properties of sputtered ultrathin chromium films. *Optical Materials*, 2021.

[59] M. Hanchak, M. Vangsness, L. Byrd, J. Ervin, and John G. Jones. Profile measurements of thin liquid films using reflectometry. *Applied Physics Letters*, 103:211607, 2013.

[60] Gil Bashan, H. H. Diamandi, Y. London, Eyal Preter, and A. Zadok. Optomechanical time-domain reflectometry. *Nature Communications*, 9, 2018.

[61] B. Soller, D. Gifford, M. Wolfe, and M. Froggatt. High resolution optical frequency domain reflectometry for characterization of components and assemblies. *Optics express*, 13 2:666–74, 2005.

[62] B. Danielson and C. Whittenberg. Guided-wave reflectometry with micrometer resolution. *Applied optics*, 26 14:2836–42, 1987.

[63] E. Chason and T. Mayer. Thin film and surface characterization by specular x-ray reflectivity. *Critical Reviews in Solid State and Materials Sciences*, 22:1–67, 1997.

[64] A. Khassanov, Hans-Georg Steinrück, T. Schmaltz, A. Magerl, and M. Halik. Structural investigations of self-assembled monolayers for organic electronics: results from x-ray reflectivity. *Accounts of Chemical Research*, 48(7):1901–1908, 2015.

[65] Alexandra D. Easley, Tingang Ma, Chikaodinaka I. Eneh, Junyeong Yun, R. M. Thakur, and J. Lutkenhaus. A practical guide to quartz crystal microbalance with dissipation monitoring of thin polymer films. *Journal of Polymer Science*, 2021.

[66] Shyam Singh. Refractive index measurement and its applications. *Physica Scripta*, 65:167–180, 2002.

[67] R. Khan, B. Gul, Shamim Khan, H. Nisar, and Iftikhar Ahmad. Refractive index of biological tissues: Review, measurement techniques, and applications. *Photodiagnosis and Photodynamic Therapy*, page 102192, 2021.

[68] Jie Hu, T. Lang, and Guohua Shi. Simultaneous measurement of refractive index and temperature based on all-dielectric metasurface. *Optics Express*, 25(13):15241–15251, 2017.

[69] O. Boughdad, A. Eloy, F. Mortessagne, M. Bellec, and C. Michel. Anisotropic nonlinear refractive index measurement of a photorefractive crystal via spatial self-phase modulation. *Optics Express*, 27(21):30360–30370, 2019.

[70] A. Ródenas, G. Torchia, G. Lifante, E. Cantelar, J. Lamela, F. Jaque, Luis Roso, and Daniel Jaque. Refractive index change mechanisms in femtosecond laser written ceramic nd:yag waveguides: micro-spectroscopy experiments and beam propagation calculations. *Applied Physics B*, 95:85–96, 2009.

[71] C. Wochnowski, S. Metev, and G. Sepold. Uv–laser-assisted modification of the optical properties of polymethylmethacrylate. *Applied Surface Science*, pages 706–711, 2000.

[72] Robert W. Collins and Yeon-Taik Kim. Ellipsometry for thin-film and surface analysis. *Analytical Chemistry*, 62:887A–900A, 9 1990.

[73] T. V. Vorburger and K. C. Ludema. Ellipsometry of rough surfaces. *Applied Optics*, 19:561–573, 2 1980.

[74] G. Jungk. Possibilities and limitations of ellipsometry. *Thin Solid Films*, 234:428–431, 1993.

[75] J R Blanco, P J Mcmarr, and K Vedam. Roughness measurements by spectroscopic ellipsometry. *Applied Optics*, 24:3773–3779, 11 1985.

[76] Soe-Mie F. Nee. Ellipsometric analysis for surface roughness and texture. *Applied Optics*, 27:2819, 7 1988.

[77] R.M.A Azzam and N.M. Bashara. *Reflection and Transmission of Polarized Light by Stratified Planar Structures*, pages 267–363. North-Holland Publishing Company, 1977.

[78] D.E. Aspnes. Chapter 5 - the accurate determination of optical properties by ellipsometry. In Edward D. Palik, editor, *Handbook of Optical Constants of Solids*, pages 89–112. Academic Press, Burlington, 1997.

[79] H. Tompkins and E. Irene. *Handbook of Ellipsometry*. William Andrew, 2005.

[80] Hiroyuki Fujiwara. *Spectroscopic Ellipsometry: Principles and Applications*. John Wiley & Sons, Ltd, 2007.

[81] H. Reisinger. Minimization of errors in ellipsometric measurements. *Solid State Electronics*, 35:333–344, 1992.

[82] S. J. Fang, W. Chen, T. Yamanaka, and C. R. Helms. Comparison of si surface roughness measured by atomic force microscopy and ellipsometry. *Applied Physics Letters*, 68:2837, 3 1996.

[83] Prabha Durgapal, James R. Ehrstein, and Nhan V. Nguyen. Thin film ellipsometry metrology. In *The 1998 international conference on characterization and metrology for ULSI technology*, pages 121–131. ASCE, 4 1998.

[84] Wolfgang Budde. Photoelectric analysis of polarized light. *Applied Optics*, 1:201–205, 1962.

[85] P. S. Hauge and F. H. Dill. A rotating-compensator fourier ellipsometer, 1975.

[86] K. Postava, A. Maziewski, T. Yamaguchi, R. Ossikovski, Š. Višňovský, and J. Pistora. Null ellipsometer with phase modulation. *Optics express*, 12 24:6040–5, 2004.

[87] D. E. Aspnes and A. A. Studna. High precision scanning ellipsometer. *Applied Optics*, 14:220, 1975.

[88] Yasuhiro Mizutani and Yukitoshi Otani. Ellipsometry at the nanostructure. In *Ellipsometry at the Nanoscale*, pages 313–323. Springer, 2013.

[89] Shiyuan Liu, Weichao Du, Xiuguo Chen, Hao Jiang, and Chuanwei Zhang. Mueller matrix imaging ellipsometry for nanostructure metrology. *Optics express*, 23 13:17316–29, 2015.

[90] U. Wurstbauer, C. Roling, W. Wegscheider, M. Vaupel, P. Thiesen, and D. Weiss. Imaging ellipsometry of graphene. *Applied Physics Letters*, 97:231901, 2010.

[91] Daesuk Kim, V. Dembele, Sukhyun Choi, G. Hwang, S. Kheiryzadehkhanghah, C. Joo, and R. Magnusson. Dynamic spectroscopic imaging ellipsometry. *Optics Letters*, 47(5):1129–1132, 2022.

[92] T. Alcaire, D. Le Cunff, S. Soulan, and J. Tortai. On-the-fly ellipsometry imaging for process deviation detection. *IEEE Transactions on Semiconductor Manufacturing*, 35:432–438, 2022.

[93] P. D. Hale and G. W. Day. Stability of birefringent linear retarders (waveplates). *Applied Optics*, 27:5146, 12 1988.

[94] D. E. Aspnes. Spectroscopic ellipsometry—a perspective. *Journal of Vacuum Science & Technology A: Vacuum, Surfaces, and Films*, 31, 9 2013.

[95] K. Hebert, S. Zafar, E. Irene, R. Kuehn, T. McCarthy, and E. K. Demirlioglu. Measurement of the refractive index of thin sio_2 films using tunneling current oscillations and ellipsometry. *Applied Physics Letters*, 68:266–268, 1996.

[96] Chun Fang Li. Unified theory for goos-hänchen and imbert-fedorov effects. *Physical Review A - Atomic, Molecular, and Optical Physics*, 76, 7 2007.

[97] Andrea Aiello. Goos-hänchen and imbert-fedorov shifts: A novel perspective. *New Journal of Physics*, 14, 1 2012.

[98] K Y Bliokh and A Aiello. Goos–hänchen and imbert–fedorov beam shifts: an overview. *Journal of Optics*, 15:014001, 1 2013.

[99] F. Goos and H. Hänchen. Ein neuer und fundamentaler versuch zur totalreflexion. *Annalen der Physik*, 436:333–346, 1 1947.

[100] Minkyung Kim, Dasol Lee, Yeseul Kim, and Junsuk Rho. Nanophotonic-assisted precision enhancement of weak measurement using spin hall effect of light. *Nanophotonics*, 11:4591–4600, 9 2022.

[101] Sichen Mi, Tie jun Wang, Guang-Sheng Jin, and Chuan Wang. High-capacity quantum secure direct communication with orbital angular momentum of photons. *IEEE Photonics Journal*, 7:1–8, 2015.

[102] D. Stepanenko and N. Bonesteel. Universal quantum computation through control of spin-orbit coupling. *Physical review letters*, 93 14:140501, 2004.

[103] R. Tenne, Uri Rossman, Batel Rephael, Y. Israel, Alexander Krupinski-Ptaszek, R. Lapkiewicz, Y. Silberberg, and D. Oron. Super-resolution enhancement by quantum image scanning microscopy. *Nature Photonics*, 13:116–122, 2018.

[104] Xuesong Li, Yicong Wu, Yijun Su, Ivan Rey-Suarez, Claudia Matthaeus, T. Updegrove, Zhuang Wei, Lixia Zhang, H. Sasaki, Yue Li, Min Guo, John P Giannini, Harshad D. Vishwasrao, Jiji Chen, Shih-Jong J. Lee, Lin Shao, Huafeng Liu, K. Ramamurthi, Justin W. Taraska, A. Upadhyaya, P. L. La Riviere, and H. Shroff. Three-dimensional structured illumination microscopy with enhanced axial resolution. *Nature Biotechnology*, 41:1307 – 1319, 2022.

[105] Jinkyeong Lee, Jaekyung Kim, Sangmin Shim, Younghwan Yang, Jeonghoon Choi, Junsuk Rho, Dasol Lee, and Minkyung Kim. Real-time observation of the spin hall effect of light using metasurface-enabled single-shot weak measurements. *Nature Communications*, 16, 12 2025.

[106] Minkyung Kim. A compact weak measurement to observe the spin hall effect of light. *Nanophotonics*, 2023.

[107] Jeonghoon Choi, Sangmin Shim, Yeseul Kim, Peng Tang, Guoqiang Li, Junsuk Rho, Dasol Lee, and Minkyung Kim. Experimental observation of spin hall effect of light using compact weak measurements. *Nanophotonics*, 13:3877–3882, 8 2024.

[108] Hailu Luo, Xinxing Zhou, Weixing Shu, Shuangchun Wen, and Dianyuan Fan. Enhanced and switchable spin hall effect of light near the brewster angle on reflection. *Physical Review A - Atomic, Molecular, and Optical Physics*, 84, 10 2011.

[109] Xiaobo Yin, Ziliang Ye, Junsuk Rho, Yuan Wang, and Xiang Zhang. Photonic spin hall effect at metasurfaces. *Science*, 339:1405–1407, 3 2013.

[110] Chong Miao, Dongxue Wang, Eric Herrmann, Zhiyuan Zheng, Haochong Huang, and Hua Gao. Limitations of the transmitted photonic spin hall effect through layered structure. *Scientific Reports*, 11:21083, 10 2021.

[111] Siyuan Liu, Xiaoxing Yin, and Hongxin Zhao. Dual-function photonic spin hall effect sensor for high-precision refractive index sensing and graphene layer detection. *Optics Express*, 30:31925, 8 2022.

[112] Xinxing Zhou, Xiaohui Ling, Hailu Luo, and Shuangchun Wen. Identifying graphene layers via spin hall effect of light. *Applied Physics Letters*, 101(25), 2012.

[113] Xinxing Zhou, Lijuan Sheng, and Xiaohui Ling. Photonic spin hall effect enabled refractive index sensor using weak measurements. *Scientific Reports*, 8:1221, 1 2018.

[114] Chengkang Liang, GuangHui Wang, DongMei Deng, and TingTing Zhang. Controllable refractive index sensing and multi-functional detecting based on the spin hall effect of light. *Optics Express*, 29:29481, 2021.

[115] Shizhen Chen, Xiaohui Ling, Weixing Shu, Hailu Luo, and Shuangchun Wen. Precision measurement of the optical conductivity of atomically thin crystals via the photonic spin hall effect. *Physical Review Applied*, 13:014057, 1 2020.

[116] Shizhen Chen, Xinxing Zhou, Xiaohui Ling, Weixing Shu, Hailu Luo, and Shuangchun Wen. Measurement of the optical constants of monolayer mos2 via the photonic spin hall effect. *Applied Physics Letters*, 118, 3 2021.

[117] Xinxing Zhou, Zhicheng Xiao, Hailu Luo, and Shuangchun Wen. Experimental observation of the spin hall effect of light on a nanometal film via weak measurements. *Physical Review A - Atomic, Molecular, and Optical Physics*, 85, 4 2012.

[118] Zirui Qin, Qinggang Liu, Chong Yue, Yaopu Lang, and Xinglin Zhou. Nanoscale film thickness measurement based on weak measurement. *Review of Scientific Instruments*, 91, 12 2020.

[119] Nathaniel Hermosa, A. M. Nugrowati, A. Aiello, and J. Woerdman. Spin hall effect of light in metallic reflection. *Optics letters*, 36 16:3200–2, 2011.

[120] O. Takayama and G. Puentes. Enhanced spin hall effect of light by transmission in a polymer. *Optics letters*, 43 6:1343–1346, 2018.

[121] Ping Nie, Lijuan Sheng, Linguo Xie, Zhihao Chen, Xinxing Zhou, Yu Chen, and Xiao Lin. Gas sensing near exceptional points. *Journal of Physics D: Applied Physics*, 54:254001, 6 2021.

[122] Younghwan Yang, Taejun Lee, Minkyung Kim, Chunghwan Jung, Trevon Badloe, Dasol Lee, Seokho Lee, Hee Jo Lee, and Junsuk Rho. Dynamic optical spin hall effect in chitosan-coated all-dielectric metamaterials for a biosensing platform. *IEEE Journal of Selected Topics in Quantum Electronics*, 27, 9 2021.

[123] Ruisi Wang, Junxiao Zhou, Kuiming Zeng, Shizhen Chen, Xiaohui Ling, Weixing Shu, Hailu Luo, and Shuangchun Wen. Ultrasensitive and real-time detection of chemical reaction rate based on the photonic spin hall effect. *APL Photonics*, 5, 1 2020.

[124] Jie Cheng, Yinjie Xiang, Jiahao Xu, Shengli Liu, and Peng Dong. Highly sensitive refractive index sensing based on photonic spin hall effect and its application on cancer detection. *IEEE Sensors Journal*, 22:12754–12760, 7 2022.

[125] Guiyuan Zhu, Binjie Gao, Linhua Ye, Junxiang Zhang, and Li-Gang Wang. Enhanced opposite imbert–fedorov shifts of vortex beams for precise sensing of temperature and thickness. *Optica*, 11(1):94–100, Jan 2024.

[126] Alison M. Yao and Miles J. Padgett. Orbital angular momentum: origins, behavior and applications. *Advances in Optics and Photonics*, 3:161, 6 2011.

[127] Stephen M. Barnett, L. Allen, Robert P. Cameron, Claire R. Gilson, Miles J. Padgett, Fiona C. Speirits, and Alison M. Yao. On the natures of the spin and orbital parts of optical angular momentum. *Journal of Optics*, 18:064004, 4 2016.

[128] K. Y. Bliokh, F. J. Rodríguez-Fortuño, F. Nori, and A. V. Zayats. Spin–orbit interactions of light. *Nature Photonics 2015 9:12*, 9:796–808, 11 2015.

[129] Masaru Onoda, Shuichi Murakami, and Naoto Nagaosa. Hall effect of light. *Physical Review Letters*, 93:083901, 8 2004.

[130] Konstantin Yu. Bliokh and Yury P. Bliokh. Conservation of angular momentum, transverse shift, and spin hall effect in reflection and refraction of an electromagnetic wave packet. *Physical Review Letters*, 96, 2 2006.

[131] L. Marrucci. The q-plate and its future. *Journal of Nanophotonics*, 7, 2013.

[132] Martin Neugebauer, Peter Banzer, Thomas Bauer, Sergej Orlov, Norbert Lindlein, Andrea Aiello, and Gerd Leuchs. Geometric spin hall effect of light in tightly focused polarization- tailored light beams. *Physical Review A - Atomic, Molecular, and Optical Physics*, 89, 1 2014.

[133] Victor V. Kotlyar, Sergey S. Stafeev, Elena S. Kozlova, and Muhammad A. Butt. High-order orbital and spin hall effects at the tight focus of laser beams. *Photonics*, 9, 12 2022.

[134] Fedor I. Fedorov. To the theory of total reflection*. *Journal of Optics*, 15:014002, 1 2013.

[135] Christian Imbert. Calculation and experimental proof of the transverse shift induced by total internal reflection of a circularly polarized light beam. *Physical Review D*, 5:787, 2 1972.

[136] K. Yu Bliokh and Yu P. Bliokh. Polarization, transverse shifts, and angular momentum conservation laws in partial reflection and refraction of an electromagnetic wave packet. *Physical Review E - Statistical, Nonlinear, and Soft Matter Physics*, 75, 6 2007.

[137] Yi Qin, Yan Li, Huanyu He, and Qihuang Gong. Measurement of spin hall effect of reflected light. *Optics Letters*, 34:2551, 9 2009.

[138] Chandravati Prajapati, Shankar Pidishety, and Nirmal K. Viswanathan. Polarimetric measurement method to calculate optical beam shifts. *Optics Letters*, 39:4388, 8 2014.

[139] Bo Wang, Yan Li, Meng-Meng Pan, Jin-Li Ren, Yun-Feng Xiao, Hong Yang, and Qihuang Gong. Measuring spin hall effect of light by cross-polarization intensity ratio. *Optics Letters*, 39:3425, 6 2014.

[140] Onur Hosten and Paul Kwiat. Observation of the spin hall effect of light via weak measurements. *Science*, 319:787–790, 2 2008.

[141] Yakir Aharonov, David Z Albert, and Lev Vaidman. How the result of a measurement of a component of the spin of a spin-1/2 particle can turn out to be 100. *Physical Review Letters*, 60:1351, 1989.

[142] Justin Dressel, Mehul Malik, Filippo M. Miatto, Andrew N. Jordan, and Robert W. Boyd. Colloquium: Understanding quantum weak values: Basics and applications. *Reviews of Modern Physics*, 86:307–316, 3 2014.

[143] Yuichiro Mori, Jaeha Lee, and Izumi Tsutsui. On the validity of weak measurement applied for precision measurement. *Journal of Physics B: Atomic, Molecular and Optical Physics*, 53:015501, 1 2020.

[144] Ling-Jun Kong, Xi-Lin Wang, Si-Min Li, Yongnan Li, Jing Chen, Bing Gu, and Hui-Tian Wang. Spin hall effect of reflected light from an air-glass interface around the brewster's angle. *Applied Physics Letters*, 100, 2 2012.

[145] Shizhen Chen, Xinxing Zhou, Chengquan Mi, Hailu Luo, and Shuangchun Wen. Modified weak measurements for the detection of the photonic spin hall effect. *Physical Review A*, 91:062105, 6 2015.

[146] Zirui Qin, Qinggang Liu, Chong Yue, Yaopu Lang, and Xinglin Zhou. Improved model of weak measurement for detecting the photonic spin hall effect. *Journal of Physics D: Applied Physics*, 52, 2019.

[147] Zirui Qin, Runhao Zhang, Lingtong Zhang, Linjiao Ren, Pei Zhang, Rubin Qi, Qingfang Zhang, Chenglin Wang, and Liying Jiang. Optimized weak measurement model for in-plane and out-of-plane splitting shifts of photonic spin hall effect. *Optics Communications*, 557:130283, 4 2024.

[148] A. Aiello and J. P. Woerdman. Role of beam propagation in goos–hänchen and imbert–fedorov shifts. *Optics Letters*, 33:1437, 7 2008.

[149] Mark R Dennis and Jörg B Götte. The analogy between optical beam shifts and quantum weak measurements. *New Journal of Physics*, 14:073013, 7 2012.

[150] Angel Yanguas-Gil and Herbert Wormeester. *Relationship Between Surface Morphology and Effective Medium Roughness*. Springer Berlin Heidelberg, 2013.

[151] The MathWorks, Inc. *Smoothing Splines (R2023a)*. The MathWorks, Inc., Natick, Massachusetts, 2023. Accessed: 2025-08-21.

[152] The MathWorks, Inc. *Fit Gaussian Models (R2023a)*. The MathWorks, Inc., Natick, Massachusetts, 2023. Accessed: 2025-08-21.

[153] Jakub Siegel, Olexiy Lyutakov, Vladimír Rybka, Zdeňka Kolská, and Václav Švorčík. Properties of gold nanostructures sputtered on glass. *Nanoscale research letters*, 6(1):96, 2011.

[154] Petr Malinskỳ, Petr Slepička, Vladimír Hnatowicz, and Václav Švorčík. Early stages of growth of gold layers sputter deposited on glass and silicon substrates. *Nanoscale research letters*, 7(1):241, 2012.

[155] *ISO 25178-6:2010 Geometrical product specifications (GPS) — Surface texture: Areal — Part 6: Classification of methods for measuring surface texture*, 2010.

[156] *ISO 25178-2:2021 Geometrical product specifications (GPS) — Surface texture: Areal — Part 2: Terms, definitions and surface texture parameters*, 2021.

[157] *ISO 14406:2010 Geometrical product specifications (GPS) — Extraction*, 2010.

[158] Angela Duparré, Josep Ferre-Borrull, Stefan Gliech, Gunther Notni, Jörg Steinert, and Jean M. Bennett. Surface characterization techniques for determining the root-mean-square roughness and power spectral densities of optical components. *Applied Optics*, 41:154, 1 2002.

[159] Richard Koops, Marijn Van Veghel, and Arthur Van De Nes. A dedicated calibration standard for nanoscale areal surface texture measurements. *Microelectronic Engineering*, 141:250–255, 6 2015.

[160] David Brewster. Ix. on the laws which regulate the polarisation of light by reflexion from transparent bodies. by david brewster, ll. d. f. r. s. edin. and f. s. a. edin. in a letter addressed to right hon. sir joseph banks, bart. k. b. p. r. s. *Philosophical Transactions of the Royal Society of London*, 105:125–159, 12 1815.

[161] H. M. Lai and S. W. Chan. Large and negative goos–hänchen shift near the brewster dip on reflection from weakly absorbing media. *Optics Letters*, 27:680, 5 2002.

[162] Xinxing Zhou, Xing Li, Hailu Luo, and Shuangchun Wen. Optimal preselection and postselection in weak measurements for observing photonic spin hall effect. *Applied Physics Letters*, 104, 2014.

[163] Jörg B. Götte and Mark R. Dennis. Limits to superweak amplification of beam shifts. *Optics Letters*, 38:2295, 7 2013.

[164] Julián Martínez-Rincón, Wei-Tao Liu, Gerardo I. Viza, and John C. Howell. Can anomalous amplification be attained without postselection? *Phys. Rev. Lett.*, 116:100803, Mar 2016.

[165] Zhaoxue Li, Xiong Liu, Yu He, Zhiyou Zhang, Lan Luo, and Pi Duan. Anomalous amplification in almost-balanced weak measurement for measuring spin hall effect of light. *Optics Express, Vol. 28, Issue 5, pp. 6408-6416*, 28:6408–6416, 3 2020.

List of Publications and Awards

Journal Articles

[1] N. Zahra, Y. Mizutani, T. Uenohara, Y. Takaya, ”Spin hall effect of light ellipsometry for nanoscale areal surface measurement”, Scientific Reports, 15, 1, 12911, (2025).

[2] N. Zahra, Y. Mizutani, T. Uenohara, Y. Takaya, ”Precision roughness measurement of smooth surface utilizing spin–orbit interaction of light with near Brewster's angle incidence”, Measurement: Sensors, 101841, (2025).

[3] N. Zahra, Y. Mizutani, T. Uenohara, Y. Takaya, ”Enhanced measurement of smooth surface using the Spin Hall Effect of Light ellipsometry with near Brewster's angle incidence”, Measurement, 120163, (2025).

International Conferences

[1] N. Zahra, Y. Mizutani, T. Uenohara, Y. Takaya, ”Subwavelength Beam Shift at the Reflection of Orbital Angular Momentum–Induced Beam Generated by Vortex Retarder.”, Optical Technology and Measurement for Industrial Applications Conference (OPTM) 2025, OPTM3-02, Yokohama, (2025).

[2] N. Zahra, Y. Mizutani, T. Uenohara, Y. Takaya, ”Refractive Index Measurement based on the Orbital Angular Momentum Amplified Spin Hall Effect of Light.”, Optics and Photonics Japan (OPJ) 2024, 30aEJ5, Tokyo, (2024).

[3] N. Zahra, Y. Mizutani, T. Uenohara, Y. Takaya, ”Spin Hall Effect of Light (SHEL) Ellipsometry for surface measurement with different models of optical interface.”, Optical Technology and Measurement for Industrial Applications Conference (OPTM) 2024, OPTM6-03, Yokohama, (2024).

[4] N. Zahra, Y. Mizutani, T. Uenohara, Y. Takaya, ”Fresnel model and effective medium approximation (EMA) in spin hall effect of light ellipsometry for surface measurement of optics.” International Symposium on Optomechatronics Technology (ISOT) 2023, Nasu, (2023).

[5] N. Zahra, Y. Mizutani, T. Uenohara, Y. Takaya, ”Propagation Enhancement Factor in the Spin Hall Effect of Light (SHEL) Observation for Smooth Optics Measurement.”, 8th International Conference on Instrumentation, Control, and Automation (ICA) 2023, Jakarta, (2023).

[6] N. Zahra, Y. Mizutani, T. Uenohara, Y. Takaya, ”On the application of the Spin Hall Effect of reflected light for smooth optics measurements.”, 2023 Siegman International School on Lasers, Poster, Dublin, (2023).

[7] N. Zahra, Y. Mizutani, T. Uenohara, Y. Takaya, ”Image Processing Aspect of Transverse Shift Measurement in the Spin Hall Effect of Light (SHEL) Ellipsometry.”, The 19th International Conference on Precision Engineering (ICPE), C-186, Nara, (2022).

[8] N. Zahra, Y. Mizutani, Z. Li, T. Uenohara, Y. Takaya, ”Ellipsometry based on spin Hall effect of light (SHEL) using modified weak measurement for surface area measurement.” Optical Technology and Measurement for Industrial Applications Conference (OPTM) 2022, OPTM1-03, Yokohama, (2022).

Domestic Conferences

[1] N. Zahra, Y. Mizutani, T. Uenohara, Y. Takaya, ”Development of Ellipsometry Based on Spin Hall Effect of Light (6th report): Accuracy Affecting Parameters.”, Japan Society of Precision Engineering (JSPE) Semestrial Meeting 2024, C-03, Tokyo, (2024).

[2] N. Zahra, Y. Mizutani, T. Uenohara, Y. Takaya, ”Detecting transverse shift in the ellipsometry based on Spin Hall Effect of Light (SHEL) through weak measurement for sub–nanometer surface area measurement”, 2022 Annual Meeting of The Abrasive Technology Society Japan (ABTEC), B-26, Yokohama, (2022).

Awards

[1] Best Paper Award, The 19th International Conference on Precision Engineering (2022). “Image processing aspect of transverse shift measurement in the Spin Hall effect of Light (SHEL) Ellipsometry” (Naila Zahra, Yasuhiro Mizutani, Tsutomu Uenohara, Yasuhiro Takaya)

[2] 2024 Encouragement Award. The Japan Society for Die and Mould Technology (2024). “SHEL 偏光計による研磨面のサブナノオーダー表面粗さ計測”. 水谷康弘、Naila Zahra Faiz、上野原 努、高谷裕浩

Acknowledgements

Bismillahirrahmanirrahim. First and foremost, my most tremendous gratitude to Allah SWT for His grace, His blessings, and His divine intervention throughout the ups and downs of this long journey. *Sufficient to me is Allah and He is the best disposer of affairs (QS 3:173).*

I am deeply grateful to my advisor, Professor Yasuhiro Mizutani, whose trust in me has been the most essential element from the beginning to the completion of my study. His confidence in my abilities, support, and constructive feedback have not only shaped this research but also influenced my personal and academic growth. His continuous encouragement to challenge myself since the beginning has been pivotal for me, as I often limit my potential. I still remember and will remember his message, "Challenge is good," when we discussed my interview back in 2019. Thank you for trusting me with this opportunity.

My deep gratitude to Professor Yasuhiro Takaya for allowing me to join this laboratory. It is such an honor to work under the supervision of a distinguished figure in this field. His constructive feedback and challenging questions, though often difficult to answer, pushed me to recognize the level of depth and critical thinking expected of a doctoral candidate.

I would like to express my sincere gratitude to Professor Toshiyuki Enomoto and Professor Shuichi Ino for their valuable feedback, constructive comments, and insightful questions during the dissertation review process. I am especially grateful for their willingness to review this work, and for the time and care they devoted to providing thoughtful and rigorous evaluations.

I would like to sincerely thank Dr. Tsutomu Uenohara, who has been giving his support since the beginning, assisting with all purchases of goods, technical experiment work, and even trivial daily laboratory matters. His experimental know-how greatly helps my research. His feedback and comments to every student during General Meetings always serve as a reminder to me to be meticulous in my work.

I extend my sincere thanks to Ms. Momoe Hayashi, secretary at the Takaya-Mizutani Laboratory, for her kind help with all the paperwork and administrative work so that every business trip went very smoothly.

To all members of Takaya-Mizutani Laboratory during my stay, thank you very much for your kind understanding of this non-Japanese-speaking member. I'm sorry yet very grateful for considering my dietary restriction at all parties held. To Kataoka-san, thank you for being a helpful tutor and colleague. To Kawakami-san, Yoshioka-san, Yasuda-san, and Shi-san, thank you for being my very first colleagues and for being very welcoming and friendly. To Mona, my fellow English-speaking woman, your hard work is such an inspiration to me. To Ellie, thank you for showing me what resilience and persistence are. Lastly, to my fellow Indonesian comrades, Reza and Aji, thank you for all the "support", your presence makes this journey more bearable. To all members of the Takaya-Mizutani laboratory who crossed my

path over the years, thank you very much, and good luck with your next endeavors.

My heartfelt gratitude to all the friends I met during my studies in Osaka. Thank you for all your help and for our meetings and talks, which have kept me sane this time. Honorary thanks to Professor Yoshiro Ogura of Osaka Metropolitan University and his Outdoor Adventure Team for all the trips that introduced me to many beautiful places in Japan and taught me to enjoy hiking. To my seniors and colleagues in the Instrumentation, Control, and Automation research group and the Engineering Physics department at ITB, thank you for all your support.

Last but not least, to my beloved family, thank you for your endless love, prayers, and encouragement. Ibu and Ayah, thank you for letting me embark on this journey in a faraway place from home and for keeping me in your prayers. Sisters and brothers, Prita, Tajudin, Amira, Fathie, and Sharyn, my nephew Aqil, my nieces Adhwa and Shafa, thank you for taking care of everything while I was away and keeping me informed about what happened at home. Your unwavering support and love have been my foundation, giving me the strength and courage to face the challenges of this journey.

Once again, for all the warm support and encouragement, thank you very much.

Osaka, December 2025

Naila Zahra